Development of a Process for Determining Minimum Feature Size in Additive Manufacturing with Applications to Topology Optimization

Benjamin M. Weiss

A dissertation

submitted in partial fulfillment of the

requirements for the degree of

Doctor of Philosophy

University of Washington

2017

Reading Committee:

Duane W. Storti, Chair

Mark Ganter, Chair

Joshua Hamel

Program Authorized to Offer Degree:

Mechanical Engineering

University of Washington

Abstract

Development of a Process for Determining Minimum Feature Size in Additive Manufacturing with Applications to Topology Optimization

Benjamin M. Weiss

Co-chairs of the Supervisory Committee:
Professor Duane W. Storti
Professor Mark Ganter
Mechanical Engineering

Additive manufacturing (AM) is opening a new creative landscape for designers. Freedom of form and material creates opportunities for customization, increased functionality, and higher complexity in manufactured objects. Characterizing and understanding the unique manufacturing constraints of AM is a key to enabling the designer to leverage the full potential of AM to produce highly complex geometries. In this work, “minimum feature size”, defined as the smallest scale at which a feature of a particular shape in a particular orientation can be manufactured, is examined in detail. A parameterization for shape and orientation of small features is developed, and an adaptive, iterative experimental procedure is created to accurately estimate the minimum feature size for a particular feature type in the parameter space. A design of experiments process is used to systematically explore the minimum feature size over the space of parameterized shapes and orientations. This process is applied to three different AM

platforms, and in each case minimum feature size spans an order of magnitude over the set of considered features. The data collected are used to create a parametric design rule for each process, a function which provides a detailed map of the minimum feature size achievable over the parameter space. The parametric design rule is applied to typical design problems, used to assess existing 3D models for manufacture, and applied to design optimization frameworks. The parametric design rules produced are found to more tightly follow the actual capabilities of the AM processes, increasing the envelope for complexity compared with existing design guidelines consisting of one or two constant minimum feature sizes and improving accuracy in predicting the minimum feature sizes for new geometries by as much as 50%. Application is made to three design problems, realizing significant improvements in each case.

The experimental study of minimum feature size is complemented by an adaptation of topology optimization to incorporate the parametric design rules into an automated design process. A new variant of the Moving Morphable Components (MMC) approach is created, improving convergence through a “bootstrapping” approach and integrating the feature-dependent design rules to ensure manufacturability of the result. Experimentally-verified manufacturable outputs are achieved while sacrificing less than 5% of the objective function value for several test problems. By bringing together experimental assessment of minimum feature size and design optimization through the creation of parametric design rules, a novel, reproducible, and practical process for ensuring manufacturability of optimized designs is created.

TABLE OF CONTENTS

LIST OF ACRONYMS AND JARGON

AM: Additive Manufacturing – a class of manufacturing methods in which an object is created layer-by-layer in an additive (rather than subtractive) process under the control of a numerically-controlled (NC) machine.

bcMMC: Bootstrapped, Constrained Moving Morphable Components – an extension to the cMMC approach first described in this dissertation in which the initial configuration of the components is derived from a separate topology optimization process (SIMP) through a "bootstrapping" process.

CMC: Connected Morphable Components – a type of MMC approach in which the components are connected end-to-end via an explicit linking of decision variables so that the optimizer cannot separate them (Deng and Chen, 2016)

cMMC: Constrained Moving Morphable Components – a variant of the MMC approach first conceived in this dissertation under which the individual components are subjected to manufacturability constraints based on each component's shape and orientation.

Heaviside Function: The unit step function, i.e. $H(x) = \begin{cases} 1 & \text{if } x \geq 0 \\ 0 & \text{if } x < 0 \end{cases}$, named for Oliver Heaviside (1850-1925).

Material Extrusion: (also occasionally referred to in citations as FDM, a trade name of Stratasys, Inc) – A type of additive manufacturing in which a material (commonly plastic) is melted in a hot nozzle and extruded out under computer control to build up an object layer by layer. See Section 1.6B for additional details.

Minimum Feature Size: In this work, "Minimum feature size" refers to the smallest scale at which a shape in a particular orientation can be manufactured, usually specified as the

dimension of the smallest side of the shape (i.e. thickness or diameter), while the aspect ratios of other parameters are held constant (i.e. the shape is scaled, not stretched).

MMC: Moving Morphable Components – a method of topology optimization (design automation) in which the decision variables controlled by the optimizer consist of the locations and shapes of various primitives, which are combined together through Boolean operations to form the final design.

Negative Feature: A feature in a design which removes material from the object, such as a hole, slot, cavity, or cut. As opposed to a Positive feature.

PLA: Polylactic Acid – A polymer thermoplastic (plastic) used in the material extrusion AM process considered in this work as the feedstock. PLA is noted for being derived from renewable sources and possessing a very small coefficient of thermal expansion.

Positive Feature: A feature which adds new material to a design, such as a bar, fin, boss, or extrusion. As opposed to a Negative feature.

Powder Bed Fusion: A type of additive manufacturing in which layers of loose powder are melted using a laser or some other means to form the final part. See Section 1.6A for additional details. Citations frequently refer to Selective Laser Sintering, or SLS, which is the trade name for the laser powder bed fusion process from 3D Systems Corporation.

SIMP: Solid Isotropic Material with Penalization – One of the earliest topology optimization approaches, in which the decision variable selected by the optimizer is the (continuous) density at each element of an FE grid, with a penalization on intermediate density elements to push towards a 0-1 solution.

Shape Skeleton: A shape skeleton is the result of a geometric transformation on a shape (called the Medial Axis Transform) which reduces it to the set of points at the centers of all the balls touching the boundary of the shape in at most two places while remaining entirely within the shape.

TO: Topology Optimization – a type of design optimization in which the number and placement of holes (topology) and sizing of various elements (topography) both occur simultaneously. See Section 1.6D for details.

Vat Photopolymerization: A type of additive manufacturing in which a (typically liquid) monomer resin placed in a vat is polymerized under computer-controlled exposure of UV light. See Section 1.6C for details. Stereolithography, abbreviated SLA, is often used by other authors in citations when referring to this process.

LIST OF FIGURES

LIST OF TABLES

ACKNOWLEDGEMENTS

So many people have worked so hard to make this dissertation possible; the list below is far from comprehensive…

Thank you to my advisors, Mark, Duane, and Josh, for your unending encouragement, council, feedback, patience, and friendship as I have walked through this process.

Thank you to my supervisory committee for providing excellent insights into my work and encouraging me to strive for excellence.

I am grateful to many other colleagues who have advised, helped, or otherwise kept me going, including Olaf Diegel, my advisor and host in Sweden, Ashley Pigott, who graciously lent me much of her time to spearhead the Form2 manufacturing, Grant, Mete, Di, and Molly for the comradery and encouragement of the lab.

Many thanks are due to my sweet wife, Katie, who sacrificed so much to help me achieve this. I love you!

Most important of all, I acknowledge the encouragement, strength, ideas, and opportunities that came from my relationship with Jesus Christ over these last four years. He is the one who truly deserves all the credit.

I am also obliged to acknowledge the financial support of the NSF for three years of my graduate work: This material is based upon work supported by the National Science Foundation Graduate Research Fellowship Program under Grant No. DGE-1256082 and an international travel allowance through the Graduate Research Opportunities Worldwide (GROW). Any opinions, findings, and conclusions or recommendations expressed in this material are those of the author(s) and do not necessarily reflect the views of the National Science Foundation

DEDICATION

To my Lord and Savior, Jesus Christ.

Take joy, my King, in what You hear; may it be a sweet, sweet sound in Your ear.

(Laurie Klein, House of Mercy Music)

Chapter 1. INTRODUCTION

1.1 MOTIVATION

Additive manufacturing (AM) is challenging the status quo of how objects are made (Gustafson, 2012, p. 2). The removal of constraints in the "traditional" manufacturing process opens new freedoms for designers. AM enables customizability of products to particular users, flexibility in the face of rapidly-shifting demand, new materials, and the ability to make seemingly arbitrarily complex structures (Maher et al., 2014). It relieves designers of many manufacturability considerations: no more wall thickness constraints in molding and casting; no more expense for milling hard-to-reach cavities. The result has been an explosion in new applications for the technology, from implants and prosthetics to novel mesostructured materials for lighter-weight components to amateur designers creating art, engineering, even architecture (Gustafson, 2012).

While AM relieves many design constraints, its capabilities have their own, unique limits, which are many times harder to predict and codify, resulting in an iterative, trial-and-error design process (Gao et al., 2015, p. 66). Layer-by-layer manufacturing cannot build on nothing, so overhanging facets of a design may not be producible (Lazarov et al., 2016). The AM machine's mechanism for adding material, be it deposition, fusion, photopolymerization, binding, or otherwise, introduces a lower limit on the size of components which can be created. This "minimum feature size" is the additive manufacturing equivalent of line width in lithography, dot size in 2D printing, or the size of the smallest brick when creating with Legos, and is an important aspect of the process's capability (Byun and Lee, 2003). In addition to the underlying resolution of the machine, minimum feature size also depends on other aspects of the process physics, such as the ability of the partially-formed part to withstand mechanical and thermal loads from the manufacturing process and support its own weight. It determines the complexity that can be created by the designer and physically realized by an AM process, and constrains the performance

of mesostructured materials, lattices, bio-scaffolds, and microfluidic devices. Minimum feature size also impacts the amount of material required to create support structures, which can play a significant role in the production cost.

1.2 Research Thrust

In light of the importance of minimum feature size to the design and manufacturing community, characterizing and predicting it form the central theme of this work. The culminating contribution is a method for experimentally characterizing minimum feature size is presented and used to create predictive design rules for the minimum manufacturable feature size of a wide variety of features of different shapes and orientations in a manner that can be replicated across AM platforms. These design rules are applied to various design problems and extended for use in an automated design process.

The remainder of this introduction collects in one place the unique and significant aspects of the current work and describes several applications of the outcomes. Subsequently, several preliminary concepts are presented to provide context for the remaining chapters. Each chapter contains its own review of the relevant literature.

1.3 Uniqueness

This study is the first work to bring together quantitative experiments on an AM process with topology optimization approaches through the use of parametric design rules. Although extensive bodies of literature are present in both the definition of AM design rules and in topology optimization for AM applications, no other researchers have been found who are active in both areas. In addition to being broad in scope, each major aspect of the work presents individual areas of uniqueness.

The process developed for estimating minimum feature size introduces a novel iterative, adaptive method which reduces the number of copies of a feature which must be manufactured to

achieve a given level of confidence in the result. Only a one study assessing minimum feature size seeks to characterize the statistical variability present in the creation of small features in any process (Meisel and Williams, 2015). The characterization approach is presented here is a reusable, cross-platform method applicable to a wide array of AM technologies.

Other researchers recognize that different types of features in different orientations can attain different minimum feature sizes (Seepersad et al., 2012; Wegner and Witt, 2012). This work develops a practical parameterization for the shape and orientation of small features and uses it to link minimum feature size estimates of different shapes into continuous parametric design rules which can predict the minimum feature size for shapes and orientations not assessed experimentally.

Finally, the parametric design rules developed are applied to a topology optimization problem, making it among the very first to utilize constraints based on feature dimensions and orientation in a topology optimization context. To support the constraint, a novel "bootstrapping" approach for leveraging the results of a faster form of topology optimization (known as Solid Isotropic Material with Penalization, or SIMP) to provide high-quality initial designs for a slower, but more capable, optimization approach (referred to as Moving Morphable Components, or MMC).

1.4 SIGNIFICANCE

In addition to being unique among existing works, the research presented in this dissertation also represents a significant contribution. Quantitative measures of success and impact will be developed in the following chapters and summarized in the Conclusion, but the approach itself presents several important areas of conceptual significance.

A cross-platform method for determining minimum feature size which produces highly accurate estimates incorporating statistical variation in the process like the one developed in Chapter 2 has potential to be very useful in characterizing the capabilities of AM processes,

especially because the proposed process focuses on features near the failure transition, making it more accurate and efficient than existing alternatives. In addition, the study explores the interplay between overhang angle and feature shape, providing insights into situations in which the maximum overhang angle design guideline might be safely broken.

In the process of creating predictive parametric design rules from collected minimum feature size data, the tradeoff between the number of points in the parameter space (i.e. the number of different shapes and orientations at which to sample the minimum feature size) and the quality of the resulting design rule is explored. This aspect of the study which explores the quality of design rules based on different amounts of experimental minimum feature size data begins to address a significant unanswered question in the existing literature, namely how much data should be collected when characterizing minimum feature size for a process. The parametric design rules are able to more precisely follow the minimum feature size over a wide range of feature types, and applications are made to "typical" design and sizing problems, as well as to automated (topology optimization) approaches. In addition to providing detailed surveys for two AM processes, the outcomes include a reproducible process which can be used by other researchers to characterize their processes.

The approach developed in Chapter 4 to handle the data-driven constraint for topology optimization is significant in its ability to reliably reflect the real capabilities of an AM platform to the design process, addressing a significant need in the literature (Deaton and Grandhi, 2014). Existing design rules (a single minimum feature size and a maximum overhang angle) provide coarse constraints on the optimization process, often at significant expense to the objective function, and result in designs which do not take full advantage of the manufacturing system's capabilities (Langelaar, 2017). Accurately characterizing what can and cannot be produced and designing directly to that standard removes much of the post-processing difficulty and trial-and-error iteration currently required for optimization of designs for AM. In the next section, several applications of the technology are discussed.

1.5 APPLICATIONS

Applications of the current work are numerous. In the coming chapters, minimum feature size parametric design rules are used in three example design problems to highlight the real-world utility of the results. First, the adaptation of a prosthetic hand to make it manufacturable on a polyamide (Nylon) laser powder bed fusion process is presented, showing how information regarding the maximum manufacturable length for cavities in that process can be leveraged to adapt designs to its unique requirements for powder removal. Later, a sizing problem is addressed, in which a pre-existing model of the Space Needle is assessed for manufacturing, and the minimum scale at which it can be reliably produced is determined. Finally, the design rules are applied to minimizing the unit cell dimensions of an octet truss lattice while maintaining a constant effective density by independently setting each truss member to its minimum manufacturable thickness in the context of a search problem.

Applications of the topology optimization approach are very wide, and extend to optimal truss design, graded mesostructured materials, and beyond. In this work, only preliminary examples are reported, but the method developed has broad application to real-world design problems.

1.6 PRELIMINARIES

Before going further into the theory that enables these applications, a brief background on several additive manufacturing technologies referred to throughout this work is presented, along with a short explanation of topology optimization. This section is intended to provide context and clarify unfamiliar terms used through this dissertation; more thorough literature reviews for each topic are presented in each of the subsequent chapters.

Every effort is made in this section and throughout the broader work to refer to additive manufacturing technologies and terminologies according to the definitions codified by ASTM/ISO (ASTM International, 2015).

A. The Powder Bed Fusion AM Process

Powder bed fusion is a category of AM process in which layers of powder are fused into solid material under the direction of a heat source. The specific powder bed fusion process considered in this work is the EOS Formiga P 110, which uses a laser is used to melt powder to form a solid structure (this is sometimes referred to as Laser Sintering; see Figure 1.1). The part is formed layer-by-layer in the build chamber out of powdered polyamide plastic (also known as Nylon). For every layer, the feed chamber, containing powdered feedstock, is raised slightly, and a roller moves across it and deposits the powder on the top of the build chamber, which moves down to accommodate it. Next, laser radiation is directed at the powder surface in a pattern corresponding to the solid material on that layer, selectively melting the powder grains to each other and to the lower layers. The process is repeated until all parts are formed.

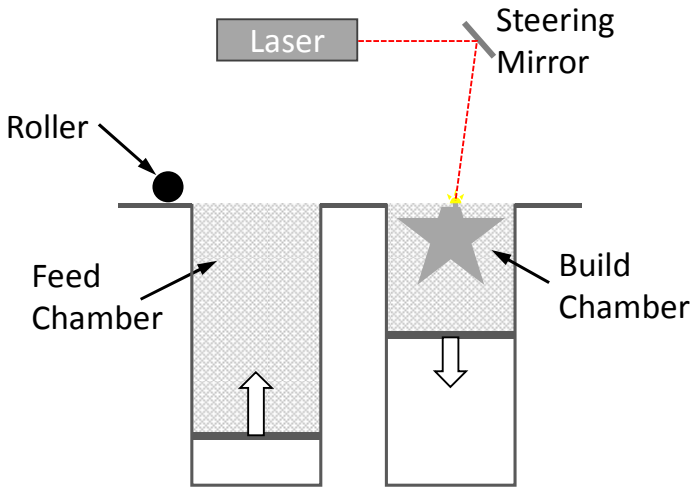

Figure 1.1. Schematic of the considered powder bed fusion process.

After manufacturing in this powder bed fusion process, parts must be removed from the build chamber and cleaned of excess, un-melted (or partially melted) powder in a post-processing

step. This is done by blasting the finished parts with a mixture of compressed air and extra powder in a process colloquially referred to as “depowdering”. For the laser-fused polyamide powder bed fusion process used in this study, the surrounding powder in the build chamber provides support for downward-facing faces in the part as it is being manufactured, so no overhang constraints are present. Most manufacturing problems in this process arise when the laser power melts excess powder, especially in holes, producing unwanted geometry.

B. The Material Extrusion AM Process

In the Material Extrusion AM process considered in this dissertation, the FlashForge Finder, the feed material consists of a spool of plastic filament, which is fed into a print head (see Figure 1.2). The print head moves over the build platform and contains a heated nozzle which melts the plastic, extruding it out onto the part where it solidifies, forming the desired geometry.

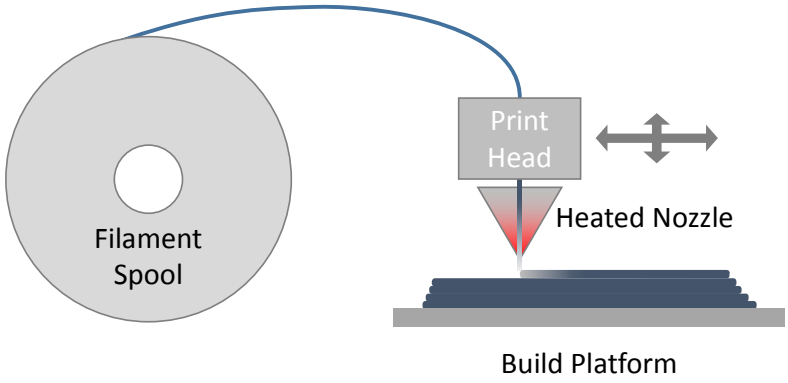

Figure 1.2. Schematic of the material extrusion process

The molten filament must have some kind of existing structure to support it while it solidifies, so support structures for overhanging features are typically included in the build. Support structures can be made of the same material as the main part and mechanically separated from the finished product, or of a different material which can be removed by chemical or other means. Besides removal of support structures, no other post-processing of finished parts is required. Because the filament is inexpensive, material extrusion is among the most economical

classes of AM process, but has comparatively poor resolution owing to the comparatively large diameter of the nozzle.

C. Vat Photopolymerization AM Process

The vat photopolymerization category of AM processes creates objects through polymerization reactions. The FormLabs Form2 is the particular vat photopolymerization process used in this work. In the Form2, the input material is a liquid monomer resin which polymerizes when exposed by a UV laser. The resin is placed in a tank with a glass bottom, and laser light solidifies the resin just beyond the glass plate (see Figure 1.3). A build platform moves up after each layer is created, collecting them into a final part.

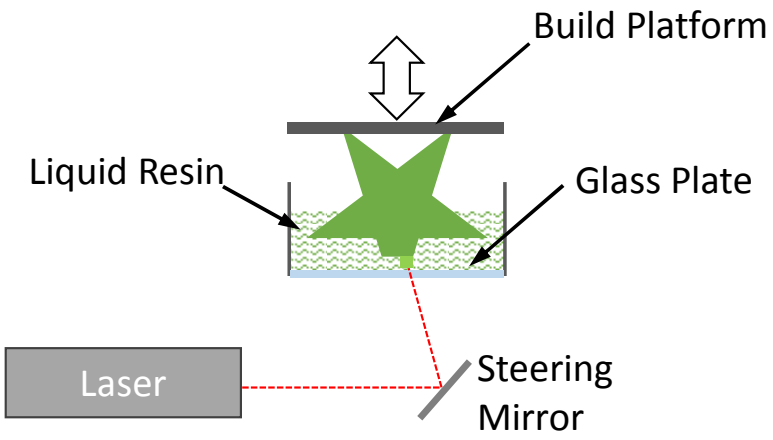

Figure 1.3. Vat photopolymerization process schematic

After manufacturing, the part must be post-processed by washing away remaining uncured resin with a solvent, then cured in a UV chamber to finish the photopolymerization process. Performance for small features of the vat photopolymerization process studied here is complicated by the fluid dynamic forces present in the resin tank and in the post-processing bath. Small features are fragile until post-curing completes the solidification process.

D. Topology Optimization

Traditionally, the design process has required a human to interpret the constraints and performance goals and use creativity and artistry to invent designs which solve the problem effectively. “Topology optimization” refers to a broad class of algorithms which seek to select an (nearly) optimal geometry to minimize an objective function subject to constraints, effectively doing the job traditionally handled by the designer (Rozvany, 2001; Sigmund and Maute, 2013). A more detailed introduction, along with a literature review, is presented in Chapter 4, and this subsection is intended only provides a small amount of additional context. The inputs to a topology optimization problem consist of a design domain, which sets the overall envelope in which the optimizer is allowed to define geometry, domain-specific information needed for the analysis (i.e. loads, supports, and material properties for solid mechanics problems), and an objective function to be minimized (see Figure 1.4). Compliance minimization (i.e. maximum stiffness) objectives are common in the literature, but applications to a variety of other fields are also possible (Deaton and Grandhi, 2014). Unlike shape optimization and sizing optimization (Haftka and Grandhi, 1986), which start with an initial geometry and adjust the size and/or shape of its elements , topology optimization is allowed (and expected) to significantly modify the topology of the object (number of holes), which is a more complicated mathematical problem.

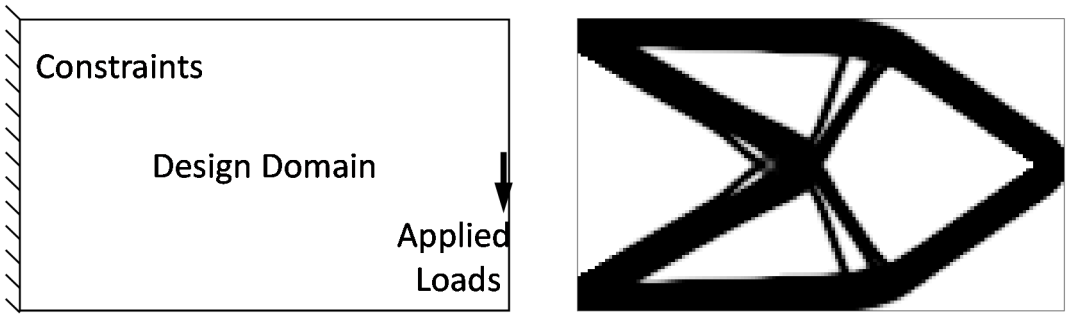

(a) (b)

Figure 1.4. Problem setup for topology optimization. (b) An example topology optimization result

The result of the optimization problem is a division of the design domain into solid and void regions, showing where to put material to achieve the local minimization of the objective found

by the optimizer. Usually, the results of topology optimization problems are taken as suggestions for the designer to integrate into a more traditional design process which can incorporate additional considerations such as manufacturing constraints, but increasingly automated tools enable direct manufacturing of optimized designs (Lazarov et al., 2016).

Topology optimization is constrained by the speed of the analysis problem (FEA in mechanics) which must be solved at every step of the iteration (Deaton and Grandhi, 2014, p. 14). Computations in 3D are particularly resource intensive, and for objective functions for which derivative information cannot be cheaply obtained the problem frequently becomes intractable because of the large number of design variables (Sigmund, 2011).

E. Shape Skeletons

Shape skeletons are a geometric transformation of an object which forms one of the central tools in Chapter 4. Conceptually, a shape skeleton seeks to find a set of center curves (2D) or center surfaces (3D) through a model which fully represents the shape's connectedness and follows the midline (equidistant between two faces).

The shape skeleton is constructed using the Medial Axis Transform, first proposed almost 50 years ago (Siddiqi and Pizer, 2008). The Medial Axis Transform first defines the concept of a maximal ball, which is a ball (circle in 2D, sphere in 3D) which touches the boundary of the object in two or more places but remains entirely inside it. Note that by this definition the center of a maximal ball is a point equidistant from two faces of the object. The medial axis (used equivalently to "shape skeleton" here) is constructed as the union of the set of the centers of all maximal balls inside the input object (see Figure 1.5). Often, the radius of the maximal ball associated with each point on the shape skeleton is also retained. If radius information is present and the sampling of maximal balls continuous, the shape skeleton can be used to perfectly reconstruct the input object.

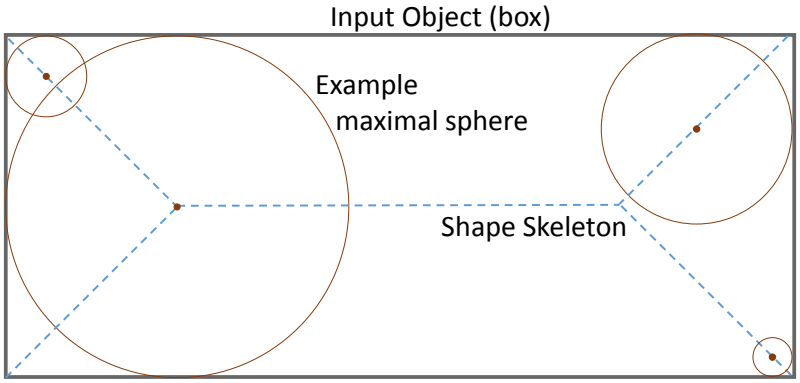

Figure 1.5. Illustration of a shape skeleton and its construction.

The brief explanation of three AM technologies and topology optimization in this section are intended only for general background of the interested reader of several topics relevant to the remainder of this work. This section is by no means intended to serve as a literature review, as each chapter includes its own survey of prior research.

1.7 Dissertation Scope and Organization

This dissertation seeks to create a reusable method for characterizing the minimum feature size capabilities of an AM process. The scope does not include investigating other types of design constraints on additive manufacturing machines (such as maximum overhang angle), nor is determining the root cause of the characterized behavior investigated. The as-manufactured dimensions of small features are not assessed, only the ability of the process to manufacture features visually similar to those in the design. In order to be applicable to a wide variety of processes, a purely experimental approach is used which captures a machine's capabilities without requiring detailed process models.

This work is organized into three main chapters, corresponding to three publications (one presently accepted and two more in preparation). First, the iterative, adaptive assessment process is prototyped in a powder bed fusion process in Chapter 2. Next, Chapter 3 applies and extends this approach to formulate a general-purpose, cross-process AM minimum feature size characterization tool, evaluated using material extrusion and vat photopolymerization processes,

and used to create predictive design rules. Finally, the parametric design rules created are applied in the context of topology optimization, and Chapter 4 details an extension of existing topology optimization approaches required to enable this.

Chapter 2. Estimating Minimum Feature Size in a Polyamide Powder Bed Fusion Process

2.1 Preface

In this chapter, the iterative, adaptive approach for sampling minimum feature size is developed, and a preliminary design rule based on an extensive experimental sampling is selected and found to be effective in predicting the minimum feature size for negative features (holes) in a powder bed fusion process using a laser to melt polyamide (Nylon) powder feedstock. The approach works well in part because this powder bed fusion process has no overhang difficulties, allowing the relatively simple design rule selected to be effective in modeling the comparatively simple underlying minimum feature size function. Nevertheless, the basic experimental approach for determining the minimum feature size of a particular oriented shape is developed in this chapter and represents a significant advance in the accuracy and quality of such estimates.

This chapter was developed and written while on international exchange under the direction of Prof. Olaf Diegel, Lund University, Sweden. A reduced form of this chapter is accepted for publication in Rapid Prototyping Journal:

Weiss, B., Diegel, O., Storti, D., Ganter, M., 2018. A Process for Estimating Minimum Feature Size in Selective Laser Sintering. Rapid Prototyping Journal 24.

2.2 Abstract

Purpose: Manufacturer specifications for the resolution of an additive manufacturing (“AM”) machine can be ten times smaller (more optimistic) than the actual size of manufacturable features. Existing methods used to establish a manufacturable design ruleset are conservative piecewise-constant approximations. This work evaluates the effectiveness of a first-order model

for producing improved design rule-sets for feature manufacturability, accounting for process variation.

Design/methodology/approach: A framework is presented which utilizes an interpolation method and a statistical model to estimate the minimum size for a wide range of features from a set of iterative experiments.

Findings: For the considered polyamide powder bed fusion process, using this approach improves the accuracy and reliability of minimum feature size estimates for a variety of feature shapes when compared to results from an industry-standard test artifact (RMS errors reduced from 67% to 34%).

Research limitations/implications: More research is needed to provide better interpolation models, broaden applicability, and account for additional geometric and process parameters which significantly impact the results. This research focuses on manufacturability and does not address dimensional accuracy of the features produced.

Practical implications: An application to the design of thin channels in a prosthetic hand shows the utility of the results in a real-world scenario.

Originality/value: This study is among the first to investigate statistical variation of "pass/fail" features in AM process characterization; propose a means of estimating minimum feature sizes for shapes not directly tested; and incorporate a more efficient iterative experimental protocol.

Keywords: Additive Manufacturing Benchmarking, Minimum Feature Size, Design Rules

2.3 INTRODUCTION

Designing parts which can be reliably produced depends on knowledge of the manufacturing process constraints. The present study focuses on characterizing the smallest (minimum) *producible* feature size, which is an important process constraint for additive manufacturing (AM).

Minimum feature size is defined, here, as the smallest design scale for a feature having a specific shape and orientation which can be produced by the AM process, and survive removal from the machine and minimal cleanup (such as depowdering or support removal). Minimum feature size is often far larger than the manufacturer-specified precision of the machine, and the minimum producible positive (boss) feature is not the same as the corresponding negative (pocket/hole) feature.

In this study, a model and experimental process to determine minimum feature sizes for a variety of features in various orientations is proposed, evaluated, and applied to a relevant example. Currently, designers rely on conservative piecewise-constant estimates for minimum feature size to avoid AM build failures. This study benefits designers by improving the accuracy and specificity of existing estimates, and also provides a richer description for use in algorithm-driven design tools such as topology optimization.

2.4 BACKGROUND

Minimum feature size is generally assessed by manufacturing a test artifact containing “pass/fail” features at varying scales. Many researchers have designed test artifacts to assess process capabilities, including pass/fail features as one component; see for example Mahesh et al. (2004) and Yasa et al. (2014). The US National Institute of Standards and Technology (NIST) has defined a test artifact which includes vertical cylinders, holes, fins and slots; see Figure 2.1 (Moylan et al., 2014).

(a) (b) (c)

Figure 2.1. Moylan et al. (2014) test artifact. (a) CAD model, (b) manufactured, (c) resulting design rules.

Typically, pass/fail features are used to generate design rules based on the smallest feature size with "pass" quality. Figure 2.1c shows one possible set of design rules from the negative features in the Moylan artifact. Near-circular holes use one rule, and all slots use another, creating a piecewise-constant or zero order design ruleset.

Meisel and Williams (2015) evaluated pass/fail features in Moylan's test artifact on the PolyJet process, concluding that the minimum feature size is at least 10 times the process XY resolution.

Seepersad et al. (2012) and Wegner (2012) thoroughly assessed polyamide powder bed fusion processes similar to that used in the present study. In each case, hundreds of features of various sizes and shapes were manufactured in horizontal and vertical orientations to create a detailed design guide. The large number of features makes such studies expensive.

Industry groups such as Materialise mv (n.d.) also publish design guidelines for wall thickness, detail size, and minimum feature size.

Except for the more exhaustive surveys of polyamide powder bed fusion machines, pass/fail features generally use four shapes (post, hole, wall and slot); are manufactured only in vertical and sometimes horizontal orientations; and do not account for process variability. This limited information is used for broad design rules with a large safety factor.

2.5 APPROACH

This work also uses pass/fail test artifacts to assess minimum feature size. For a variety of feature shapes and orientations, copies of increasing scale are included, and each feature visually classified on a "Green-Yellow-Red" scale depending on the quality of the result, similar to Seepersad et al. (2012). The objective is to determine the smallest feature scale (set by feature thickness) which will consistently be produced at Green quality.

Three key differences exist between the present work and existing studies. First, an interpolation model provides estimates for the minimum feature size of intermediate shapes and orientations not directly surveyed. Second, the test artifact geometry is parameterized so the sizes of features included in each series can be adjusted from one manufacturing run to the next. This iterative approach increases the likelihood that each series accurately and efficiently captures the pass/fail transition point. Finally, a statistical model accounts for the variability between manufactured test artifacts and produces more reliable design rules.

A. Minimum Feature Size Interpolation

On any test artifact, a finite number of feature shapes and orientations are evaluated, but the results obtained are used as design rules for a much larger set of features. These design rules can be made more accurate by interpolating between evaluated cases (providing smooth transition between estimates for hole and slot features, for example). The underlying dynamics are process-dependent and nonlinear, so selecting an accurate model is difficult. This study explores the use of linear interpolation as the logical first-order step beyond current zero-order methods.

Consider a small arbitrary feature of a design shown in Figure 2.2a. This work selects three parameters which characterize straight features, both positive (bars and fins) and negative (holes and slots). Two aspect ratios (length/thickness r_l and thickness/width r_w) describe feature shape, and the angle between the feature axis and the build direction, ϕ, captures feature orientation (see

Figure 2.2b). Scale is controlled by setting the thickness (or diameter) of the feature. All other characteristics are held constant.

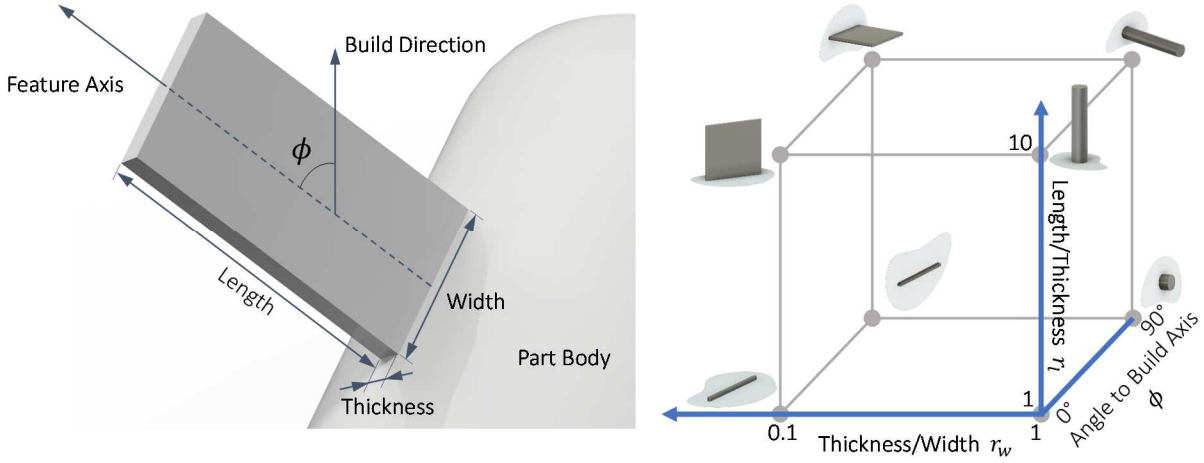

(a) (b)

Figure 2.2. Parameterization of an arbitrary straight feature. (a) Schematic (b) Parameter space

B. Test Artifact Geometry and Iteration

The test artifact evaluates the minimum feature size at all eight corners of the parameter space shown in Figure 2.2b, in both positive and negative form. For each feature type, a series of seven copies of the feature with varying feature thickness (scale) is included. The model is shown in Figure 2.3.

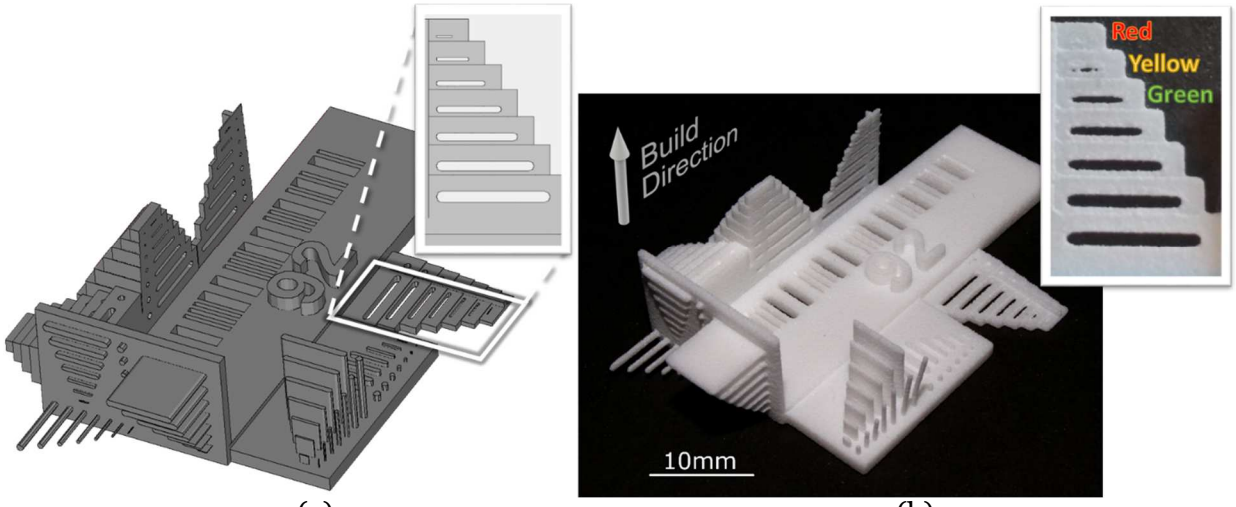

(a) (b)

Figure 2.3. First iteration test artifact for an EOS Formiga P 110: (a) Model (b) As manufactured.

After manufacture, the test artifact is visually assessed. “Green” features survived minimal post-processing and closely resemble the intended geometry. “Red” features are not produced or did not survive post-processing, and remaining features are “Yellow” (see callout of Figure 2.3b).

The test artifact model is parameterized to enable iterative refinement of feature sizes over several manufacturing runs to focus on the Green boundary. This significantly reduces the number of extraneous features that must be manufactured.

After assessment, the data from the current and previous iterations are combined, the Green boundary dimension is determined, and the range of scales for next test iteration is selected.

C. Statistical Model

An example set of results over five iterations and 10 parts (two parts per iteration) is shown in Figure 2.4. In this case, no sharp transition is found between Green and Yellow, so the underlying process is assumed to follow a logistic distribution and fit using regression (see Figure 2.4 bottom).

The feature sizes used in the next iteration of the test artifact are determined based on the 5%-95% probability in the logistic curve when a statistically reasonable fit is present. Otherwise, a heuristic algorithm adjusts the range using the results from previous iterations.

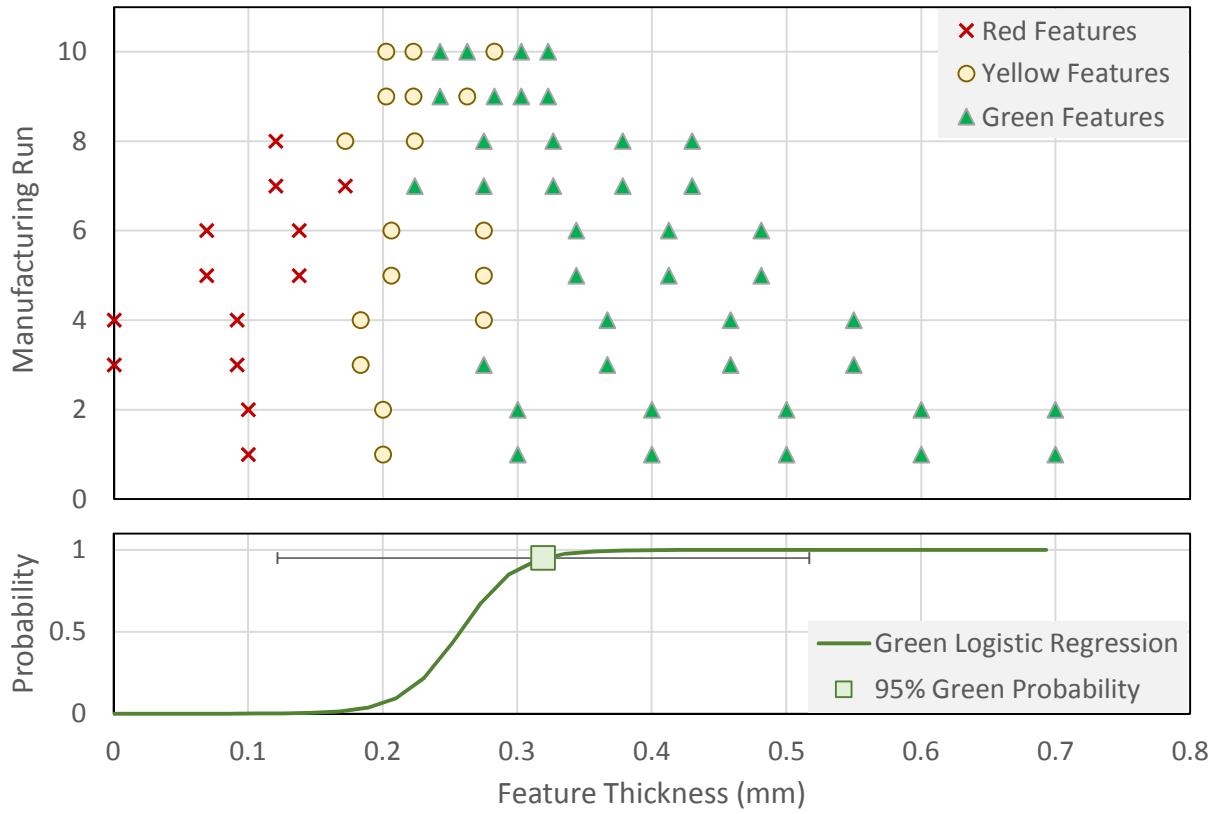

Figure 2.4. Example data (horizontal slit feature) from 10 manufactured artifacts over five iterations (top) and fitted logistic curve with 95% Green probability point shown with a 90% confidence interval (bottom).

When a logistic fit is available, the output design rule for minimum feature size is the scale at which Green probability is 95%. The transition is reported with a 90% Wald confidence interval, highlighting the uncertainty present when few trials have been used. When no probability distribution is present, the design rule is approximated from the largest Not Green thickness and the smallest Green thickness. No confidence interval is possible for this case.

2.6 Preliminary Results

The test artifact was manufactured 10 times on an EOS Formiga P 110 polyamide powder bed fusion machine using polyamide (Nylon) powder. The feature angle ϕ was evaluated at 0° (vertical) and 90° (horizontal), length/thickness r_l at 1 (boss) and 10 (bar), and thickness/width r_w at 0.1 (fin) and 1.0 (bar). Negative features had a wall thickness of 2mm. Parts were removed,

then post-processed by powder-blasting (using a sand-blasting cabinet but with unmelted powder instead of sand), and air-blasting with compressed air to remove powder from the negative features.

Figure 2.5 presents preliminary results for negative features, all of which show a Green transition well above the machine resolution (0.1mm layers and 0.05mm laser spot). High aspect ratio vertical holes require diameters over 100 times greater than the laser spot size to consistently depowder without additional post-processing, due to combined effects of heat from surrounding geometry causing over-melting and difficulty in depowdering deep holes with compressed air and powder-blasting.

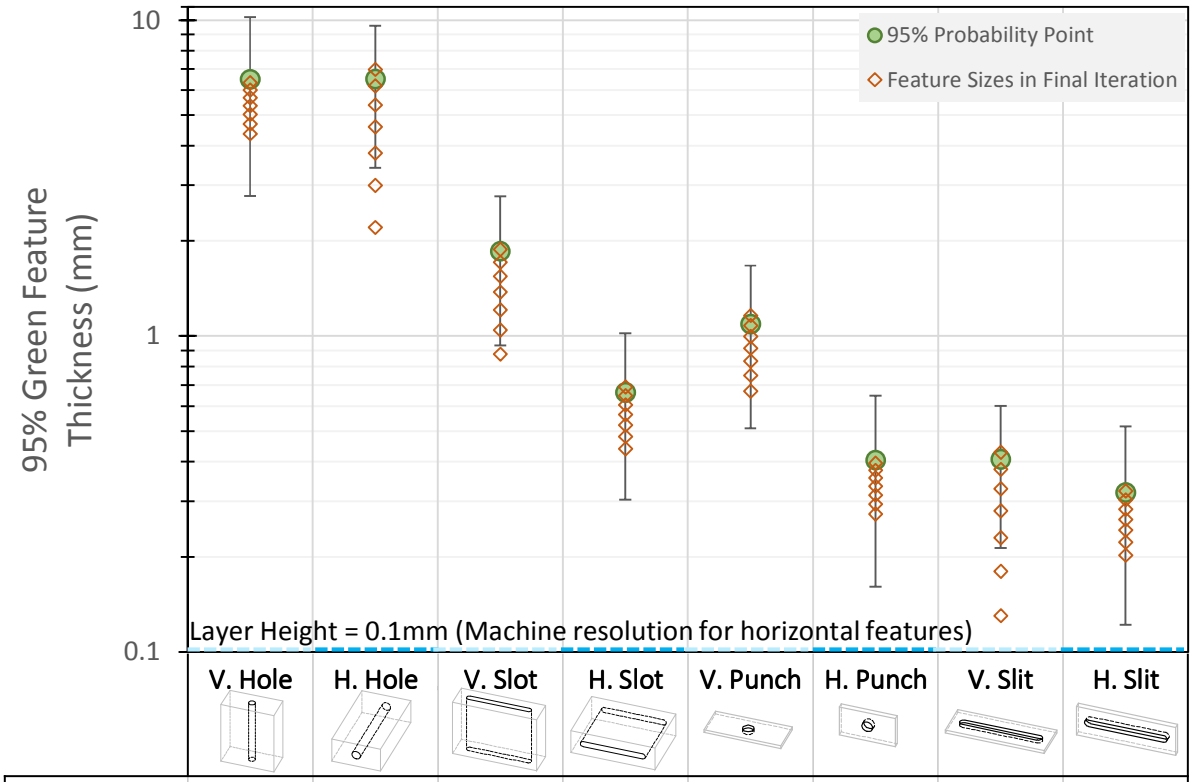

		V. Hole	H. Hole	V. Slot	H. Slot	V. Punch	H. Punch	V. Slit	H. Slit
95% pt. (mm)		6.497	6.501	1.853	0.662	1.090	0.404	0.407	0.319
± (mm)		3.722	3.095	0.919	0.359	0.580	0.243	0.194	0.197
Coordinate	r_l	10	10	10	10	1	1	1	1
	r_w	1	1	0.1	0.1	1	1	0.1	0.1
	ϕ	0°	90°	0°	90°	0°	90°	0°	90°
Green Features		22	20	35	34	32	36	38	40
Total Features		71	71	71	71	71	71	71	71

Figure 2.5. The results obtained for the negative test features on a polyamide powder bed fusion process after five iterations and 10 manufactured parts.

Two validation datasets were used to assess the interpolation model for negative features. First, a validation artifact sampling 12 points distributed around the center of the shape/orientation space was manufactured iteratively to measure the actual 95% Green transitions. The resulting transitions were predicted by the trilinear interpolation with 39% RMS error (worst was 95%). In seven of the 12 cases, the validation data point lay within the confidence interval of the estimate.

A second validation dataset consisted of 80 iterative feature size measurements distributed along the edges of the parameter space. 85% of the Green transitions lay in the confidence interval of the linear interpolation, with an RMS error of 34% (worst was 128%). If the results from the features on the NIST test artifact were used instead, the RMS and maximum errors would be 67% and 215%, respectively. This represents a 2X improvement in the accuracy of the estimate.

2.7 APPLICATION

As an example application, consider the palm of the Phoenix Hand v2 (EnableCommunityFoundation, 2016). Six long, curving tubes 2.3mm in diameter for routing cables are highlighted in Figure 2.6a.

A design rule based on the NIST test artifact in Figure 2.1 would indicate a 2mm hole should be manufacturable, but removing powder from the tubes is nearly impossible, even with additional post-processing.

After using the interpolation function to determine the maximum allowable aspect ratio for each channel, appropriate cleanouts were inserted (Figure 2.6b). The revised model was manufactured and successfully depowdered (Figure 2.6c).

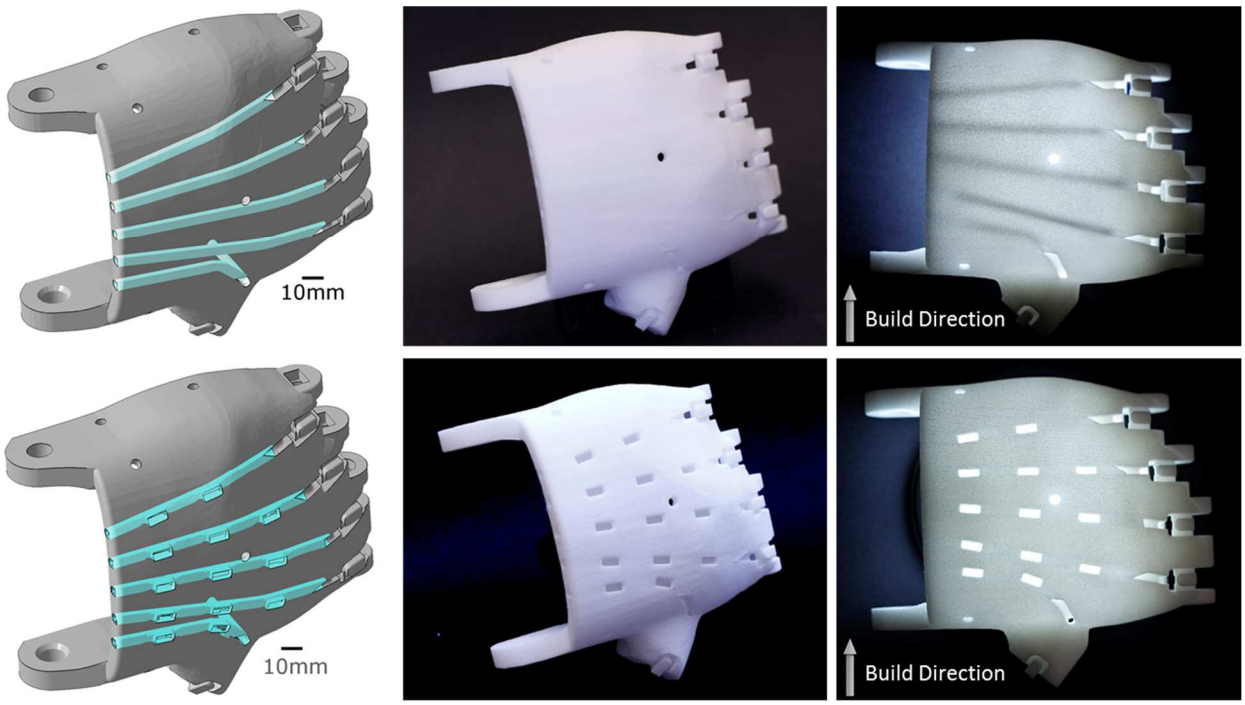

Figure 2.6. The Phoenix Hand (Top: original. Bottom: modified) (a) models with tubes highlighted (b) manufactured parts (c) backlit manufactured parts (note dark regions of un-melted powder). Model from (EnableCommunityFoundation, 2016).

All the studies presented here used the same wall thickness, feature shape, and orientation with respect to the feature axis, and each of these variables has an effect on the minimum feature size. For example, if the hand is printed palm-down, the larger in-plane wall thickness causes the channels to over-melt, and depowdering of the revised model is more difficult.

2.8 Conclusion

A method of evaluating and interpolating the minimum producible feature size for small straight features in a variety of shapes and orientations has been proposed and validated for negative features in a polyamide powder bed fusion process. The method improves on prior studies by capturing statistical variation and interpolating between measurements to estimate different shapes and orientations. It represents a 2X improvement in the accuracy of the estimate over those using an NIST test artifact (RMS error dropped from 67% to 34%).

The focus was on which design dimensions produce visually acceptable geometries; dimensional accuracy is not examined. The statistical model used to account for process variability is sensitive to outliers and the assumption of a logistic distribution to the data may not be satisfied for features in some situations; vertical pillars in polyamide powder bed fusion, for example, exhibit infrequent failures not correlated with diameter.

Higher order models could further improve prediction accuracy by incorporating process physics and additional geometry and orientation parameters. Benefits of this research direction include enhanced design rules for human and algorithmic designers leading to reduced waste from manufacturing failures.

Chapter 3. Towards a General Method for Constructing Manufacturability Design Rules for an Additive Manufacturing Process

3.1 Preface

Chapter 2 presented a method for determining minimum feature size experimentally by manufacturing a series of test artifacts. In Chapter 3, this approach is extended and applied to two new AM processes. A more systematic design of experiments (DOE) is used to frame the experiment with an eye towards developing design rules for an example machine in each of the material extrusion and vat photopolymerization AM process categories, which are expected to have much more complex behavior because overhang angle plays a significant role. The DOE framework employed enables a retrospective analysis of the results for varying sizes of experiment, answering important questions about the tradeoffs between how much data should be collected and the quality of the resulting design rule. The parametric design rule functions produced are used in Chapter 4 to ensure manufacturability of the outputs of a topology optimization automated design framework.

3.2 Abstract

Additive manufacturing (AM) presents a unique set of manufacturability constraints, among the most important of which are the smallest producible feature size and the maximum overhang angle before support structures are required. In this work, a parameterization for small features and an iterative experiment are used to realize minimum feature size design rules as functions of feature shape and orientation in a general manner applicable to a wide variety of processes. The technique is applied to an example machine in each of the material extrusion and vat photopolymerization AM process categories, finding that minimum feature size can vary by as

much as 10x over the set of considered oriented shapes. A thorough experimental evaluation explores the tradeoffs between the number of oriented shapes evaluated and the predictive quality of the resulting design rules. Compared to existing design rules based on a single minimum feature size and overhang angle, this work increases the design space by incorporating the overhang angle constraint into the minimum feature size definition, detects un-manufacturable features that existing design rules would have incorrectly allowed; and provides lower minimum feature sizes for other shapes and orientations by as much as 60%. A procedure to replicate the experiment on the interested reader's own AM process is included.

Keywords: Additive Manufacturing Benchmarking, Minimum Feature Size, Design Rules

3.3 INTRODUCTION

Additive manufacturing (AM), in which an object is built in a layer-by-layer fashion, has become an increasingly popular manufacturing technology, with applications from conceptual visualization through production manufacturing (Thompson et al., 2016). Among the key advantages of AM is its independence from design constraints driven by manufacturability requirements associated with other, more traditional, means of making physical objects such as casting, molding and machining (Hague et al., 2004). These relaxed constraints create new freedoms for the designer and have opened the door for new design paradigms to realize more effective products, including topology optimization, which produces organic shapes nearly impossible to manufacture by conventional (non-AM) means.

Additive manufacturing comes with its own, unique, set of manufacturability constraints, however, which have been studied by various researchers, including Chu et al. (2008), Meisel and Williams (2015), and Ponche et al. (2014). Two of the most studied design constraints for AM are the overhang angle, which represents the shallowest downward-facing surface which can survive manufacturing without support, and the minimum feature size, which quantifies the dimensions

of the smallest element of a design which can be realized on a particular process. A single overhang angle (in degrees elevation above the build plane or degrees of declination from the build axis), and one or several minimum feature size(s) (usually expressed in millimeters for various structures, such as walls, holes, etc.) are typically used to characterize the manufacturing capabilities of a particular process/material combination. These quantities are provided by the machine manufacturer ("Design Guidelines: Fused Deposition Modeling (FDM)," n.d.), by a researcher working on a similar process (Thomas, 2009), or by manufacturing and analyzing a carefully designed test artifact (Moylan et al., 2014).

These manufacturing constraints are provided as guidelines to the designer, but the true behavior of the process is more complex, and through trial-and-error experience, designers learn when they can break the rules. For example, in the considered material extrusion process, overhang angle is often violated deliberately by a designer when a flat element is supported at both ends (known as "bridging", see Figure 3.1).

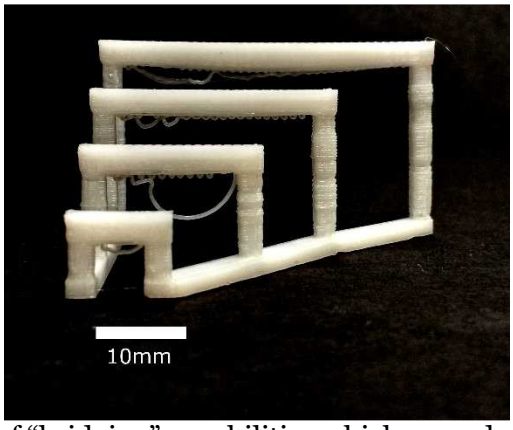

Figure 3.1. Demonstration of "bridging" capabilities which exceed overhang angle requirements but are still manufacturable Process: Hot PLA material extrusion

Minimum feature size also varies with the shape and orientation of the feature, making a single design rule difficult to obtain with confidence, as explored by various researchers (Kranz et al., 2015; Seepersad et al., 2012; Wegner and Witt, 2012). Positive (boss) features and negative (hole) features have different minimum feature size because they depend on different characteristics of the process. Minimum feature size for positive features is restricted by the

deposition/fusion/solidification size and layer height, whereas negative features depend on the deposition/solidification accuracy of the machine. In both cases, the material, process parameters, and underlying physics have significant effects. Small positive features might be larger than the bead size and the layer height but still be unable to support their own weight after manufacturing, resulting in warping or breakage. Small negative features can be blocked by material over-deposition in surrounding geometry, and difficulty in removing uncured build material (in powder and liquid feedstock processes) can both be far more significant than the machine's positioning resolution.

Accurately characterizing the overhang angle and minimum feature size throughout a broad set of feature configurations is important for the AM ecosystem. If the minimum feature size and overhang angle design rules are overly conservative, opportunities to leverage the full capability for product complexity are lost. If design rules are selected without fully evaluating a range of features, however, the results may give an unrealistically optimistic view of the process, resulting in designs which fail in manufacture, wasting time and money. As designers seek to push the boundaries of AM processes, and especially in processes where trial-and-error design iterations are costly, more robust design rules must be developed. In previous work, the authors reported on an initial study quantifying the minimum feature size for a powder bed fusion process using Polyamide powder, finding that the shape and orientation of negative features could change the minimum manufacturable size by an order of magnitude, especially for negative features (Weiss et al., 2018).

With this as motivation, the present work presents a general framework for determining the minimum feature size as a function of shape and orientation on minimum feature size for any AM process. The approach is applied to example AM processes from the material extrusion and vat photopolymerization categories, and results are reported and discussed. Specific contributions of this paper include the following:

- Overhang angle and minimum feature size are combined into a single, richer design ruleset based on the minimum manufacturable scale[1] for features of various shapes and orientations.
- An adaptive, iterative approach for obtaining high quality minimum feature size estimates on any AM process is presented.
- The size of the experiment can be adjusted based on the user-desired level of expense and machine time, and the tradeoff between experiment size and predictive accuracy of the design rules is explored for considered AM processes.

In the next section, a brief overview of relevant literature is presented. Following that, the proposed general experimental procedure for determining the minimum feature size for a given printer is detailed in Section 3.5; implementation details for the specific experiments performed are provided in Section 3.6; and results are shown in Section 3.7. Conclusions drawn from the results form the basis for two application examples in Section 3.8. Finally, Section 3.9 provides details on adapting the process to the reader's own AM processes.

3.4 Background

A great deal of research has sought to establish design rules for additive manufacturing processes. Dimensional and geometric accuracy, surface finish, minimum feature size, and overhang angle have all been explored by various researchers, either for comparing different AM processes based on their capabilities, or for generating design rules for a specific process. Overhang angle is relatively straightforward to assess, and has received comparatively little attention from the research community. This section begins with a brief survey of overhang angle studies, followed by a more detailed review of works assessing minimum feature size.

A. Overhang Angle Assessment

Maximum overhang angle is generally evaluated using a test artifact, which manufactures a specific geometry at various orientations. After manufacturing, the artifact is evaluated, and the

[1] Minimum feature scale is used interchangeably with minimum feature size in this text and refers to the smallest uniform scaling of an shape in a particular orientation which can survive manufacturing and minimal post-processing.

most inclined feature which is classified as “manufactured acceptably” is used to set the design rule.

Overhang angle is of less concern in powder-based processes (such as binder jetting and powder bed fusion), but in metal additive manufacturing, heat transfer and warping cause overhanging features to perform poorly. Castillo (2005) and Yasa (2014) address overhang features in metal AM, utilizing an “open book” structure with sheets of material extending into the volume at different angles, and Mertens et al. (2014) assesses and optimizes machine parameters for down-facing structures in a metal powder bed fusion process, concluding that an overhang angle of 45° is tolerated.

Johnson et al. (2011) includes overhanging features in a test artifact designed for a material extrusion AM process and reports that 45° is manufacturable while 50° from the build axis shows significant deformation, while Nelaturi et al. (2015) uses a theoretical argument to set the overhang angle as the arctangent of the ratio of extrusion nozzle diameter to the layer height.

B. Minimum Feature Size Assessment

Characterizing minimum feature size and overhang angle have received the attention of a variety of research efforts, but few summaries of the literature focusing only on this topic are available. Most design rules rely on a combination of expert knowledge and test artifacts, which characterize the ability of a particular process to produce features of a given size. The use of test artifacts is advantageous because it evaluates the entire system, characterizing a specific combination of materials, mechanics, physics of deposition/fusion, software, and process settings.

However, the wide variety of processes make designing a single test artifact which is applicable across the spectrum of AM very difficult. Also, assessment of results is made tedious because the anisotropy of the underlying process requires tests to be run in multiple orientations in order to fully characterize each type of feature. Further repetitions are required if information on the statistical variation of the process is desired.

Test artifacts which characterize minimum feature size generally do so by including a series of so-called "pass/fail" features of successively smaller characteristic dimensions, then using some kind of inspection (usually visual) to classify features as to the process's ability to manufacture them "acceptably". Studies generally focus on comparing processes (for process selection) or on a single process (for design rule generation).

C. Studies focusing on multiple processes

Some researchers have explored smallest producible features over a range of processes to inform process selection decisions or in an attempt to create a generic test artifact which can be used on multiple platforms. Using benchmark parts to compare multiple processes began early in the days of additive manufacturing (Kruth, 1991), and follows from similar techniques in other manufacturing domains, for example ISO 10791-7 (2014). Most of the studies surveyed in this section include pass/fail features as one piece of a larger test artifact designed to measure dimensional accuracy, geometric accuracy, surface finish and/or other machine characteristics.

Xu et al. (2001) and Mahesh et al. (2004), both from the National University of Singapore, each published results from different test parts manufactured on four different AM platforms which included a small series of pass/fail features. They visually inspected each part after manufacturing and classified features as "successful" or "unsuccessful".

Byun and Lee (2003) used an algorithm to lay out features of differing shapes in a test matrix, and included 4 sets of pins and holes (both rectangular and circular), as well as walls in pass/fail feature tests on four printers. In 2005, Kruth et al. evaluated the ability of several powder bed fusion processes to produce fine features using a series of circular holes, cylinders, and walls in a test part also designed to evaluate surface finish, dimensional accuracy, and mechanical properties (Kruth et al., 2005). Later, Yasa et al. built on Kruth's test artifact, introducing additional pass/fail features as well as fins at various angles from the build plane (Yasa et al., 2014).

Moylan et al., with the US National Institute of Standards and Technology (NIST), surveyed existing test artifacts and proposed one of their own design for standardization (Moylan et al., 2014). It includes vertically-oriented circular cylinders/holes as well as fins/slots which are evaluated by optical microscope. Figure 3.2 shows this section of the NIST part in both digital and manufactured form.

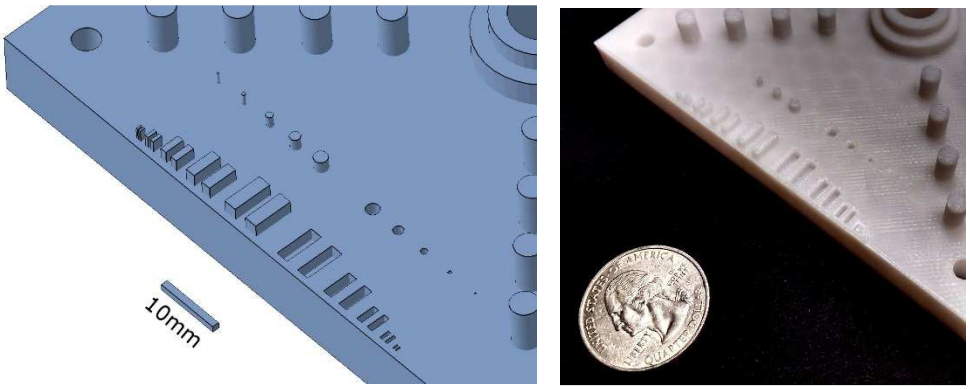

(a) (b)

Figure 3.2. NIST Test Artifact. (a) CAD model (b) as manufactured on a hot PLA material extrusion AM process.

D. Studies focusing on a specific process

Restricting the study to a single process (and often a single machine) generates process knowledge suitable for use in parameter optimization and generating design guidelines.

Some researchers combine experimental evaluation with process models. For example, Ponche et al. uses multiphysics modeling of the additive laser melting process combined with experimental evaluation of a test artifact to generate both quantitative predictions of minimum wall thickness and qualitative relationships between certain geometries and defects which are used as input to a topology optimization process (Ponche et al., 2014).

Another advantage of focusing on a single process is the flexibility to explore materials and process parameter spaces. Meisel and Williams (2015) explored the minimum sizes of small positive and negative circular and rectangular features on the PolyJet process, characterizing the effect of different materials and process parameters. Despite the PolyJet process's theoretical X/Y accuracy of 42 μm, their experiments indicate that the minimum feature size is anywhere between

372 μm and 897 μm, depending on feature geometry, material, and process settings. They recommend using 897 μm (21 times the X/Y accuracy) as a design rule that works in the worst case, unless care is taken to control material and other parameters. Meisel and Williams also are among a very small number of studies to consider the statistical variation of pass/fail features.

A few researchers have performed thorough assessments of polyamide powder bed fusion machines utilizing plastic powder feedstocks (Govett et al., 2012; Seepersad et al., 2012; Wegner and Witt, 2012). In each study, 5 or more test artifacts, each containing as many as 150 features, were manufactured in different orientations to explore a variety of fine features and functional components, reporting both build success and (in some cases) dimensional variation for each feature in order to help create a detailed design guide for various features. Seepersad et al. and Govett et al. both utilized a "red-yellow-green" traffic light scale for reporting printing success. The large number of parts to be manufactured and features to be evaluated make these studies very expensive and time consuming, but provide value to readers by surveying a much wider set of features with a high level of detail. The large number of different features surveyed also means the cost of producing multiple copies in order to estimate process variability is generally prohibitive. An open question not addressed in these works is how many levels of each feature parameter (variations in diameter or length, for example) must be included to provide predictive design rules.

Because human designers can incorporate both qualitative and quantitative design guidelines, some efforts have combined test artifact results with expert knowledge to produce guidelines covering a broad range of issues important to design for additive manufacturing (DFAM), (Kranz et al., 2015; Thomas, 2009). Of particular interest to the present study, Kranz et al. includes bar and fin features at several angles above the build plane along with a variety of lengths in his analysis.

Although the raw results are rarely disclosed, industry frequently publishes design guidelines including "rule-of-thumb" values for wall thickness, detail size, and sometimes

minimum feature size, in addition to a wide variety of suggestions for changes which make designs more manufacturable on the company's equipment. See, for example, ("Design Guidelines: Fused Deposition Modeling (FDM)," n.d., "Design rules and detail resolution for SLS 3D printing," n.d.; Materialise mv, n.d.).

E. Summary

Generally, pass/fail features fall into four categories (Post, Hole, Fin/wall and Slot/gap) and are printed in the vertical (build axis) and possibly also horizontal (build plane) orientations. Many of the parts in existing literature include only 3-10 pass/fail features when minimum feature size is only one component of the study, while others which seek to explore a larger design space require many hundreds of features.

A summary of the pass/fail features in four common forms is shown in Table 3.1. Post and Hole features refer to square or round cross-section cylindrical structures (conversely cylindrical holes) with base dimensions between 0.5mm and 2.0mm and length/base aspect ratios generally greater than 2. Some studies include posts supported on both ends, and others use posts cantilevered from the supporting body; similarly, some studies use through holes while others choose blind holes. Most commonly, the features are manufactured only vertically (feature axis parallel to the build direction) and horizontally (feature axis in build plane), though Kranz et al. (2015) includes angled posts and Wegner and Witt (2012) includes one set of posts at 45° from the build plane.

Fins are thin plates on the test part; slots denote rectangular channels. Walls and gaps are similar, except for the support of one or more sides (or access for slots). There is variation among studies in height and depth, as well as doubly-supported or simply supported (for holes, through and blind) configurations. As with Posts and Holes, they are usually manufactured only in horizontal and vertical configurations. Although some studies include slanted planes, the focus is

generally on surface finish rather than minimum plane thickness. Generally, thickness of fins and slots is varied between 0.1mm and 1.0mm.

Evaluation of the smallest manufacturable size of a feature of arbitrary shape and orientation using any of the approaches discussed above requires the use of very large or many test artifacts which contain pass/fail features of several possible sizes in each of a variety of shapes and orientations (Weiss et al., 2018). Because the lower limit of a process containing random variables is being evaluated, multiple copies of each test feature must be included on the artifact or the artifact must be produced repeatedly, as evidenced in Meisel and Williams (2015). Using any of the above approaches for even a simple set of real-world features therefore requires an exponentially-large set of tests. As a result, most designers utilize a small set of rules of thumb, which include a significant factor of safety over the process's real lower limits to account for variables not captured in the experimental evaluation.

Table 3.1. Comparison of number and range of simple pass/fail geometries in selected test artifacts.

Work	Process & Material	Positive		Negative	
		Pins	Fins/Walls	Holes	Slots/Gaps
Mahesh (2004); Mahesh et al. (2004)	Various	1 (0.5mm)	3 (0.5- 2mm)	4 (0.5-3mm)	4 (0.5-3mm)
Byun and Lee (2003)	Various	---------- 4 (0.2, 0.5, 1.0, 2.0mm) ----------			(none)
Meisel and Williams (2015)	PolyJet	10 (0.1-1.0 mm)	10 (0.1-1mm)	10 (0.1-1mm)	10 (0.1-1mm)
Yasa et al. (2014) builds on Kruth et al. (2005)	Metal powder bed fusion	4 (0.5-5mm)	3 (0.25-1mm)	4 (0.5-5mm)	(none)
Moylan et al. (2014)	Various	5 (0.25 - 2mm)	5 (0.25-2mm)	5 (0.25-2mm)	5 (0.25-2mm)
Govett et al. (2012) Seepersad et al. (2012)	Poly-amide powder bed fusion	15 (0.2-3mm)	15 (0.2-3.0mm)	147 (0.125-4.0mm)	
Wegner and Witt (2012)	Polyamide powder bed fusion	60 (0.6-2mm)	76 (0.2-2mm)	Not reported	
Our approach, building on Weiss et al. (2018)	Various	6 copies of a carefully selected set of feature types (iteratively adapts feature size on successive test parts)			

3.5 APPROACH

In light of the survey of the literature presented above, this work proposes a cross-platform experiment for efficiently determining a functional relationship between shape, orientation, and minimum feature size. In doing so, it builds upon the process previously reported in Weiss et al. (2018), the salient details of which are repeated as appropriate in the current presentation.

The set of studied small features is parameterized as a set of fins of different aspect ratios (shapes) and angle from the vertical (orientation), in addition to an identical complimentary

analysis of slots. The parameterization selected uses Length/Thickness (r_l), Thickness/Width[2] ("r_w", where $r_w = 1$ corresponds to a bar) and angle from the vertical ("ϕ", where $\phi = 0$ indicates a feature whose axis is parallel with the build direction). Fins are assumed rectangular, and the angle of the fin about the feature axis is fixed (i.e. the extreme edge of each fin is parallel to the build plate), see Figure 3.3a. The parameter space produced, visualized in Figure 3.3b, covers a large set of common design features, and a similar parameter space for negative (hole/slot) features is also created.

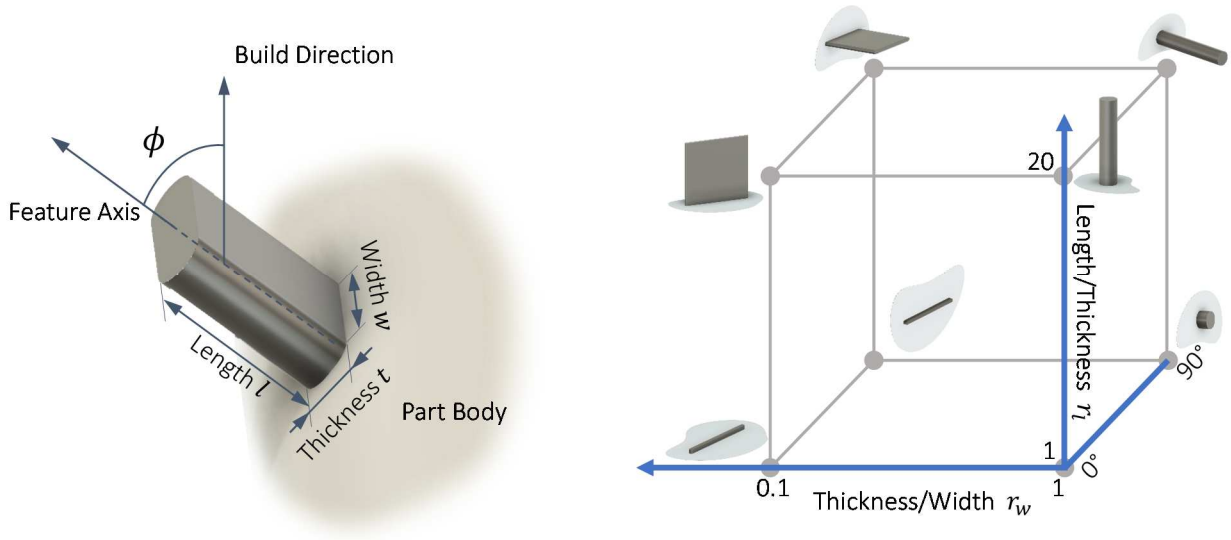

(a) (b)

Figure 3.3. Parameter space of features considered in this study.

Three research questions posed in this experiment:

1. Can a function, fit over this parameter space, be used as a more complete design rule for manufacturability, generally over different AM processes?
2. How does the amount of data collected and the complexity of the fitting function affect the ability to predict design rules for oriented shapes not directly studied?
3. Will the process implicitly incorporate an overhang angle restriction by returning prohibitively large minimum feature sizes at high overhang angle?

[2] Thickness/Width is selected instead of Width/Thickness because it maps the asymptotic behavior of a progressively wider fin (which one expects to converge to a single design rule as the ratio becomes increasingly large) to a smaller and smaller number, making a linear fit more nearly predictive, and causing the experiment to sample fins in the more interesting region near the cylinder end.

Research Question 1 extends the initial investigation of Weiss et al. to a general framework for other processes which have different behavior resulting from different process physics and failure modes. Research Question 2 seeks to understand the number of oriented shapes that must be evaluated in order for the fitting surface created from the data to be effective in predicting the minimum feature size for other features not directly included in the experiment. Research Question 3 hypothesizes that the overhang angle constraint, normally considered separately in material extrusion and vat photopolymerization processes, can be integrated into the minimum feature size function, reducing the difficulty of applying design rules.

To answer these questions, an experiment was designed and performed following the high-level procedure in Figure 3.4, which simplifies the process slightly for clarity; details of the actual implementation are covered in the following subsections. In Figure 3.4a, a high-level *Experiment Design* is carried out which selects points in the parameter space of small features to evaluate for minimum feature size (a simplified, two-parameter space is used in the figure). Each point selected in the high-level experiment defines a particular shape and orientation of feature (Figure 3.4b), and the goal is to determine the smallest scale (i.e. the smallest thickness t) at which the feature can be consistently manufactured. To do this, the feature is replicated six times at different scales on a test artifact in the *Artifact Definition and Generation* step, using initial guesses for the minimum and maximum thickness derived from manufacturer specifications or user judgement (Figure 3.4c). This test artifact is *Manufactured and Evaluated* (Figure 3.4d), and the user codes each feature as successful or unsuccessful (indicated by the "√" and "x" symbols). Based on the results, a new set of minimum and maximum scales is specified and a new artifact is defined, a process described in the *Iteration* subsection below. This occurs a set number of times (the question of how many times it should occur is addressed later in this work), after which all collected data for the current oriented shape is combined and used to estimate a minimum feature size based the probability of a feature being successfully manufactured (shown in Figure 3.4e).

The minimum feature size values for each individual oriented shape sampled are combined in the *Design Rule Definition* phase, in which a function is fit to the data creating a predictive design rule.

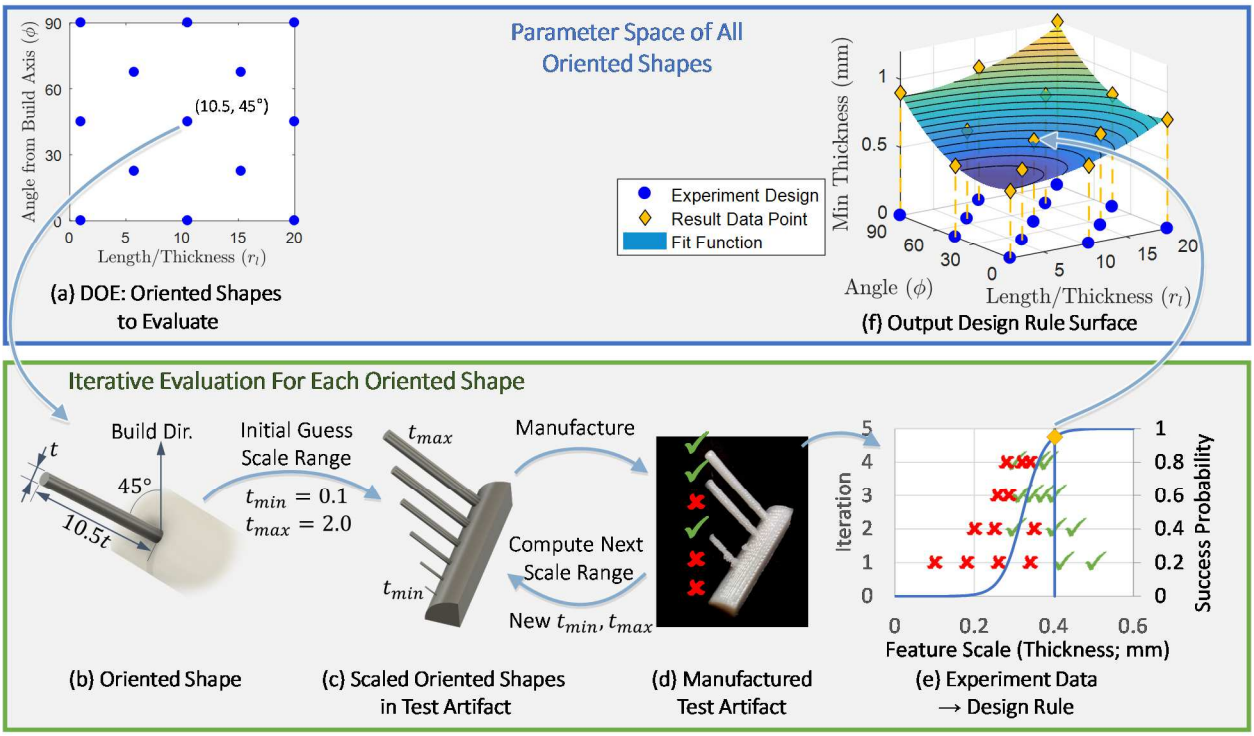

Figure 3.4. Overview of the (simplified) experimental procedure followed. Top box (frames (a) and (f)) indicate steps associated with the high-level experiment over a wide range of orientations and shapes. Bottom box (b-e) shows a low-level procedure for evaluating each individual sample of the higher-level experiment.

A. Focusing Assumptions

For the purposes of this research, several assumptions are explicitly made in this experimental setup to reduce noise and improve tractability.

- To keep the size of the parameter space of small features manageable, only straight, small cylindrical and rectangular features are considered, and rectangular features are assumed to be "level" with the build plate (no rotation about the feature axis).
- It is assumed that as the scale of a feature increases, it is more likely to be manufactured successfully, and that this relationship can be modeled with a logistic ("S"-shaped) function. This approach will struggle when the AM process allows random failures of features of any size, or if the bending stress in long features during post processing rises faster than the increased strength from larger base thicknesses can overcome it.
- The experiments are performed on only one machine (per process), with consistent settings, operating procedures, or post-processing regimens.

- Because the determination of which features are "successful" is made by a human user, assessment is done by a single designer in each case to avoid differences in interpretation.
- Features which are entirely in the build plane (i.e. the feature axis is horizontal) are supported at both ends so as to realize the "bridging" effect shown in Figure 3.1.
- Finally, neither strength nor geometric accuracy of the resulting features is considered when scoring, only the visual similarity between the design and the manufactured product.

Under these assumptions, the experimental approach shown in Figure 3.4 is described in detail in the following subsections.

B. Experiment Design

A design of experiment (DOE) process is used to select which coordinates (data points) in the parameter space should be evaluated. Two types of data points are desired, "training" points which are used to define the design rule functions, and "test" data points at different locations which will be used to evaluate the predictive ability of the design rules at different points. The training points are selected using the Maximum Entropy Design (MED) method (Li, 2007; Shewry and Wynn, 1987). In MED design, an ordered list of points to sample is produced, with each point placed so as to minimize an entropy measure when combined with all previously sampled points. The definition of entropy used arises out of information theory and Bayesian statistics and is not reproduced here, but several example MED designs are shown in Figure 3.5. If some data is already known, MED can use this information as a prior, providing additional data points to sample in light of the preexisting information (see Figure 3.5b). As a result of the MED construction, any sub-experiment consisting of the first N entries in the main MED experiment is itself a valid MED design. This allows the analysis to examine the quality of fit achievable using different sized subsets of the data without violating the integrity of the design or the quality of the results, in support of Research Question 2. The experiment presented here consists of 76 MED data points.

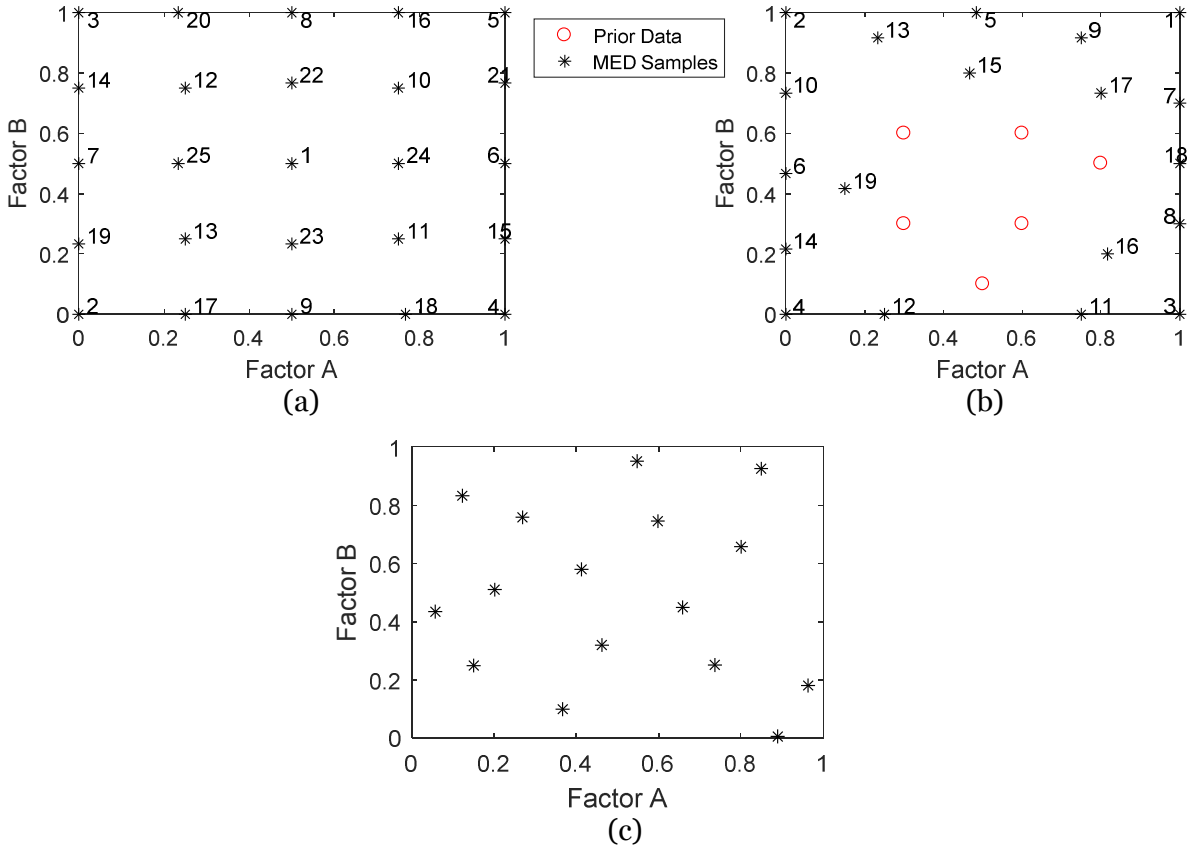

Figure 3.5. Examples of experiment designs. Numbers indicate order of the data points. (a) MED experiment with no prior data. (b) MED experiment with prior data. (c) Latin Hypercube experiment design

The "test" sample locations, which are used to evaluate the quality of the design rule functions at points not included in the training dataset, is constructed using the popular Latin Hypercube design method (Wang and Shan, 2007). The Latin Hypercube design evenly and randomly distributes the sample points across the design space, maximizing the distribution uniformity when collapsed to each coordinate axis (see Figure 3.5c for an example). This experiment uses 32 Latin Hypercube data points for testing.

C. Artifact Definition and Generation

Each of the data points selected in the training and test data sets must have its minimum feature size evaluated using the process laid out in Figure 3.4b-e. The experiment is carried out for both positive and negative features, so in addition to the positive (bar) features shown in Figure 3.4, a

similar experiment evaluates holes of the same shape and orientation. Note that the minimum and maximum thicknesses for the positive and negative features vary independently.

The scale for each feature is controlled by varying the thickness, t (see Figure 3.6). For each oriented shape being evaluated, the aspect ratios of length and width to thickness (i.e. the r_l and r_w) as well as the orientation (overhang angle ϕ) are fixed (since these define a single oriented shape in the parameter space), and the size (scale) of each individual feature is set by selecting an appropriate thickness. A series of six scales of the oriented shape are included on the test artifact which linearly interpolate between a minimum and maximum scale (defined by thicknesses t_{min} and t_{max}). The maximum and minimum scale will be adjusted after each time the artifact is manufactured and evaluated, as described in the *Iteration* subsection.

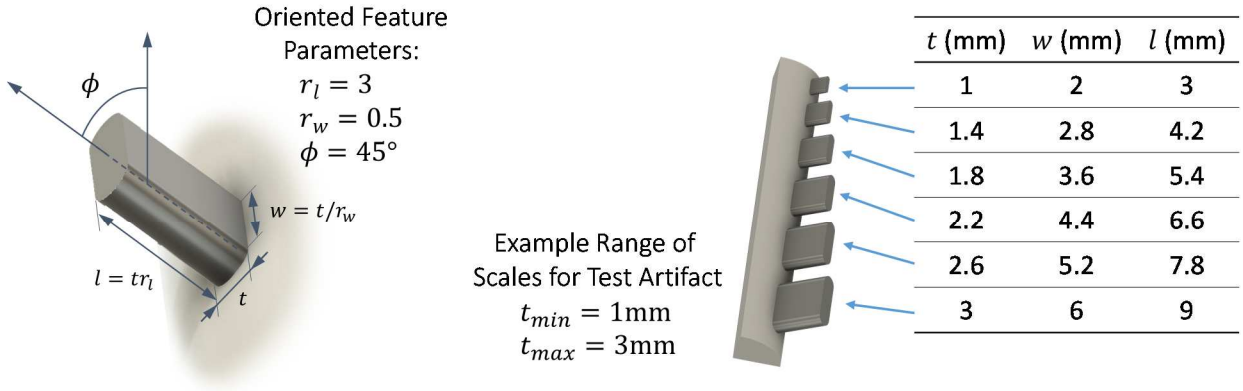

t (mm)	w (mm)	l (mm)
1	2	3
1.4	2.8	4.2
1.8	3.6	5.4
2.2	4.4	6.6
2.6	5.2	7.8
3	6	9

Figure 3.6. Illustration of thickness as the parameter which controls scale. (a) An example oriented feature (which specifies aspect ratios and overhang angle, but not scale), and (b) the same oriented feature manifested in several scales by varying thickness t. Note that all numeric dimensions are for illustration only; actual dimensions vary in successive iterations of the test artifact.

For efficiency, instead of manufacturing a single test artifact for each oriented shape (as shown in Figure 3.4c and in Figure 3.6b for simplicity), 5-7 oriented shapes are grouped into artifacts which can evaluate them all at once (recall that each oriented shape is replicated six times

at different scales, so each test artifact contains between 30 and 42 individual features).[3] Figure 3.7 shows an example of four test artifacts containing a variety of features in both positive and negative form.

Initially, the range of scales for all positive features is set using an initial guess for t_{min} and t_{max}, with negative scales selected at a different initial range, based on the best judgement of the operator. The definition of the artifact geometry is performed using a parametric model built in OpenSCAD (Kintel, n.d.), which generates an STL definition of the solid. Negative features are realized as through-holes surrounded by a fixed amount of geometry, and the model also defines a base plate to adhere to the build plane and supports for bridging positive features. Serial numbering is included to aid in experiment organization.

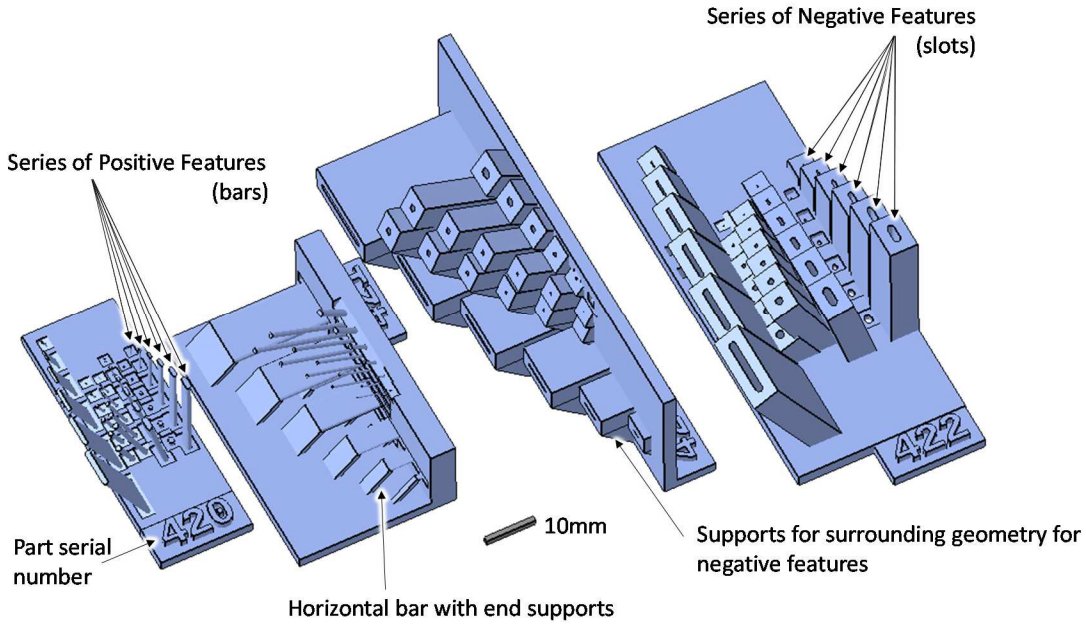

Figure 3.7. An example group of test artifacts, encoding 6 scales each of 12 features in both positive and negative form. The range of scales of each feature is updated at successive iterations based on past results.

[3] When originally designing the experiment, features were grouped into sets of 12, then each group was divided into a set of 5-7 features above and below a 45° overhang, which were arranged onto two halves of a test artifact. Later, the two halves were separated into two different artifacts to ease layout on the build platform. In the experiments reported here, the selected oriented shapes to include in each feature was randomized, then sorted by angle.

D. Manufacture and Evaluation of the Test Artifacts

Each test artifact is manufactured on the target process. In most cases the artifact should be producible without generating additional supports. After manufacturing and a specified minimal post-processing (such as removal from the build plate or minimal cleaning), each feature is visually assessed and scored according to its reproduction of the original design. “Acceptable” or “Pass” features are defined as ones in which material fills the original feature in the intended shape. The exact characteristics of an acceptable feature are left to the user to determine; the procedure provided here does not require a particular definition of passing or failing.

E. Iteration

After the first manufacturing run, the scores of the individual features are recorded and used to determine the next range of feature scales to use. In subsequent iterations, all of the data for a particular shape and orientation coordinate is combined to select the next range of features.

When sufficient data is present, regression is used to fit a logistic function to the features, providing a continuous estimate for the probability of feature success over the range of scales (bottom row, Figure 3.8). When a logistic fit is possible, the next range of scales to investigate is selected as the range between 5% probability and 95% probability.

When a reasonable logistic fit is not possible, either because too little data has been collected or because the passing and failed features are completely separated[4], a heuristic is used (see top row, Figure 3.8). The heuristic first tries to center the pass/failure transition point in the range of sampled features, then zooms in on the transition in order to more accurately estimate the transition point. Details of the heuristic function used can be found in Appendix A.

[4] “Complete separation” in the context of logistic regression refers to the case where the “passing” and “failing” data points can be divided perfectly by picking an appropriate threshold (even allowing one or more “pass” and “fail” data points exactly on the threshold). In this case, more than one logistic regression can fit the data exactly, and the steepness of the transition becomes unbounded.

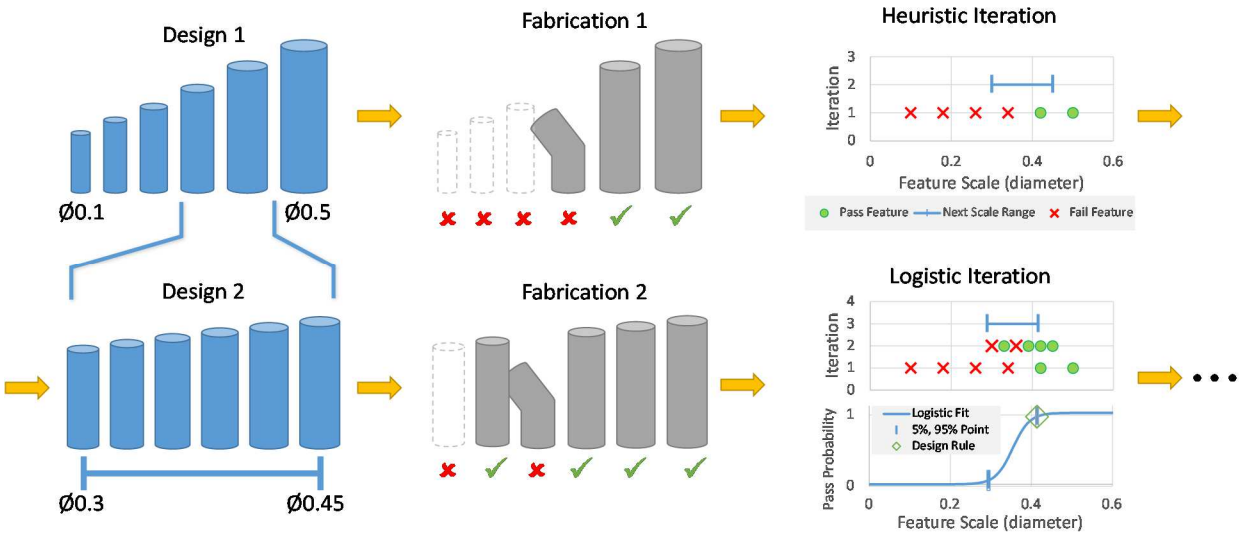

Figure 3.8. The Iteration Process. When insufficient data or complete separation between the passing and failed features sampled is present, a heuristic approach is taken to determine the next set of scales to evaluate. When a logistic fit is possible, the next range of scales is selected as the 5%-95% probability range.

F. Design Rule Definition

After a set number of iterations, the data for each shape and orientation coordinate is combined using logistic regression to a single minimum feature scale, the scale at which features have a 95% probability of successful manufacture (see diamond in bottom plot, Figure 3.8). If a reasonable logistic fit is still not possible, a heuristic is used to determine the minimum feature scale. Thus, a single minimum feature scale (thickness) for each oriented shape specified in the original DOE is produced through the iterative manufacturing and evaluation of the feature at dozens of scales using the procedure described above. In this specific experiment, 6 iterations of 6 scales each were used, producing 36 total manufactured features per data point.

The processed data now consists of a single minimum feature size for each coordinate in the experiment designs. These data are separated back into training and test datasets, and the training data (which consists of independent parameter coordinates and dependent minimum feature sizes) is used to fit a polynomial function over the experiment space, producing a continuous design rule function for minimum feature thickness over all shape and orientation parameters.

The predictive quality of the design rule function is checked by comparing its predictions with the measured data in the test dataset.

By measuring minimum feature size at various overhang angles, it is expected that the maximum overhang angle design constraint will be automatically captured by correspondingly large minimum feature sizes for features with greater degrees of overhang; details of the actual behavior are presented in a subsequent section.

3.6 IMPLEMENTATION

The above approach was implemented on two example machines (one from the material extrusion and one from the vat photopolymerization AM process categories) as part of this study. Unlike with the powder bed fusion process studied previously in Weiss, et al. (2018), overhang is a significant concern in both these processes. For material extrusion processes utilizing a hot nozzle and common thermoplastic build materials, various authors suggest 45° as a maximum overhang angle ("Design Guide: ABS 3D Printing," n.d.; Johnson et al., 2011). For vat photopolymerization processes similar to the Form2 used in this study, researchers and the industrial company i.materialise encourage unsupported overhangs to be less than 60°-65° from vertical (Byun and Lee, 2006; "Design Guides: Gray Resin 3D Printing," n.d.; Lantada and Morgado, 2012).

In the considered material extrusion manufacturing process, melted polymer is extruded through a small nozzle and cooled quickly to solidify into the final part; for additional description, the reader is referred to the excellent video by Stratasys Direct Manufacturing ("3D Printing with FDM," n.d.). Failure sources observed in the course of this experiment for this process included drooping, where a lack of structure underneath the newly extruded material causes it to deform downward before solidification occurs. Small features can also fail because of mechanical limitations, if the material is unable to support its own weight through manufacturing in the presence of machine vibrations. Negative features fail because of over-extrusion of material in the

surrounding solid regions which causes blockage, especially near the start or the end of the feature, where extra-dense "floor" and "roof" structures appear.

In contrast, the vat photopolymerization process studied here directs a laser over a vat of liquid resin, initiating a photopolymerization reaction which solidifies a thin layer of material ("What is Stereolithography (SLA)?," n.d.). Failure sources observed in this experiment primarily consist of drooping and warping of positive features from fluid forces encountered during build plate motion and post-processing in alcohol. Mechanical failure can also break thin features unable to support their own weight. Negative features fail when resin is not completely cleaned from the channel during post-processing before post-curing, and can also suffer from over-curing of subsequent wall layers and scattering of the laser light in surrounding geometries (the specific post-processing procedures used are described shortly).

In addition, in either process, the manufacturer-supplied preparation software may choose to eliminate some small features as un-manufacturable, or instead instruct the machine to place a single line of solid material even though a thin feature is smaller than the line width of the deposition process, further adding to potential error sources. By assessing the entire process end-to-end, all sources of potential errors are accounted for, providing a "real-world" estimate of manufacturing success.

The experimental process described in the previous section was run on both of these processes. The experiment designs consisted of 55 training data points selected by Maximum Entropy Design using all three parameters as factors (r_l, r_w, and ϕ). An additional 21 data points were selected using a subsequent Maximum Entropy Design along the "Bar" face of the parameter cube, because of significant practical design interest in structures involving bars, for a total training dataset size of 76 coordinates. The test dataset consisted of 20 points selected using Latin Hypercube design, and for the positive features in the experiment run on the material extrusion AM platform, an additional 12 Latin Hypercube data points were used to provide validation for the bar "face" (6 points with $r_w = 1$) and the bridging "face" (6 points with $\phi = 90$). Also, as a

result of preliminary findings (described in the next section), additional MED data points were taken for the positive training data in the experiment run on the material extrusion AM platform, replicating all points otherwise lying on the $\phi = 90$ plane but at an angle of $\phi = 80$ (15 additional points). A summary of the sub-experiments performed on each process is shown in Table 3.2.

Table 3.2. Summary of experiments performed

			Material Extrusion		Vat Photo-polymierization		Comment
Experiment		Samples	Pos	Neg	Pos	Neg	
Training	3 Factor MED	55	●	●	●	●	
	"Bar" Supplementary MED ($r_w = 1$)	21	●	●	●	●	Built with data already present on the "Bar" plane as priors.
	"Non-Bridging" Alternate MED	15	●				Replaces all data points having $\phi = 90°$ with $\phi = 80°$
Test	3 Factor Latin Hypercube (LH)	20	●	●	●	●	
	"Bar" Supplementary LH ($r_w = 1$)	6	●				
	"Bridge" Supplementary LH ($\phi = 90°$)	6	●				

Each test artifact, sampling 5-7 oriented shapes, was generated and manufactured once per iteration; the experiment consisted of six total iterations. For the material extrusion process category, parts were manufactured on a FlashForge Finder, using white PLA filament as the feedstock with an extrusion temperature of 220°C and a layer height of 0.183 mm, with all support settings disabled. After manufacture, these parts were removed from the build plate and analyzed without any further post-processing.

A FormLabs Form2 AM machine represented the vat photopolymerization process category in this study. The feedstock FormLabs Gray resin (item GPGR03), with default settings and 0.05 mm thick layers, all support settings disabled. Post-processing of the vat photopolymerization

parts consisted of removal from the build plate, 15 minutes of cold ultrasonic washing in a bath of isopropyl alcohol, and at least 60 minutes of curing in a UV chamber.

When assessing the resulting parts, the primary criteria considered was the presence of stable features which accurately reflected the overall length and shape of the designed feature. Small amounts of warping and drooping were permitted so long as the mechanical integrity and general shape of the feature remained intact (in the vat photopolymerization experiment, extreme amounts of warping were permitted so long as the feature geometry remained present). Holes were required to be visibly clear. The assessment did not measure the geometric or dimensional accuracy of the produced features. Other studies have suggested that inaccuracies in these quantities are prevalent near the minimum feature size of AM processes due to compensations used in the preparation software, and mechanical accuracy of the AM platform (Meisel and Williams, 2015; Seepersad et al., 2012). Quantifying these deviations is beyond the scope of the present work.

After manufacturing, linear, quadratic, and cubic polynomial functions ($\hat{s}_1$, $\hat{s}_2$, and $\hat{s}_3$) were fit to the training data as candidate continuous design rule functions. The linear relationship can be stated as

$$\hat{s}_1(r_w, r_l, \phi) = a_1 r_w + a_2 r_l + a_3 \phi + a_4 \tag{3.1}$$

with r_w the thickness/width ratio, r_l the length/thickness ratio, and ϕ the angle between the feature axis and the build direction and $a_1, \dots, a_4$ fitting parameters to be determined using least squares regression. The second order and third order polynomials are,

$$\begin{aligned}\hat{s}_2(r_w, r_l, \phi) = {} & a_1 r_w^2 + a_2 r_l^2 + a_3 \phi^2 + a_4 r_w r_l \phi + a_5 r_w r_l + a_6 r_l \phi + a_7 r_w \phi \\ & + a_8 r_w + a_9 r_l + a_{10} \phi + a_{11}\end{aligned} \tag{3.2}$$

$$\begin{aligned}\hat{s}_3(r_w, r_l, \phi) = {} & a_1 r_w^3 + a_2 r_l^3 + a_3 \phi^3 + a_4 r_w^2 r_l + a_5 r_w r_l^2 + a_6 r_l^2 \phi + a_7 r_l \phi^2 \\ & + a_8 r_w^2 \phi + a_9 r_w \phi^2 + a_{10} r_w r_l \phi + a_{11} r_w^2 + a_{12} r_l^2 + a_{13} \phi^2 \\ & + a_{14} r_w r_l + a_{15} r_w \phi + a_{16} r_l \phi + a_{17} r_w + a_{18} r_l + a_{19} \phi + a_{20}\end{aligned} \tag{3.3}$$

Because polynomial regression attempts to minimize the overall error between the function and the input data points, the results sometimes include regions of the $\hat{s}$ function which are

significantly lower than any sampled data point, a case unlikely to occur in practice for sufficiently large samples. To remedy this, the polynomial fits are further adjusted to always be no smaller than the smallest data point sampled using the following transform:

$$\begin{aligned} &\tilde{s}_i(r_w, r_l, \phi) = \max(\hat{s}_i, t_{lower}) \\ &t_{lower} = \text{mean}(t_1, t_2, t_3) \\ &\text{with} \quad t_1 < t_2 < t_3 < \cdots < t_n \end{aligned} \tag{3.4}$$

where t_{lower} is a lower limit on the minimum feature thickness constructed by averaging the three smallest minimum thicknesses observed in the current sample. This "min clamping" helps ensure that predicted feature sizes are manufacturable by ensuring they are at least as large as some feature in the current data set which has been manufactured successfully.

3.7 Results and Analysis

As noted, the experiments described in previous sections were performed on an example process from both the material extrusion and vat photopolymerization AM process categories; a summary of the results is shown in Table 3.3. The minimum size for different feature shapes and orientations is seen to vary by as much as an order of magnitude in every case except negative features in the material extrusion example process, and even that case saw a 4x spread. Except for the positive vat photopolymerization dataset, 80-90% of the oriented shapes showed enough stochastic behavior to avoid perfect separation and create a reasonable logistic fit (recall that perfect separation means the all "fail" data points are less than or equal to all "pass" ones, meaning a logistic regression is not possible).

Table 3.3. Summary Results of the experiments

		Material Extrusion		Vat Photo-polymerization	
		Positive	**Negative**	**Positive**	**Negative**
Oriented Shapes Evaluated		123	96	96	96
Test artifacts		19	16	16	16
Iterations/artifact		6 (four: 17[a])		4	
Feature types with logistic fit		86 (90%)	87 (91%)	51 (53%)	81 (84%)
Min. Feature Size (Thickness) Estimates (mm)	**Smallest**	0.18[b]	0.307	0.1[b]	0.538
	Largest	1.583	1.249	1.08[c]	5.80
	Mean	0.596	0.773	0.235	1.89

[a] Explanation of these four is present in the subsequent text
[b] This was the smallest allowed element diameter in the respective trial
[c] Several outlier data points in the vat photopolymerization positive experiment have been identified and are discussed later in this section, but are still reported in these summary results

More detailed results are presented in the following three subsections for the material extrusion example process. First, the effectiveness of the iteration approach is evaluated as low-level building block for subsequent analyses. Next, just the cylindrical "bar" features with $r_w = 1$ are investigated, providing mid-level results which compare the expected and observed behavior in several areas, addressing Research Questions 1 and 3. Then, high-level results present the performance of a series of polynomial fits to the full sample space, providing design rule functions and answering Research Questions 1 and 2. Finally, a summary of the corresponding findings for vat photopolymerization example process are included at the end of this section.

A. Low-Level Results: Individual Feature Types

The validity of the resulting design rule function depends on the quality of the individual estimates of minimum feature size. These estimates depend on the number of iterations of the experiment performed, that is, how many copies of each feature at varying scales have been manufactured.

Most references surveyed in the Background section include 4-10 copies of individual pass/fail features in a particular orientation when comparing processes, and while several exhaustive studies include hundreds of individual features, they are organized into similar shapes manufactured at between 10 and 21 different sizes (Govett et al., 2012; Wegner and Witt, 2012). No surveyed work addresses the question of how many features should be included in such a study, and only Meisel and Williams (2015) gives attention to the stochastic behavior of the process near the minimum feature size limit.

To address this question, four of the test artifacts in the material extrusion process experiment, containing a total of 12 positive and 12 negative feature types, were allowed to iterate for an additional 11 iterations (for a total of 17). After each iteration, the minimum feature thickness, which value would be returned if the experiment was to be stopped at this point, is compared with the final design rule after all 17 iterations have completed. Significant variations in the design rule are seen in the first few iterations, as the pass/fail threshold is located and the range of feature scales focuses in on this transition. If the design rule determined after 17 iterations is taken to be fully converged, the variation and convergence behavior in the design rule value at prior iterations is visualized in Figure 3.9.

For both positive and negative features, after four iterations, only about half of the features are within 10% of the final value. After six iterations, all but two of the 12 feature types have converged to within 10%. This suggests that six iterations is the minimum required to provide reasonably accurate design rules for this process. Six iterations at six scales per iteration corresponds to 36 copies of each feature, significantly more than used by other researchers. Also, unlike existing studies, the iterative approach used here reduces the dependence of the minimum feature size on the accuracy of the guess used to set the initial range of feature scales, as successive iterations adapt to the results of previous ones.

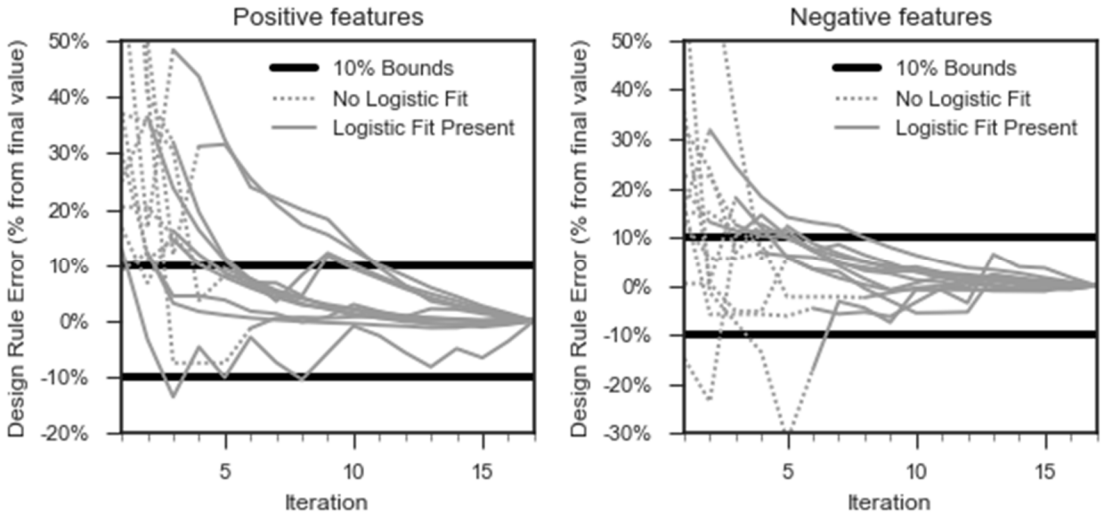

Figure 3.9. Value of the minimum feature thickness *t* for each iteration for 12 positive and 12 negative features, as a percentage of the final value (after 17th iteration).

Another significant advantage of the adaptive iteration approach is the ability to "zero in" on the relevant range of feature scales. Manufactured test features are only useful if they lie near the minimum feature size; features which are clearly doomed to failure or certain to succeed are unlikely to provide useful information. For example, the initial range of thicknesses specified for positive features on the material extrusion example AM platform was 0.4 mm to 1.0 mm, however several oriented shapes attained minimum feature thicknesses significantly less than this, as low as 0.18 (the lowest value allowed). If only the six scales of the feature had been used to estimate minimum feature size, all features would have been manufactured successfully and only an upper bound on the minimum feature size could be suggested.

Stochastic variation in the processes was also seen across all the oriented shapes in the dataset from the material extrusion example process. As the iterations progress, the heuristic algorithm zooms in on the pass/fail transition, and at some scale the stochasticity of the process begins to be seen in variations in results between features of similar scale or between manufacturing runs. Once this variation is present, logistic regression is used to map a probability function to the data. The 5%-95% probability spread covers an average range of thicknesses of 0.222 mm. In addition, the difference between the thickness of the smallest passing feature and

the largest not-passing feature across the positive material extrusion dataset is 0.109 mm. In order to adjust for this stochasticity, the minimum feature size reported corresponds to a 95% pass probability, which for the positive material extrusion data represents an average increase of 0.149 mm over the smallest successfully manufactured feature, but only a 0.040 mm increase over the largest failed feature. These results represent a significant fraction of the mean minimum feature size over the dataset, suggesting that using a single series of features on one manufacturing run to assess minimum manufacturable feature size is not a reliable way to produce robust design rules.

Another assumption in the approach taken here is the suitability of logistic regression as a tool for modeling the underlying success probability function. The statistics literature suggests a minimum sample size of 50 data points is required to employ logistic regression with confidence (Sheskin, 2011). For the 24 features on the artifacts allowed to iterate 17 times, a total of 96 data points are present, and the binned data visually match the progression of a logistic curve; for example see Figure 3.10.

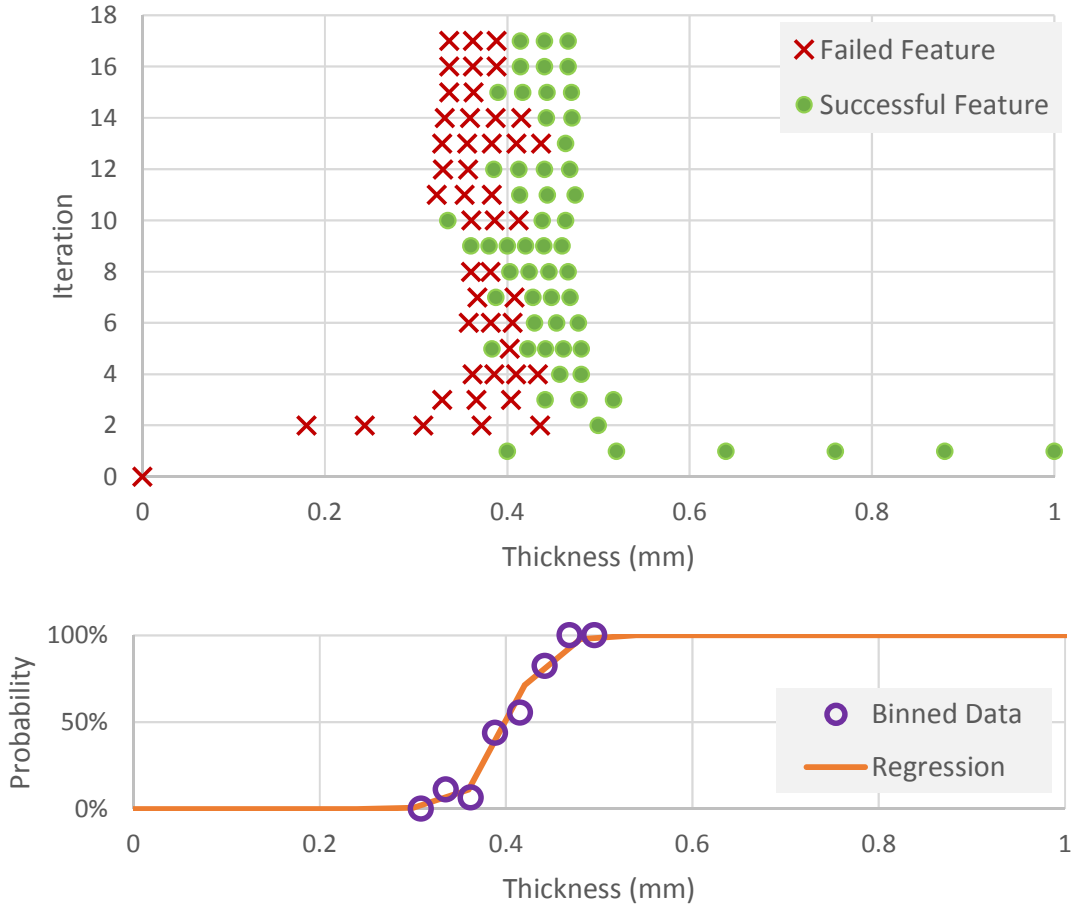

Figure 3.10. The scored features by iteration, and grouped by bin above the corresponding logistic regression curve for a single feature type.

For the remainder of the data, after six iterations only 36 data points are collected, which is too few to confidently apply logistic regression techniques, making the results not yet statistically significant. As a result, controls in the iteration process are applied to keep incorrect or unreasonable logistic fits from being utilized. Logistic regressions are rejected if the P value is greater than 0.5 (i.e. the fit is less than 50% probable), or if the spread of the probability distribution is more than twice the spread of the data collected so far. In these cases the heuristic approach is used instead.

Based on the above, for this material extrusion process, six iterations (corresponding to 36 data points per feature type), is the minimum appropriate amount of data to collect, and for

stronger statistical confidence in the result, eight or more iterations are suggested, resulting in 48+ data points, enough to satisfy the best practices of the literature.

B. Mid-Level Results: Cylindrical "Bar" Features

In this section, the data set is restricted to features with width equal to thickness ($r_w = 1$; cylindrical features). For this subsection, the main experiment data with $r_w = 1$ is supplemented with 21 additional MED data points (the "Bar supplementary" data set) included in the study but consisting only of cylindrical features of various lengths and orientations. The additional MED data was selected with the main experiment data specified as prior information, making the resulting combined dataset have good coverage over the space while reusing as much of the experimental results as possible. The minimum feature size, expressed as the diameter of the cylinder, is the dependent variable at each assessed oriented shape in this analysis. Results, shown with interpolating surfaces for ease of visualization, are presented in Figure 3.11.

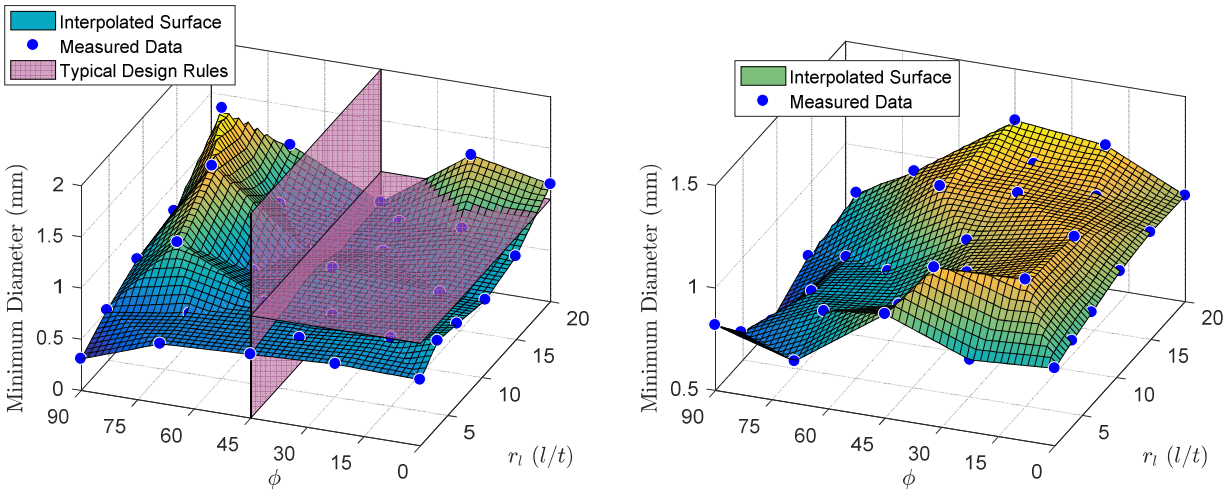

(a) (b)

Figure 3.11. Interpolated visualization of the cylinder data, parameterized by the length/diameter ratio r_l and the overhang angle ϕ. Design rules from industry best practices are shown as translucent planes. (a) Positive features (b) Negative features.

Comparison with existing design rules

This easier-to-visualize subset of the data is used to correlate the results obtained with expectations based on the process physics. In addition, the data will be compared with the

literature-accepted overhang angle of 45° for similar hot-nozzle material extrusion processes utilizing common plastic feedstocks ("Design Guide: ABS 3D Printing," n.d.; Johnson et al., 2011) and 60-65° for similar vat photopolymerization processes utilizing UV curing of photopolymerizing resins (Byun and Lee, 2006; "Design Guides: Gray Resin 3D Printing," n.d.; Lantada and Morgado, 2012). The minimum feature size for cylindrical features obtained from the NIST test artifact (Moylan et al., 2014), which was manufactured on each of the processes in question, is also compared to the results obtained using the present method.

For the material extrusion process studied, as hypothesized, high angles of overhang receive comparatively larger minimum feature sizes for long bars, where r_l is large, caused by drooping. Long, nearly-vertical cylinders also see a large minimum feature diameter, resulting from comparatively small in-plane cross-sectional area and loads from the motion of the print head increasing the risk of failure from mechanical stress. Long features near 45° have more cross-sectional area in each plane and can therefore be manufactured more reliably at smaller diameters. The bridging effect allows very slender cylinders in the horizontal direction, so long as both ends are supported. Short features (with $r_l < 5$) show relatively little dependence on angle, so long as the parent body remains below/beside the small feature so some source of support is present.

Holes in the material extrusion process studied (Figure 3.11b) perform best in the horizontal configuration, where very small holes are easy to create by not depositing material for one or two layers. Vertical holes can be smaller in diameter than angled holes because the clean alignment between layers reduces the likelihood the hole will be fully blocked by over-extrusion. Since the failure modes for holes are generally not dependent on depth, little variation is seen in the r_l direction.

Figure 3.11a presents the industrially-generated design rules from i.materialse ("Design Guide: ABS 3D Printing," n.d.), which specifies a 1.0 mm wall thickness and 45° maximum overhang angle as shaded planes. It is evident that the existing suggestions work reasonably well

for the bulk of positive design cases. The typical overhang angle for positive features in this process (visualized with the vertical plane in Figure 3.11a) avoids the regions of drooping, which correspond to the higher minimum feature sizes. However, this strict maximum overhang angle excludes the possibility of including smaller features at any angle, so long as the lower edge of the feature remains supported. In fact, the strict maximum overhang angle criteria excludes approximately 43 % of the design space studied for which the minimum feature size is less than 1 mm. No industrial guidelines were identified which provide general design guideline for the minimum hole diameter in the material extrusion process studied.

Depending on the method used to select a minimum feature size design rule, different problems arise. A conservative estimate for the positive features of the material extrusion process studied would place the minimum feature size at the worst-case value, which in the present study was 1.25 mm (excluding features below the overhang angle). With this estimate, all features above the overhang cutoff should be manufacturable, but a significant portion of the design space is restricted (i.e. features much smaller than the design rule are producible in shorter lengths). In addition, it requires a fairly thorough survey of the space to accurately locate the feature type which sets this conservative design rule, so generally a few sample points and a generous safety factor is used instead. On average, a conservative design rule of 1.25 mm diameter over-estimates the true minimum by 0.49 mm on average over the interpolated design space of cylinders with $\phi < 45°$.

In existing literature, a design rule is typically selected based on a single sample, generally placed at $\phi = 0°$ and $1 \leq r_l \leq 10$. The NIST part includes a series of five cylinders, all 2mm tall, with diameters [0.25, 0.5, 1.0, 1.5, 2.0] mm. These points are visualized in Figure 3.12. Based on the current experiment, a design rule based on the smallest manufactured feature size is accurate for most positive features below the overhang angle cutoff. However, for long features, especially not quite vertical, the actual minimum feature size is underestimated by as much as 0.25 mm (25%), and a designer utilizing this optimistic design rule will very likely obtain an unsatisfactory

product. For negative features (Figure 3.12b), the NIST artifact's results are also optimistic, as the variation in minimum hole diameter with hole angle is significant over much of the domain.

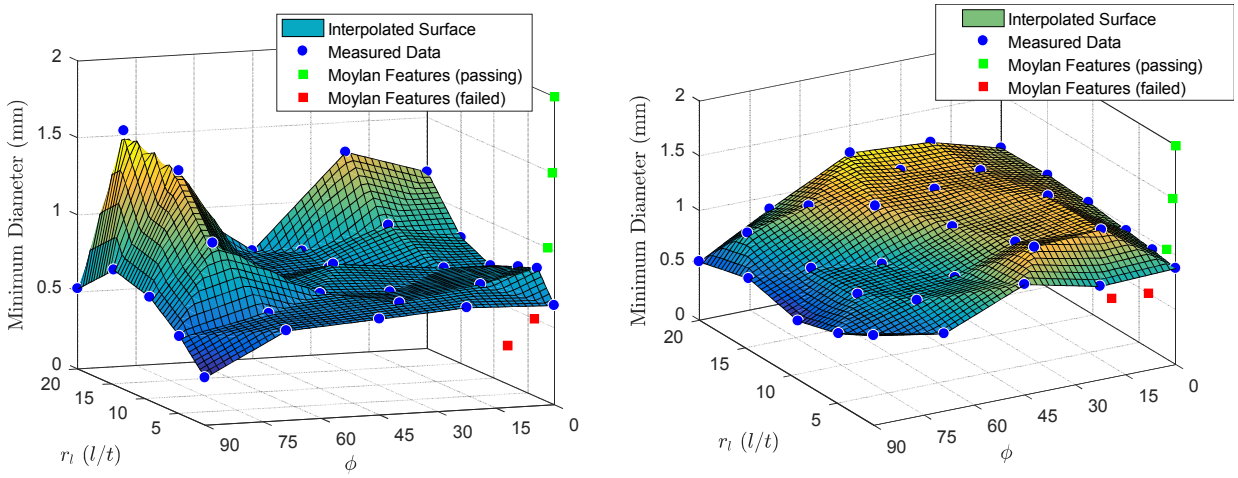

Figure 3.12. The interpolated sampled data, with the data points from the NIST test artifact (Moylan et al., 2014) overlaid on the $\phi = 0$ plane. (a) Positive features (b) Negative features.

Design rules from polynomial fits of the data

Above, qualitative and quantitative assessment of the cylinder dataset was performed based on the raw data and a 2D linear interpolating surface. In support of Research Question 1, this section explores fitting a low-order polynomial function to the data to create a design rule function which is predictive for intermediate coordinates not directly sampled. To evaluate the predictions for the positive material extrusion data, a six data point Latin Hypercube sample is used for testing ("Bar supplementary" LH data). Because the "bridging" features behave very differently, they are excluded from the data set for this sub-subsection and treated differently in the *High Level Results* subsection to follow.

Because the experiment was constructed using an MED method, ordered subsets of the results can be used to define sub-experiments containing fewer data points. Polynomial fits were applied using just two variables (i.e. Equations (3.1), (3.2), and (3.3), with $r_w = 1$, using the modification in (3.4)) for various sizes of experiment, and the errors are plotted in Figure 3.13. Figure 3.13a shows error with respect to the corresponding six test data points (from the Latin

Hypercube validation data), while Figure 3.13b shows the RMS error of the fit against the entire cylinder MED dataset.

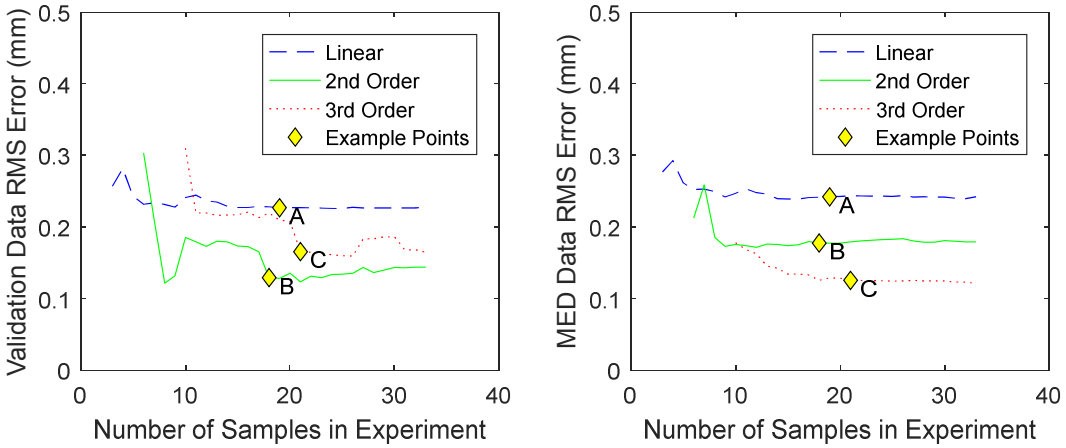

Figure 3.13. Variations in the fit quality obtained as the experiment size changes, for the "bar" dataset of positive features in the material extrusion process. (a) shows RMS error against the 6 test data points, and (b) shows RMS error against the entire cylinder MED datasets. "Example Points" will be visualized in Figure 3.14.

For both error metrics, the nonlinear shape of the underlying data results in poor fitting with the linear (first-order) polynomial function. Second order regression fits the test data nicely, but does not perform as well at fitting the larger MED data set as the 3rd order function. The 3rd order polynomial fit appears to be over-fitting the training data; however, so few test data points are present for validation that it is difficult to draw conclusions.

Qualitatively, the higher-order fits do a much better job of following the trends in the collected MED data, and three representative fits are visualized in Figure 3.14. The linear fit (Figure 3.14a) only captures the general trend in the data, and cannot fit the large valley in the middle of the ϕ span. A quadratic fit does better, but higher-frequency features in the data are not well modeled (see arrows in Figure 3.14b). As a comparison, consider the linear model using the smallest amount of data possible (3 data points, or the end of the "Linear" curve in Figure 3.13a closest to the Y axis). The quadratic fit achieves a 53% reduction in error against the validation dataset compared with the this "simplest" reference model. Figure 3.14c presents a cubic

interpolation of the first 21 samples. Fits utilizing more data than this achieve only minor improvements in either error metric.

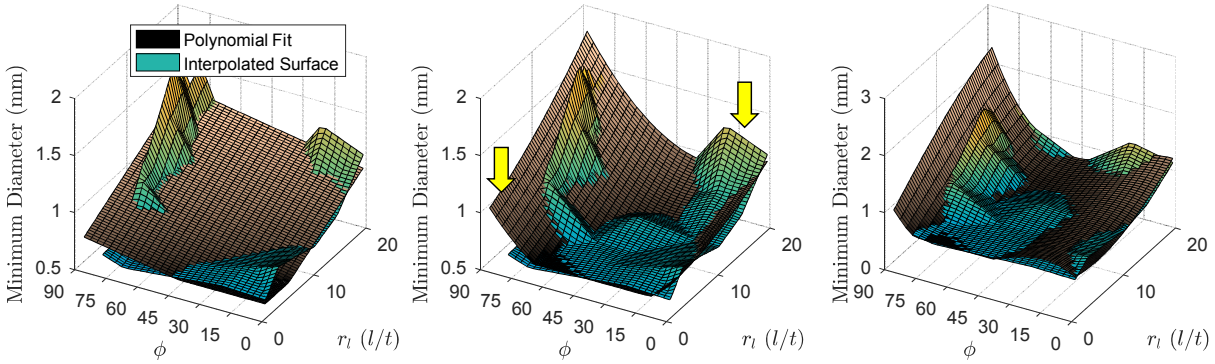

(A) Linear, 19 samples (B) Quadratic, 18 samples (C) Cubic, 21 samples

Figure 3.14. A polynomial fit (in brown) overlaid on the linear interpolation of the raw data for three different fit functions, each with around 20 samples of data used. Labels correspond to the "Example Points" in Figure 3.13.

In general, the design rules presented here, approximated as polynomial surfaces in the design space, have the potential to incorporate more robust and effective constraints on manufacturable features, resulting in improved utilization of the design space. The results suggest that in answer to Research Question 3, a variable minimum feature size constraint can incorporate the intent of the maximum overhang constraint used elsewhere by requiring much larger minimum feature sizes in regions with significant overhang, but still allow short features to be produced at all angles without hindrance. The incorporation of statistical modeling of the failure of produced features causes the produced design rules to be more robust in the face of process and parameter variability.

C. High-Level Results: Cylindrical and Plate Features

In this subsection, the full dataset of cylindrical and plate features is combined to produce a single design rule function valid over the entire domain. The key questions addressed in this section are Research Questions 1 and 2, investigating whether such a design rule is predictive, and how much data is required to make it effective.

As discussed in the Background section, the literature approaches the problem of assessing feature size for various feature shapes either by assigning a single minimum feature size constraint to the entire design space (often based on the result of experimental assessment of only one or two features), or by systematically surveying a huge number of features to produce design rule tables relating two parameters at a time (such as hole diameter and depth). The approach presented here attempts to fit an analytic function to a carefully selected subset of feature types, rather than collect the extensive amount of data other researchers do in their full-factorial experiments (Seepersad et al., 2012; Wegner and Witt, 2012). As a result, the approach presented here represents a middle of the road approach which is more generally applicable (effective across three parameters at once) while requiring an achievable number of features to be manufactured and evaluated.

The data considered for this section consists of the main MED training set, not including the supplementary MED data used in the previous section to keep the data evenly distributed across the parameter space. However, because the second support in horizontal features ($\phi = 90°$) significantly changes the behavior in the bar data presented above, the positive material extrusion feature space is divided into two sections for this analysis, as shown in Figure 3.15a, and bridge features are handled separately. Negative features for the material extrusion experiment have no special characteristics for horizontal features, and the design rule function fit is compiled using all the MED data.

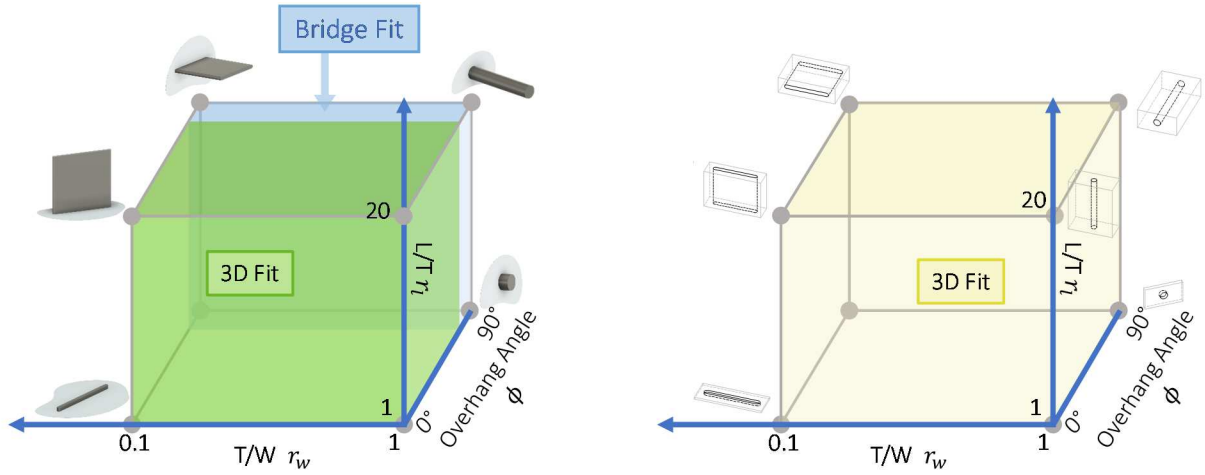

(a) (b)

Figure 3.15. Subdivision of the parameter space for the high-level analysis. The space of positive features for the material extrusion experiment is shown in (a), divided into "Bridge" horizontal feature fits and the remaining data ("3D fit"). (b) shows the parameter space for negative features of the same experiment, which is all fit with a single function.

3D Design Rules for the Material Extrusion Results

Since the training data was constructed using a maximum entropy experiment design, the first N points in the experiment can be separately considered as a valid experiment as well. This characteristic is exploited to allow the number of data points considered when selecting the fit to vary from one to the entire MED dataset (55 total). Because 14 of these data points lie on the $\phi = 90°$ face of the parameter space, and are therefore treated separately in the next sub-subsection, the data were re-taken at the same coordinates except for $\phi = 80°$. This ensures that the coverage over the entire parameter space remains relatively even, though an entirely new DOE would yield more accurate results (these come from the "Non-Bridging" Alternate MED dataset shown in Table 3.2).

Each subset of the data is fit using three polynomial functions (described in the Implementation section as Equations (3.1), (3.2), and (3.3), using the modification in (3.4)). The quality of each fit is evaluated by considering the root-mean-square error of the predictions compared with the measured values over the separate test dataset. This RMS error is plotted for each fit type in each set of experiments in Figure 3.16.

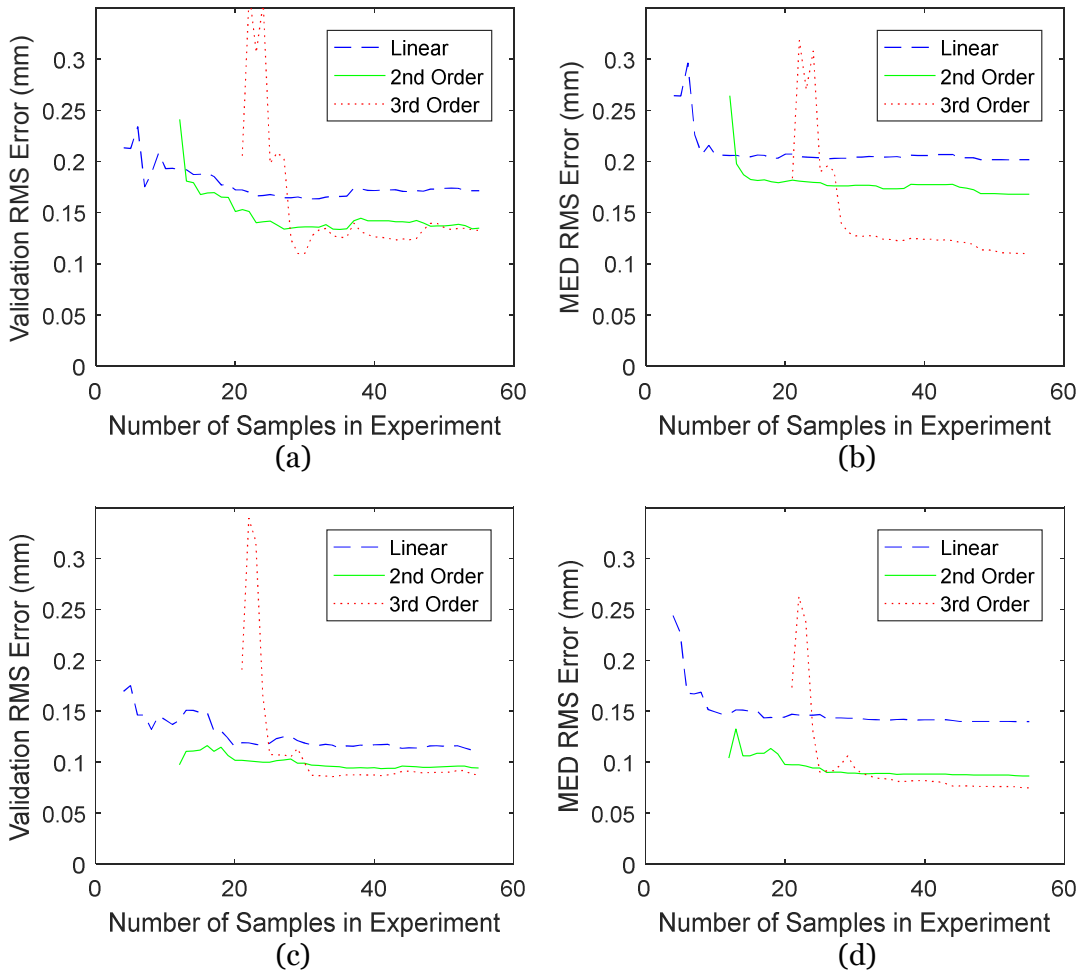

Figure 3.16. RMS error with respect to the test dataset for fits of different order polynomials considering different amounts of the input data for the material extrusion example process. (a), (b) show results for positive features when compared with the validation and MED data sets, and (c) and (d) present the same for negative features.

For positive features from the material extrusion example process, the fits presented show errors on the order of 0.1-0.15 mm, or about 15-25% of the mean minimum feature size of 0.610 mm. Errors computed against the validation (test) dataset and against the entire MED dataset indicate that a 2nd order fit out-performs a first order (linear) one, but while a 3rd order fit with more than 30 samples improves substantially in predicting the MED data itself, it provides little improvement on the validation data. This suggests that the 3rd order polynomial is over-fitting the sampled values and not tracking real trends in the data. For all fits, performance against the validation data improves with increasing number of samples in the experiment, up to around 30.

Negative features on the material extrusion example process perform significantly better, with predictive errors on the order of 0.1 mm (15% of the average negative feature diameter of 0.699 mm) and small improvements in fit quality are seen up to around 30 samples. For negative features, the 2nd and 3rd order polynomials achieve very similar error rates using both metrics, suggesting that the higher-order fit does not expose any new dynamics in the data.

Note that in each case, the collection of additional data and the use of a higher-order fitting function has a significant effect on the quality of the resulting design rule. The difference between the first linear design rule, using four points in each case, and the best-performing design rule in both validation error metrics above, is almost a 50% reduction (49.4% reduction for negative features and 48.5% reduction for positive).

Bridge Design Rules for Positive Features in the Material Extrusion Example Process

An analysis similar to that used for the cylindrical "bar" dataset was performed on the set of MED points from the original experiment which formed "bridges" supported at both ends due to $\phi = 90°$. The minimum feature size data is presented with an interpolating surface shown for clarity in Figure 3.17. Note that the axes have changed to r_w and r_l since for this slice of the parameter space, ϕ is fixed.

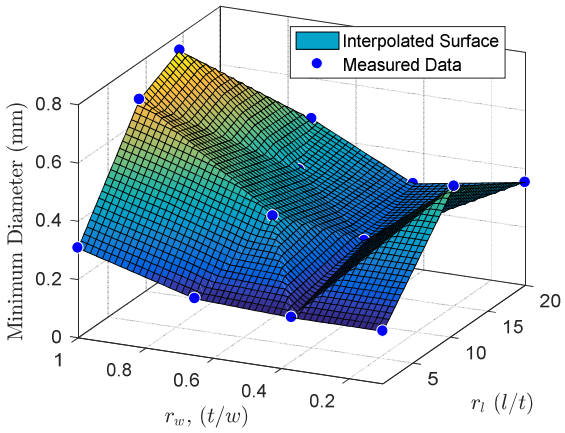

Figure 3.17. Minimum feature size data collected for bridging features.

From the "Bridge" Supplementary Latin Hypercube dataset (Table 3.2), six test data points are available for evaluating the quality of fits for the bridging features. As before, various polynomial fits are performed for increasing numbers of samples over the MED data, with errors computed both against the test data and against the full set of MED measured feature sizes, see Figure 3.18. Although the second and third order polynomial fits perform much better at fitting the original data due to the saddle shape of the raw data, the linear fit better matches the test data, suggesting that the shape seen in the MED data may be more indicative of a general trend than higher-frequency dynamics.

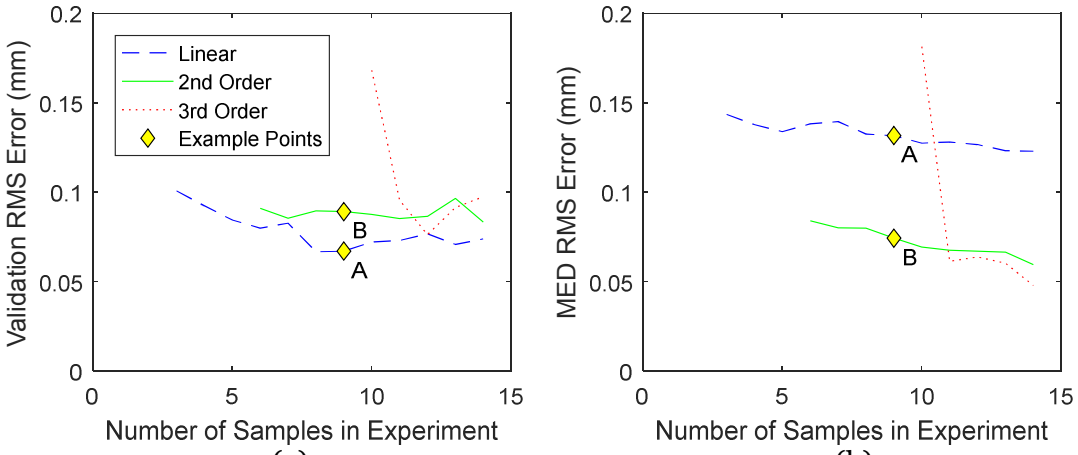

Figure 3.18. Performance of fit polynomials for the bridging data for varying number of fits and degree of polynomial. (a) shows RMS error against the validation dataset, while (b) shows fitting error against the set of all bridging MED data points.

Visualizations of the fits identified by "A" and "B" in Figure 3.18 are shown in Figure 3.19. Note that the quadratic fit captures higher-frequency dynamics in the data, but performs more poorly when evaluated using the test dataset (that is, example point "B" has a higher validation RMS error than example point "A" in Figure 3.18).

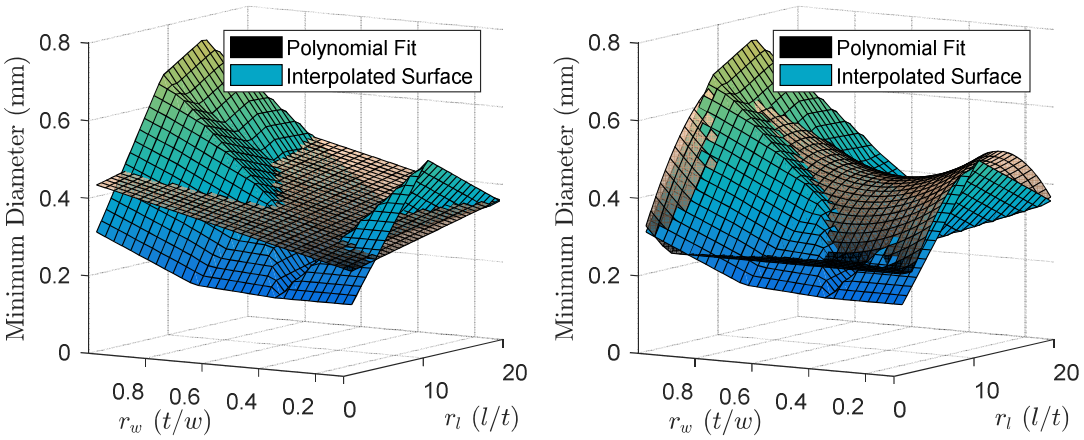

(A) Linear fit, 9 samples (B) Quadratic fit, 9 samples

Figure 3.19. Visualization of the two fits identified with diamonds in Figure 3.18.

Summary of Material Extrusion Results

In light of the above results, the following conclusions can be drawn:

- Polynomial design rule functions can be of significant value as design rules when all three parameters are considered, answering Research Question 1.
- The amount of data collected directly impacts the quality of the resulting design rule functions (Research Question 2)
- The polynomial design rule functions improve significantly on a fixed minimum feature size constraint.

By dividing the positive dataset for the material extrusion example process into "bridging" and "non-bridging" features, RMS accuracies of less than 0.110 mm and 0.067 mm against the test data, respectively, can be attained in each case. This represents 18% and 17% of the corresponding mean maximum diameter for each of the bridging and non-bridging feature types, respectively. Even better accuracies should be attainable if an overhang angle cutoff is used to remove the more variable data above about 50°. For the negative features in the material extrusion example process, no division of the parameter space is needed, and high-quality fits are obtained using 2nd-order polynomials.

With regard to Research Question 2, the amount of data collected directly impacts the quality of the resulting design rule functions. The above analysis suggests that up to a certain point, more data significantly improves the quality of the resulting design rule function (around 30 data points for the 3D fit and 8 for the bridge data). The additional data allows higher-order

models to be fit, reducing error, and also smooths out variation due to noise in the minimum feature size data collected.

The polynomial design rule functions improve significantly on a fixed minimum feature size constraint in increasing the space of available complexity. A polynomial design rule for the 3D dataset[5] provides an average minimum thickness estimate of 0.481 mm over the whole parameter space with overhang angles less than 45°, which is 0.519 mm less than a 1.0 mm design rule, a 52% reduction in the minimum feature size and a substantial increase in the space of designable features. The 1.0mm design rule is derived from industry recommendation for minimum wall thickness from i.materialse ("Design Guide: ABS 3D Printing," n.d.).

D. Vat Photopolymerization Results

The same experiment was performed on the FormLabs Form2, which is a vat photopolymerization process, and the results are described briefly in this subsection.

Positive Vat Photopolymerization Features

In the vat photopolymerization experiment, a significant amount of warping was seen in the positive features, apparently caused by the ultrasonic cleaning used for post-processing. So long as the shape of the original feature, though deformed, was still intact, the feature was classified as successful. However, as iterations progressed, the vast majority of features were successful by this metric, resulting in design rules which were mostly very near the minimum allowed thickness of 0.1 mm. Figure 3.20a presents the distribution of the measured minimum feature thickness, while Figure 3.20b shows a typical iteration history for a positive feature in the vat photopolymerization process used (compare to that for positive features in the material extrusion example process shown in Figure 3.10, which had a good overlapping mix of passing and failed features). Note that

[5] Specifically, these statistics were computed with a 3rd order polynomial fit to the full space using 20 samples of the experiment

the way the heuristic updating is unable to locate a definite transition between successful and failing features and zooms closer and closer to the minimum allowed value as iterations progress in Figure 3.20. In total, only about half of the feature types assessed could be fit with a logistic probability curve (see Table 3.3).

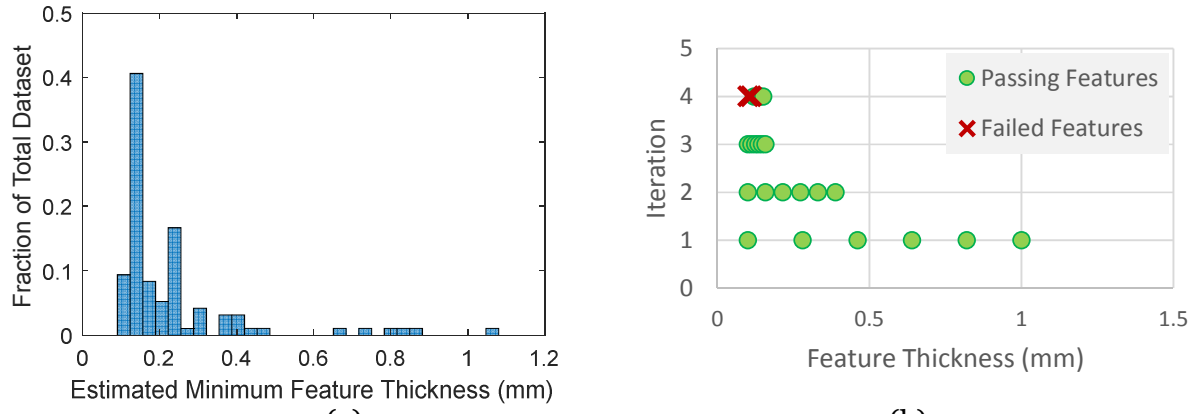

(a) (b)

Figure 3.20. (a) Histogram of minimum feature thicknesses computed for positive features in the vat photopolymerization process used. (b) Iteration history for a typical feature in the positive dataset for the vat photopolymerization process used.

On the other hand, the dataset contains six outliers, with minimum feature sizes significantly above 0.5 mm. Each of these was investigated, and in each case, 3-5 scaled oriented features failed, seemingly at random, throughout the iterations. The outlier features were all located on the far edge of their respective test artifacts, and therefore more likely to be bumped or broken during post-processing. This could be easily avoided in the future by adding protective structures to the artifact body.

More than half of the sampled points having minimum thicknesses below 0.15 mm, and seem to only reflect the raw laser spot size rather than a discernable design rule. Six outlier points have minimum feature thicknesses more than 0.6 mm, and are likely caused by experimental error. Between these two factors, meaningful design rules for features of reasonable size were not obtained from the vat photopolymerization experiment. In addition, while reasonable agreement between the training and test datasets present in the experiment was achievable, the design rules have failed to be predictive for several “real-world” example parts, severely under-predicting the

minimum manufacturable feature size. For completeness, results of the design rules obtained using the data collected for positive features in the vat photopolymerization process used can be found in Appendix C.

To correct these shortcomings, a revised experiment is proposed. First, the definition for "successful" must allow only minimal warping of the feature. Because in many applications small features are connected to the part body on both ends (as in lattice structures), part or all of the experiment should include supports on both ends of the feature under test, which will significantly reduce the likeliness of warping during post-processing. Finally, because this type of vat photopolymerization is capable of manufacturing small features at high aspect ratios, an alternative experiment in which the space of features is parameterized using length, width, and overhang angle instead of ratios of length/thickness and width/thickness will allow the experiment to estimate design rules for a user-specified space of "useful" feature sizes instead of trending towards the sub-millimeter-scale as this experiment did.

Negative Vat Photopolymerization Features

The negative component of the vat photopolymerization experiment was hindered by the features becoming too large. The ultrasonic post-processing step selected did not do a good job of removing bubbles of resin left in long tubes, resulting in many holes and slots otherwise perfectly fabricated by the Form2 machine being occluded by small amounts of resin which was then solidified in the UV post-curing chamber. As the iterations progressed, the features became so large that the test artifacts no longer fit on the build platform, and had to be controlled by an upper limit on feature width. An example iteration history, along with the corresponding logistic fit, is shown in Figure 3.21.

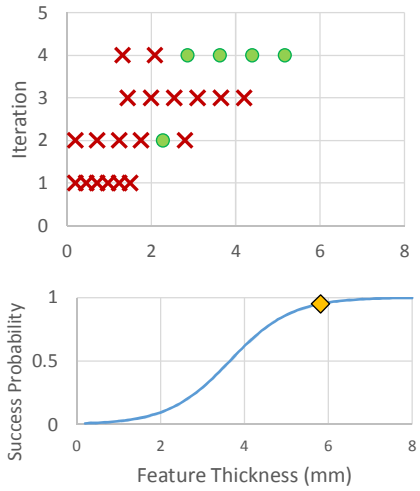

Figure 3.21. An example iteration history from a typical negative feature in the evaluated vat photopolymerization process with corresponding logistic fit.

Besides being significantly larger than features most designers are likely to use, the resulting data is reasonable and follows expected trends for the circular hole data: As r_l increases, features become progressively larger (see Figure 3.22). Significant noise in the measured data makes drawing conclusions after only four iterations premature; for example it is difficult to tell if the two largest feature sizes in the plot represent a trend in the data or just sampling noise. Time and resource constraints prohibited a prolonged experiment to evaluate how many iterations of this experiment should be run.

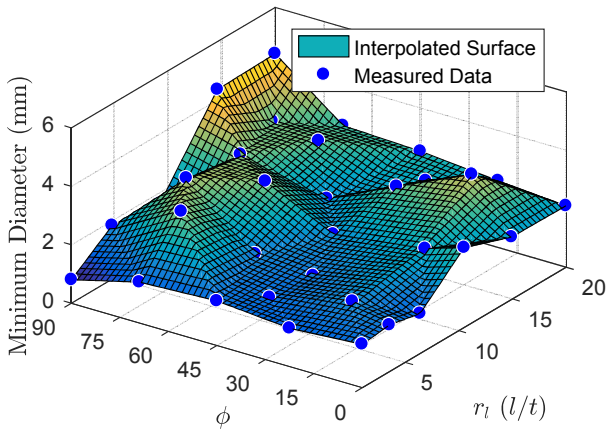

Figure 3.22. Circular hole data for negative features in the vat photopolymerization process, shown with an interpolating surface for clarity.

The remainder of the analysis of negative features for the vat photopolymerization process studied is reserved for Appendix C.

Again, some changes to the experiment would increase the likelihood of a more useful and robust design rule result. Modifying the experimental procedure to include manually clearing negative features using a jet of IPA before post-curing would significantly shrink the manufacturable feature sizes. Also, switching to a non-ratiometric parameterization for the feature space (as above, where width and length are used instead of r_l and r_w) would restrict the space of features evaluated to those useful to the designer.

With appropriate modifications, as described above, the overall process can be adapted to the vat photopolymerization AM process category and should provide useful design rule functions in a manner similar to the results shown for the material extrusion example process.

3.8 Application Examples

The parameterized design rule functions presented here are useful both to designers in specifying the geometry of new designs, as well as for manufacturing engineers evaluating the producibility of a design on one or more processes. The procedures described enable the user to take more complete advantage of the space of manufacturable features. In addition, the design rules are expressed as a function which is differentiable and easy to incorporate into layout, sizing, or topology optimization problems. In this section, two examples demonstrate applications of this approach.

For these examples, design rules built for the example material extrusion process are utilized. Where horizontal “bridging” features appear, the first-order fit to the bridging data with 8 data points is utilized. For non-bridging “bar” features, the 3rd order fit from the bar design rule based on 20 sample points acts as the design rule. For all remaining features, a 3rd order fit over the full 3D space is used, built on 28 sample points.

A. Model Sizing Example

In the first example, a pre-existing model of the Seattle Space Needle is evaluated to determine the smallest scale at which the model can be manufactured without losing fine detail (Jeepguy42, 2015). The design has a total height of 634 STL units, which are taken to be millimeters. The fine features in the model have been manually measured, and their coordinates in the 3D parameter space computed. See Figure 3.23 for several examples. In total, 12 unique shapes of small features were identified in the model. For each feature type, the appropriate design rule function is used to determine the minimum thickness of that feature. The minimum scale at which the model can be manufactured to preserve this feature is defined as the ratio between the minimum manufacturable thickness and the current model thickness (or diameter for cylindrical structures).

In order to map the features in the model to the features in the parameter space, several assumptions were made, illustrated by the inset panels in Figure 3.23. First, curved or multi-part features were taken as one or more linear segments, as in panel (a). Vertical plate features in panel (a) were modeled as bar features along the lower edge, a conservative estimate that ensures the remainder of the feature is manufacturable, or deemed out of experiment scope entirely because no allowance for rotation about the feature axis is included in the experiment. Note that these features should not be interpreted as plates with $\phi = 0°$, because they are not supported on the bottom face. Panel (b) includes three very thin features with aspect ratios of 25:1; these are assessed using the length/diameter ratio of 20 as a nearest estimate. The inclined overhanging feature in panel (c) does not correspond to a valid parametric feature, and support should be used in this case, as with the other locations in which unsupported horizontal features are present.

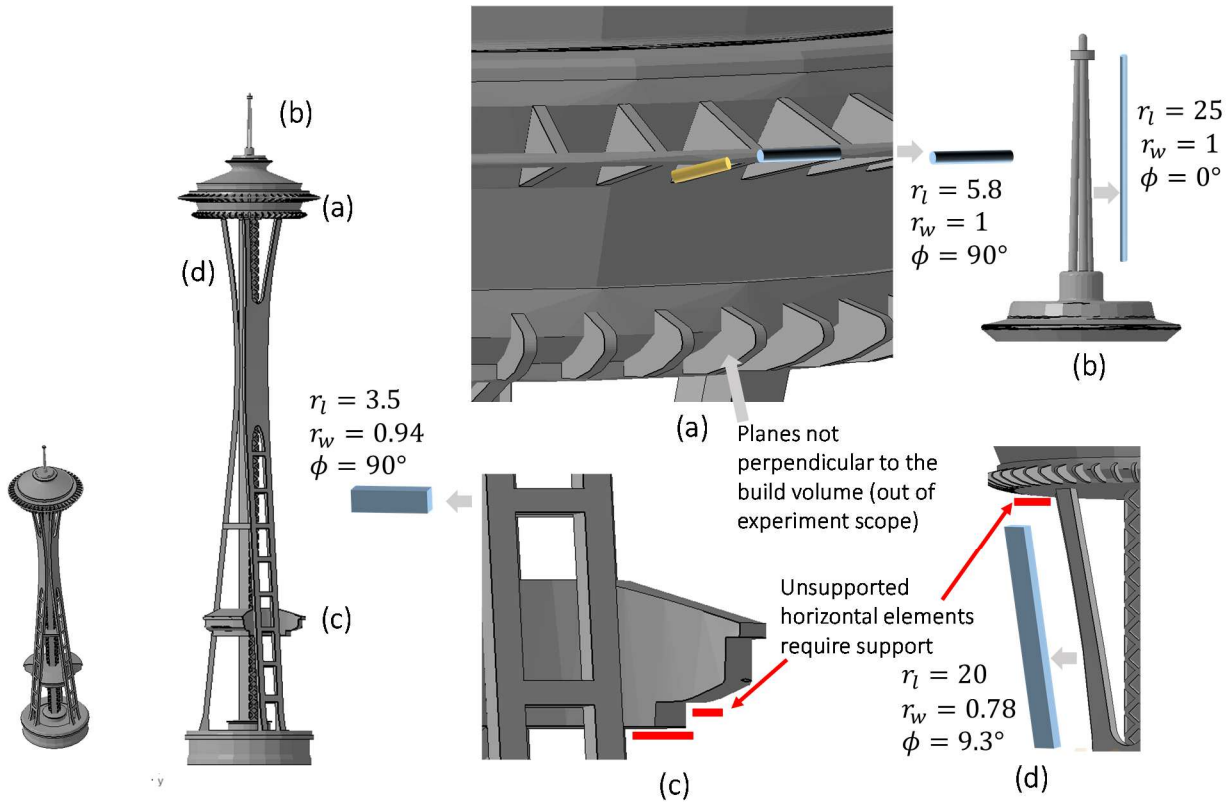

Figure 3.23. CAD model of an artist's interpretation of the Space Needle, with insets highlighting various features (see text for description). Model courtesy of Thingiverse user Jeepguy42 (2015).

In fabricating the Space Needle model on material extrusion example process, the overhanging features which are not bridging two bodies must be supported. In addition, the equivalent features for the supporting struts for the ring would require the entire model to be much larger than desired, so these struts are supported. In designing the support structures, the design rule function is again used to make sure that the support structures can be manufactured. Finally, because of the very large overhang just below the top of the model, the Space Needle design is cut in two pieces where the top connects to the supporting body, eliminating very long support structures.

As a result of the analysis, the smallest scale the Space Needle model can be manufactured at has a total height of 389 mm (61.4% of the original 634 mm) in this material extrusion process. The scale-limiting feature is the set of three thin antennas on the top of the model, once the

overhanging thin fins are supported. The design rule function predicts that the thin ring feature could be manufactured as small as 38% scale, despite appearing to be the most delicate feature in the model. The fabricated top piece is shown Figure 3.24a.

The above discussion limits the scale of the entire model. As a further example of the sizing analysis, consider for a moment only the bottom portion of the Space Needle model. The bottom half of the model contains larger features, and applying the same assessment to its features using the appropriate design rules results in a minimum scale of 21.3% (total height of 135 mm). The bottom half was separately manufactured at this scale, and is shown in Figure 3.24b. Of course, if the top half were manufactured at this scale the antenna, ring and support features all fall below the design rule guidelines, and manufacturing fails (see Figure 3.24c). As a result, for all features in the model to be fully resolved, the larger minimum scale dictated by the top portion of the model should be used.

On the other hand, consider if the design rules derived from the NIST test artifact were used instead (i.e. the smallest manufactured bar was 1.0 mm and smallest manufactured fin was 0.5 mm). In this case, the predicted scale for the top portion of the model would be 100% (634 mm tall), which while manufacturable is significantly larger than necessary. The bottom portion is predicted by the NIST design rule to be manufacturable at 12.7%, significantly *less* than the scale predicted by the approach presented here (which requires at least 21.3% scale). The part would likely have been manufactured at this smaller scale, only to have it fail and require trial-and-error additional iterations of guessing the scale and manufacturing, wasting time and resources.

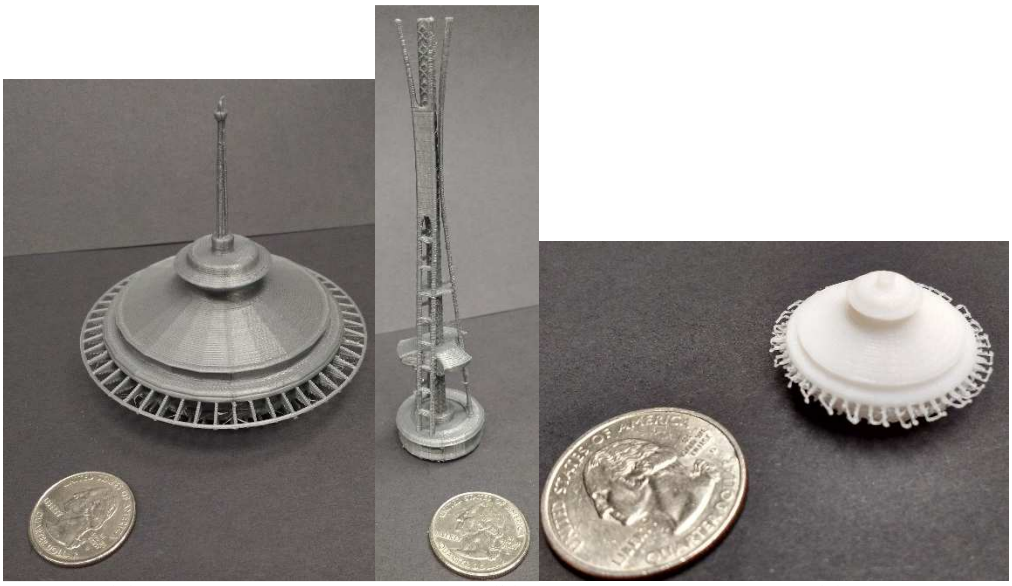

(a) (b) (c)

Figure 3.24 Manufactured Space Needle Model (3D model courtesy of Thingiverse user Jeepguy42, 2015). (a) Top part at minimum predicted scale. (b) Bottom part at its minimum predicted scale. (c) Top part manufactured at the bottom part's minimum predicted scale (NOT predicted to succeed).

B. Mesh Cell Miniaturization Example

The design rule functions developed in this work are also useful in design problems. As an example, consider the tetrahedral lattice pictured in Figure 3.25a, used to create a truss structure. In general, it is desirable to manufacture lattice structures with as small a unit dimension as possible so as to maximize the uniformity of the resulting structure while maintaining a specified effective density. The unit truss is made up of 48 elements of the same length, 12 in the build plane and the remainder inclined by 45°.

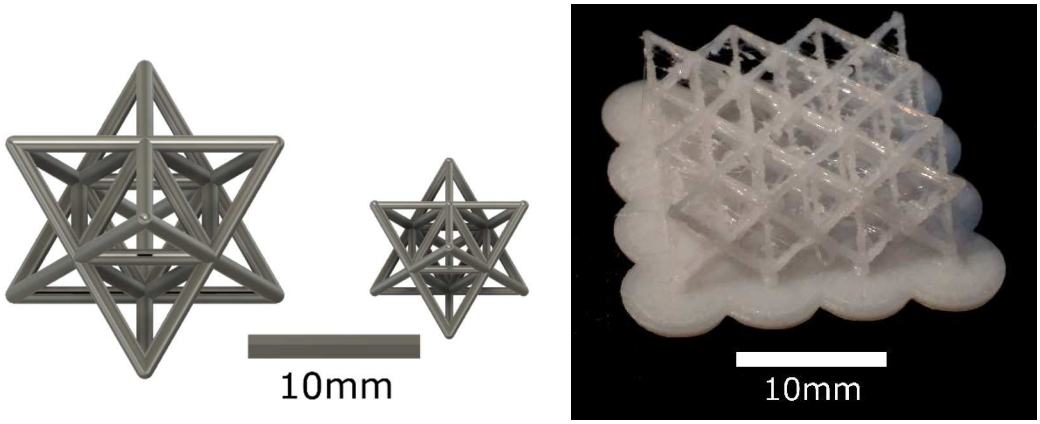

(a) (b) (c)

Figure 3.25. (a) Parametric octet truss lattice element, with 1mm elements (10% effective density; 10.7 mm unit cell). (b) 10% effective density for manufacture using design rule functions for the material extrusion example process (6.10 mm unit cell). (c) Manufactured version of (b), in a 3x3 lattice with a supporting base.

The length and orientation of each cylindrical element was computed as the unit cell size was varied, and a search was performed using the design rule functions derived from the material extrusion data collected above to determine the corresponding minimum feature size. Figure 3.26 shows the effective density (volume ratio), the length/thickness ratio (r_l) for each member type, and the computed minimum element diameter in panels (a)-(c) respectively for the material extrusion example processes. For comparison, a truss composed of bars with fixed diameter of 1.0mm is included. As bars grow longer, the length/diameter ratio is constrained to not exceed 20 so as to stay within the design rule scope. This is a conservative estimate, and additional sample data could be used to produce more correct design rules for such long slender features.

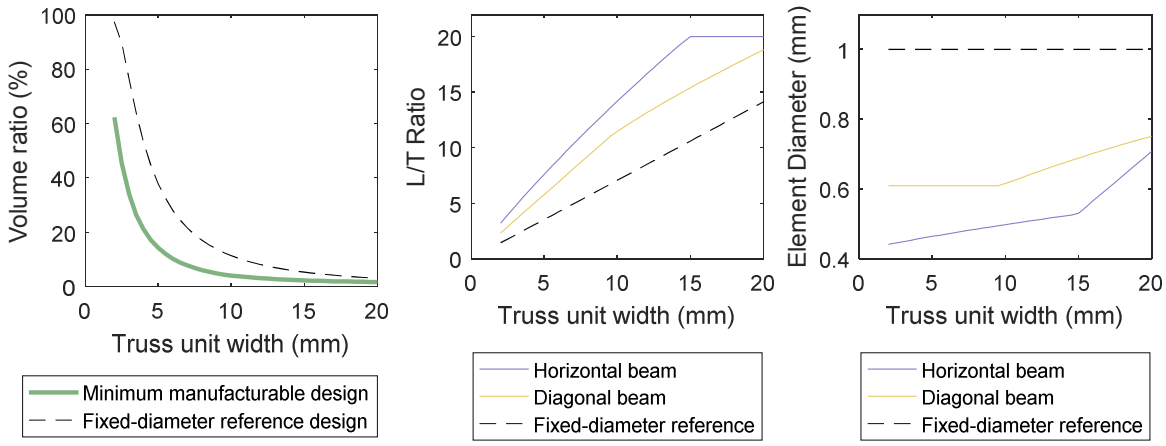

(a) (b) (c)

Figure 3.26. Plots of truss width (a), length/diameter ratio for truss elements (b) and element diameters (c) for the example material extrusion process.

These results demonstrate that the design rule functions allows a 43% decrease in the mesh cell size compared to the 1.0 mm reference case, as the minimum feature size for each individual member can be independently specified based on its manufacturability. The ability of the design rules to incorporate feature shape and orientation information enables the optimized design to fully take advantage of the manufacturing system's capabilities while ensure the resulting designs are manufacturable.

3.9 Recreating the Experiment

The experiment performed in this study answers important questions about the scope and quantity of data needed to produce viable design rule functions for different types of small features. The results presented for the material extrusion example process suggest that predictive design rules over the parameter space of small features can be obtained, but doing so requires significantly more data than is included in most standard AM test artifacts. A numeric presentation of the results above was deliberately avoided, as the design rules generated are specific to the particular process, material, settings, and assessment metric used, and as a result cannot be reliably transferred *verbatim* to other contexts. Different processes, even within the same families, are configured with different layer thicknesses and deposition/fusion diameters;

different materials vary in their mechanical, thermal, and optical properties, all of which have a significant impact at small scale. In addition, the specific user who evaluates the results, and the definition they use as "passing" can significantly change the design rules produced.

The amount of data to collect depends on the tradeoff between desire for high-quality design rules and the cost of the material/machine time required to sample more oriented shapes. A significant benefit of Maximum Entropy Design (MED) is the ability to collect some data, evaluate the preliminary results, and then collect more as needed (Shewry and Wynn, 1987).

To replicate the results presented above on the reader's own AM process, the number of oriented shapes to sample, as well as the number of iterations to use for determining the minimum feature thickness at each point, must both be determined. Eight iterations are needed for logistic regression to be statistically viable (i.e. to obtain about 50 data points in accordance with best practices), however predictive design rules for the material extrusion example process were attained after only six. The appropriate number of iterations will vary with the stochasticity of the process, and careful attention should be paid to the convergence of each feature type as the iterations progress.

To aid in replicating all or part of this experiment, the ordered list of specific feature coordinates evaluated are presented in Appendix B for each dataset. The following steps should be followed when replicating the experiment:

1. Determine initial guesses for the maximum and minimum feature scale for positive and negative features for the first 10-20 MED coordinates, as well as the set of test coordinates.
2. Generate test artifacts with one or more oriented features at scales between the minimum and maximum initial guess
3. Manufacture the test artifact, and evaluate the success of each feature produced
4. Utilize the heuristic or logistic updating schemes to select the next range of features, monitoring the convergence and quality of the data produced
5. Continue from Step 2 until convergence is satisfactory or resources are exhausted
6. Post-process collected data to obtain a single minimum feature size for each oriented shape, and fit a function to the MED data gathered, evaluating against the test data
7. If fit quality is not satisfactory, add subsequent MED coordinates to a new test artifact and continue from step 2, starting again at initial guesses for minimum and maximum feature size.

3.10 Conclusion

A systematic experiment exploring minimum producible size for additively manufactured features of different shapes and orientations has been presented, with results for the material extrusion example process provided and discussed, as well as a description of how the experiment could be adapted to vat photopolymerization and other AM technologies. The approach presented falls in between two types of feature size assessment approaches seen in the literature: Results are more precise than (1) many studies which include only 2-4 small feature types at 3-6 different scales, yet less thorough than (2) exhaustive studies in which dozens of features of different shapes are manufactured at dozens of scales to produce bitmap-style "pass/fail" design rule tables.

Instead of providing design guidelines suitable for use by other researchers, the outcome of this work is a process by which others can characterize their specific additive manufacturing processes, developing their own design rules. An exploration of the tradeoffs between experiment size and accuracy of the predictive design guidelines is presented and informs the proposed characterization process. Although the vat photopolymerization example process evaluated did not produce viable design rules, significant insights were gained in how the procedure could be further adapted to different processes.

Feature shape and orientation were found to have a strong impact on the minimum feature size for the material extrusion example process, with minimum feature thickness varying by as much as an order of magnitude over the surveyed set of features.

In order to capture statistical variation, a single feature shape in a particular orientation must be manufactured many times at various scales before results are reliable. This study, which models the failure of small features using a logistic function, estimates that at least 36 copies of each oriented shape at various scales should be manufactured for the material extrusion example process, 3-8 times the number of samples done in most other studies. By spreading these copies out over several manufacturing runs, an adaptive update scheme is able to adjust the range of

feature sizes to maximize useful information gain, which both reduces the total number of copies manufactured and captures run-to-run variability of the process, while also reducing the dependence of the results on the range of features originally selected by the test artifact designer.

The design rules developed are functions of a parameter space of small features, and enable more granular predictions of the minimum feature size for specific shapes and orientations of small features. By providing more precise (and therefore less conservative) data-driven estimates of minimum feature size, some features with specific shapes can be manufactured as much as 60 % smaller than design rules derived from the NIST test artifact suggest (some features have design rules as low as 0.180 mm, compared to the NIST minimum manufacturable fin thickness of 0.5 mm). In addition, design for additive manufacturing best practices include an overhang angle constraint to prevent manufacturing difficulties when supports are not used. For cylindrical features, sufficient data was collected to entirely remove the overhang angle constraint, as overhanging features which are more difficult to produce have a correspondingly larger minimum feature size, without penalizing shorter features which can be manufactured at any angle. This approach also directly incorporates "bridging" elements where horizontal members connect two supporting entities without requiring a special exception to the design rule.

The experimental scope could be made larger to predict performance over a larger set of parameters for small features can be considered, including rotations about the feature axis, curved features, and interactions between features. A smaller version of the experiment could include a single test artifact containing all the data points needed to characterize a new process over several manufacturing runs. Statistical information from the sub-experiment used to determine the minimum feature size at each sampled shape could be used to provide more accurate design rules and/or control the degree of conservativeness in the resulting design rule functions.

The presented parametric design rule for minimum feature size and overhang angle can improve design performance and process utilization, as demonstrated through the use of two real-world examples, which show significant improvements over alternative approaches.

Chapter 4. Data-Driven Additive Manufacturing Constraints for Topology Optimization

4.1 Preface

The parametric design rules developed in the last two chapters have already been shown to be valuable tools for human designers seeking to create, adapt, or scale models for additive manufacturing. Parametric design rules are also ideally suited for integration into automated design frameworks. Computers can more easily take advantage of the continuous, differentiable design rule functions, and leverage them to ensure that the results are both effective in meeting the user's need and capable of being manufactured. In this chapter, parametric design rules are applied to topology optimization, a burgeoning area of automated design which looks to AM as the realization of its complex optimized designs.

4.2 Abstract

Topology optimization of structures producible using Additive Manufacturing (AM) is explored using a data-driven constraint function derived from extensive experimental data on the minimum producible size of small features in different shapes and orientations (developed previously). This constraint function is applied to topology optimized designs using the Moving Morphable Components (MMC) framework, which is readily adaptable to the shape- and orientation- dependent manufacturing constraint considered. The MMC approach is extended to include a "bootstrapping" which provides initial component layouts to the MMC algorithm based on intermediate SIMP results, improving convergence compared to reference MMC implementations. Results show the manufacturability constraint successfully applied to a variety of compliance design problems, with minor changes in topology and shape compared to fixed-radius filters in SIMP designs while taking better advantage of the achievable complexity in

additive manufacturing processes, resulting in typical penalties to the objective function of 5% or less.

Keywords: Topology Optimization, Additive Manufacturing Benchmarking, Minimum Feature Size, Design Rules.

4.3 Table of Variables

A large number of equations appear in this chapter; this section provides a table of variables used for reference.

Variable	Symbol	Note
Manufacturing (build) direction	$\mathbf{b}$	Unit vector.
Parameters for the kth morphable component	$\mathbf{c}^k$	Where $\mathbf{c}^k = \left[x_1^k, y_1^k, x_2^k, y_2^k, t^k\right]^{\mathrm{T}}$
Components in chain	$Ch(k)$	Returns component indices for each element in the chain containing component k
Global density field	$D(P, \mathbf{z})$	
Young's Modulus	E	
Minimum allowable elastic modulus	E_{min}	
Applied load	$\mathbf{F}$	
Objective function	f	
Thresholded compliance	$\bar{f}$	Compliance computed after thresholding a continuous design so as to maintain the volume constraint.
State equation	$G(\mathbf{z}, \mathbf{U})$	State variable relationship describing problem physics
Constraint functions	$g_i(\mathbf{z}, \mathbf{U})$	Typically, g_0 is the volume constraint
Heaviside function	$H(\phi, \epsilon, \eta)$	Where ϕ is the input, ϵ is the smoothing width, and η is the maximum value (usually 1).
Stiffness matrix	$\mathbf{K}$	The portion corresponding to element e is $\mathbf{k}_e$
Linking matrix for connected morphing components	$\mathbf{L}$	Each row represents a component, each column an endpoint.
Feature length	l	
Minimum allowed skeletal segment length	l_{min}	

Number of constraints	n_g	
Number of FEA elements	n_e	
Size of FEA grid	n_x, n_y	Note that $n_e = n_x n_y$
Number of MMC components	n_c	
Number of junction points	n_p	
Number of links in a chain of components	n_l	
Spatial coordinates of the center of finite element e	$\mathbf{N}^e$	
Density Penalization parameter	p	Always 3 in this work
Point in 3D space	$P = [x, y, z]^T$	
Density filtering radius	r_{min}	Creates an effective minimum feature size of $2r_{min}$
Minimum manufacturable feature thickness function	$S(l, \theta)$	If bridging data is used, the symbol S_b is shown; no bridging is indicated by $S_{\bar{b}}$
MMC component thickness	t	
State variable	$\mathbf{U}$	Displacement vector for solid mechanics problems. The portion corresponding to element e is $\mathbf{u}_e$
Volume of solid material	V	
Volume of the domain Ω	V_0	
Maximum allowed volume fraction	V_f	
Domain width, height	w_d, h_d	In domain units (mm)
Element width, height	w_e, h_e	Note that in this work, only square elements are considered ($w_e = h_e$)
MMC component endpoints	x_1, y_1, x_2, y_2	
Spatial locations	x, y	
Decision variable for optimization	$\mathbf{z}$	The effective definition of $\mathbf{z}$ varies with different approaches; see text.
Distance function	$\Delta(e, j)$	Returns the Euclidian distance between elements e and j
Smoothing for Heaviside function (when computing penalty)	γ	In the continuation approach, the initial value (at iteration 0) is γ_0, and the final value (after a set number of iterations) is γ_f
Smoothing for Heaviside function (when computing density)	ϵ	
Distance field from a single morphable component	ϕ^k	For the kth morphable component

Distance field from the union of all morphable components	ϕ	
Maximum value for Heaviside function	η	
Field of element densities	$\boldsymbol{\rho}$	The density of element e is given by ρ_e
Feature angle from build direction	θ	
Density filtering weight function	ω_{ej}	
Optimization domain	Ω	

Index Variables

Misc. Iterators	i, j	i.e. $g_i = 0$; meaning should be inferred from the context
Current FEA element	e	i.e. the eth element of $\boldsymbol{\rho}$ is ρ_e
Current MMC component	k	As a superscript, as in t^k is the thickness of the kth component

4.4 INTRODUCTION

Additive manufacturing (AM) has become a compelling alternative to traditional manufacturing technologies for the fabrication of complex, organic shapes produced by topology optimization (Liu and Ma, 2016). The layer-by-layer manufacturing technique, compared to older manufacturing processes like casting and machining, removes many considerations which reduce the optimality of the outcome, from constraints on the optimization problem to post processing of the results. The promise of AM to produce parts at fixed cost irrespective of the design complexity in various materials has led to a variety of topology optimization applications, including tissue engineering (Hollister, 2005), mesostructured or lattice materials (Coelho et al., 2011; Gu et al., 2012), auxetic materials (Schwerdtfeger et al., 2011), complex fluid flow channels (Borrvall and Petersson, 2003), heat flow problems (Gersborg-Hansen et al., 2006), and more.

However, despite the removal of constraints applicable to other manufacturing processes, AM brings with it a unique manufacturing considerations (Vayre et al., 2012). Each type of AM process has unique process physics, resulting in unique design constraints. Two well-studied design rules applicable to a broad class of AM features are

1. The minimum feature size (or the smallest element of a design which can be realized by the manufacturing process), and
2. The overhang angle (the maximum degree of overhang achievable by the process without requiring support structures).

Both have been studied in the topology optimization literature, and Liu and Ma (2016) present a recent survey.

Topology optimization seeks to produce highly performant designs, but from the very beginning, manufacturability constrains the problem: Theoretical results from beam and truss layout theory show that the optimal material distribution for many common objectives involve infinitely-many, infinitely-small members (Zhou and Rozvany, 1991). Solid-and-void designs consist of a multitude of complex tiny features as resolution grows (Bendsøe, 1988). Taking full advantage of the capabilities of the manufacturing process to produce small features is therefore important to maximizing the optimality of the design. Both the minimum feature size and overhang constraints typically applied in AM design work to limit the complexity of the resulting designs in significant ways, effectively setting limits on the kind of features (based on orientation and size) which can be produced. The actual manufacturing process is likely capable of producing some features at even smaller scales, but utilizing a constant overhang angle and minimum feature size constraint is straightforward to implement and ensures manufacturing success. For example, short horizontal segments connecting two supporting bodies (called “bridges”) can frequently be manufactured without support on various processes, even though this process exceeds the overhang angle. Alternately, the process may well be able to produce members much smaller than the minimum feature size for some shorter beam elements, depending on the orientation of the feature in the build volume.

In previous chapters, a parametric constraint function for AM processes was explored which provides a more precise set of design rules by experimentally determining a minimum feature size constraint as a function of feature shape and orientation in the build volume. The resulting function can incorporate both overhang and minimum feature size components (by realizing a penalty of a large minimum feature size for overhanging features), which captures more closely the real capabilities of the process, including effects such as bridging.

In this work, the authors apply this constraint function, derived experimentally for a specific AM machine in the material extrusion process category, to the topology optimization domain, presenting a new way of formulating the minimum feature size constraint based on the shape and orientation of the described feature. To accomplish this, the Moving Morphable Component (MMC) framework is used, which allows geometry to be explicitly described in terms of features. To improve convergence, a bootstrapping technique is proposed and implemented, leveraging the fast initial convergence of the SIMP method to provide high-quality starting points for the MMC algorithm. For clarity, the newly-developed variant on the MMC approach presented in this work is termed the "Constrained Bootstrapped Moving Morphable Components", or bcMMC approach.

To the best of the authors' knowledge, this work presents the first instance where a topology optimization formulation incorporates a variable minimum feature size constraint. The results provide manufacturable geometries that more fully take advantage of the complexity capabilities of specific AM processes, improving the optimality of the physically-realizable topology.

After a review of the relevant literature (Section 4.5), the manufacturing constraint is described and applied to the topology optimization problem in Section 4.6, followed by a detailed explanation of the bootstrapped MMC topology optimization methods in Section 4.7. Results of experimental studies are presented in Section 4.8.

4.5 BACKGROUND

The topology optimization problem seeks to divide a design domain Ω into solid Ω_1 and void Ω_0 regions in order to minimize an objective function, usually under a constraint on the volume of the solid region. Evolving from shape and layout optimization (Haftka and Grandhi, 1986) and variable plate thickness algorithms, the first applications of optimization to the design of arbitrary structures with unrestricted topology became known as the SIMP method, developed independently by Bendsoe and Kikuchi (1988) and Zhou and Rozvany (1991). Since this early work, research in the topology optimization area has exploded. Rozvany (2001) provides an excellent survey of the first 15 years of research, while Deaton and Grandhi (2014) and Sigmund and Maute (2013) each survey the present state of the literature. The fundamental optimization problem can be stated as

$$\begin{aligned} \min_{\mathbf{z}} : \quad & f(\mathbf{z}, \mathbf{U}) \\ \text{subject to} : \quad & G(\mathbf{z}, \mathbf{U}) = 0 \\ & g_i(\mathbf{z}, \mathbf{U}) \leq 0, \quad i = 1 \dots n_g \\ & \mathbf{z}_{min} \leq \mathbf{z} \leq \mathbf{z}_{max} \end{aligned} \tag{4.5}$$

where f is an objective functional in the design variable $\mathbf{z}$ and the state variable $\mathbf{U}$; $G(\mathbf{z}, \mathbf{U})$ is a state equation, and the n_g constraint equations g_i restrict the solution space. In compliance minimization, which is the most common topology optimization test problem, the domain Ω is divided into uniformly-sized finite elements and the objective function f is the compliance, leading to the problem statement

$$\min_{\mathbf{z}} : \quad f(\mathbf{z}, \mathbf{U}) = c = \mathbf{U}^T \mathbf{K}(\mathbf{z}) \mathbf{U} = \sum_{e=1}^{n_e} \mathbf{u}_e^T \mathbf{k}_e(\rho_e(\mathbf{z})) \mathbf{u}_e \tag{4.6a}$$

$$\text{subject to} : \quad G(\mathbf{z}, \mathbf{U}) = \mathbf{K}\mathbf{U} - \mathbf{F} = \mathbf{0} \tag{4.6b}$$

$$g_0(\mathbf{z}, \mathbf{U}) = \frac{V}{V_0} - V_f = \frac{1}{V_0} \sum_{e}^{n_e} \rho_e(\mathbf{z}) - V_f \leq 0 \tag{4.6c}$$

$$g_i(\mathbf{z}, \mathbf{U}) \leq 0, \quad i = 1 \ldots n_g \tag{4.6d}$$

$$\mathbf{z}_{min} \leq \mathbf{z} \leq \mathbf{z}_{max} \tag{4.6e}$$

Where the state variable **U** is the displacement vector across the set of elements, and **K** is the global stiffness matrix, which is controlled by the design variables **z** through the density field $\boldsymbol{\rho}(\mathbf{z})$. The state equation is the linear elastic relationship, $\mathbf{KU} = \mathbf{F}$, where **F** is the vector of applied loads. Usually, a volume constraint, g_0 is applied to constrain the volume of the solution obtained to be below some threshold V_f.

Today, topology optimization approaches include hundreds of methods centered around a few key approaches, based on the way the design variable is selected; three of particular import to the current work are presented here and shown graphically in Figure 4.1. For ease of analysis, most approaches divide the design domain into a fixed grid, and allow the density of each element to be independently set as 0 (no material present) or 1 (material present). In *density-based approaches*, the decision variable for optimization directly specifies the density of each element, i.e. $\mathbf{x} = \boldsymbol{\rho}$, and the problem is relaxed to make numerical solution tractable by allowing the densities to vary continuously between zero and one (Deaton and Grandhi, 2014). For several common objectives, derivative information for the individual densities is easy to calculate from the objective and state equations, making gradient-based solution straightforward.

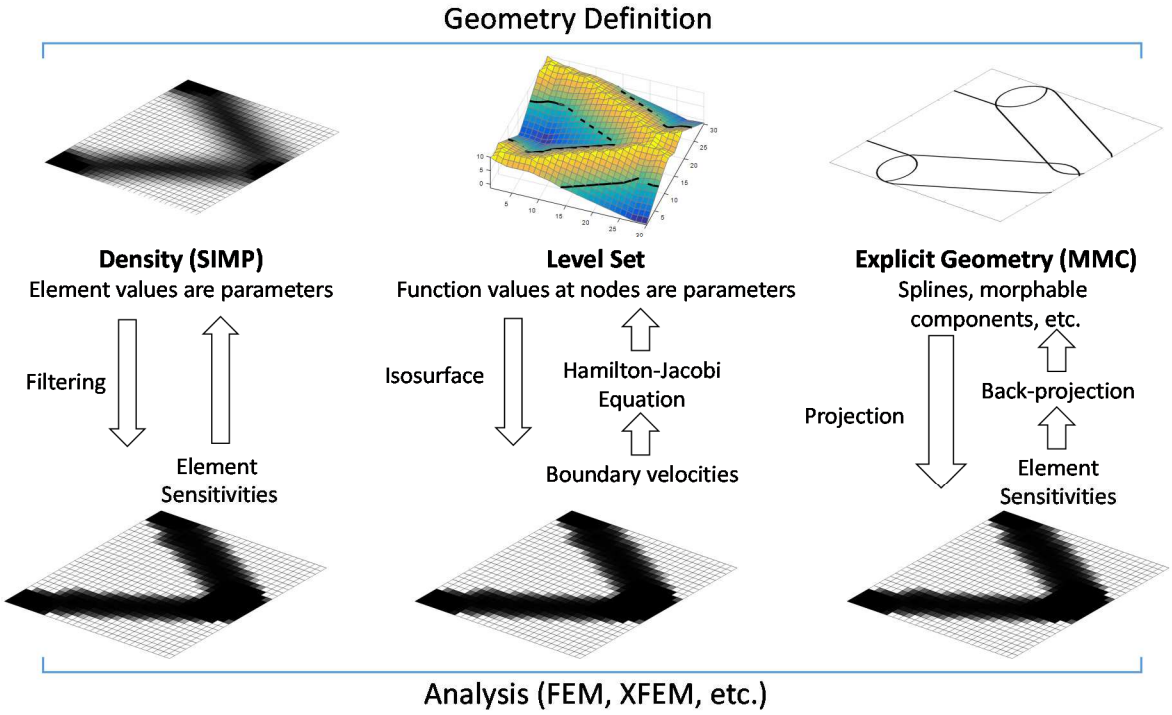

Figure 4.1. Graphical comparison of the density (SIMP), level set, and explicit geometry (MMC) topology optimization methods.

Level set approaches still relax the element density to be continuous, but specify the material and void domains using the level set of higher-dimensional function, and which is typically advected using the derivative information from the FEA solution by solving the Hamilton-Jacobi equation (Burger and Osher, 2005; Luo, 2013). In this formulation, the parameters for optimization are typically the sampled values of the level set function on some grid over the domain (Wang et al., 2003), but sometimes take the form of coefficients of a pre-selected function, such as Kriging interpolation of control points (Guirguis et al., 2015).

In what is here termed *Explicit Geometry Approaches*, some kind of geometric primitive is used as the basic element for manipulating the domain (Guo et al., 2014a; Mei et al., 2008; Takalloozadeh and Yoon, 2017). Primitives used include superellipsoids, offsets of linear elements, and spline curves, among others (see Figure 4.2). Depending on the application, the geometric primitive(s) can be moved, rotated, and morphed (using the primitive's parameters) into various configurations, and then projected onto the FEA domain as solid or void regions.

Sensitivity information propagates backwards through the projection operator to compute the sensitivities for each parameter in each primitive.

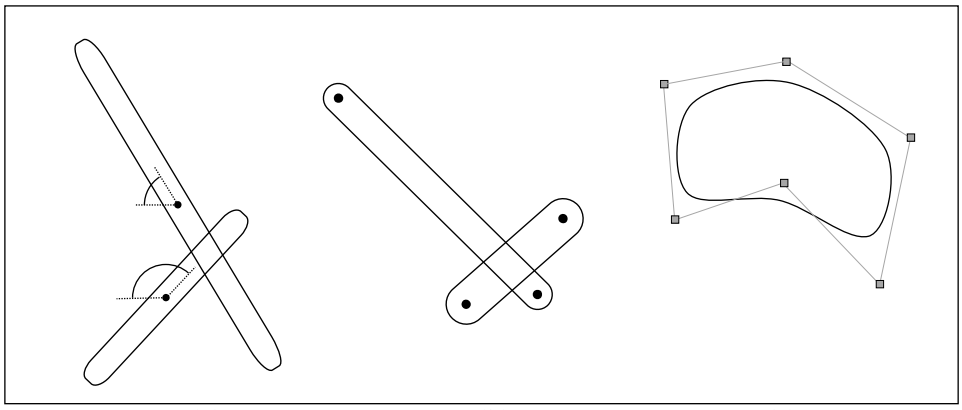

(a) (b) (c)

Figure 4.2. Schematic diagram of selected primitives used in explicit geometry approaches. (a) Hyperellipsoids parameterized by center point, angle, thickness, and length (Guo et al., 2014a) (b)Offsets of line segments, parameterized by end point locations and thickness (Deng and Chen, 2016); (c) Spline curves (Seo et al., 2010).

The above is by no means an exhaustive list of topology optimization approaches, which include significant branches of research in evolutionary structural optimization (Munk et al., 2015), sometimes utilizing non-gradient optimizers (Hiller and Lipson, 2009). As the field has progressed, the similarities between the various areas have grown rather than shrunk, leading some authors to suggest they have become roughly analogous (Sigmund and Maute, 2013).

In the remainder of this section, SIMP (a density approach) and MMC topology optimization algorithms are described, a brief survey of bootstrapping techniques similar to the proposed approach is presented, and manufacturing constraints for topology optimization are reviewed.

A. SIMP: A density-based approach

Solid Isotropic Material with Penalization (SIMP), is the oldest and one of the most widely-employed density-based topology optimization approaches, with founding works in the late 1980's and early 1990's (Bendsøe, 1988; Rozvany et al., 1992). It derives its basic concept from homogenization theory, where the domain is broken into elements, each of which takes on a

different microstructure consisting of varying amounts of solid and void material, allowing the density to be continuously varied without losing the physical meaning of the solution (Guedes and Kikuchi, 1990). Because of the difficulties in manufacturing these microstructures, the formulation is modified to penalize the mechanical performance of intermediate-density materials so the optimizer is encouraged to select solutions with most elements either 0 or 1, forming the "P" in SIMP (Bendsøe, 1988; Zhou and Rozvany, 1991).

The optimization problem solved in SIMP can be derived from the general problem statement in Equation (4.6) with the following definitions, using the formulation of Andreassen (2011).

$$\begin{aligned} &\boldsymbol{\rho}(\mathbf{z}) = \mathbf{z} \quad \Rightarrow \quad \rho_e = z_e \\ &\mathbf{k}_e\big(\rho_{\mathbf{e}}(\mathbf{z})\big) = [E_{min} + \rho_e(\mathbf{z})^p(1 - E_{min})]\mathbf{k}_0 = \big[E_{min} + z_e^p(1 - E_{min})\big]\mathbf{k}_0 \\ &\mathbf{z}_{min} = 0; \mathbf{z}_{max} = 1 \end{aligned} \tag{4.7}$$

Here, the design variable is mapped directly to density, and the stiffness for each element $\mathbf{k}_e$ is a product of the fully-dense element stiffness matrix $\mathbf{k}_0$ and an effective modulus of elasticity, ranging between E_{min} and 1, as allowing $\mathbf{k}_e$ to take the value zero creates singularities in the global stiffness matrix. This places very low stiffness elements in the void regions, an approximation which allows a valid solution to the FEA equation without removing the void elements completely.

To avoid gray elements in the solution, the SIMP penalization exponent $p > 1$ is introduced in the construction of $\mathbf{k}_e$ in Equation (4.7)). This causes the effective modulus of intermediate-density elements to be less than a linear interpolation between E_{min} and 1, which makes the element's cost (in its contribution to the volume constraint) comparatively greater than its contribution to the overall stiffness, driving solutions towards binary 0-1 fields. Functionally, the gray elements in the un-penalized SIMP solutions can be thought of as corresponding to infinitely-fine microstructure in the optimal object, creating an effective intermediate-density material. With penalization, SIMP creates larger structures which approximate this intermediate-density material. Improved objective function values can be attained by slowly increasing the penalization

parameter p from 1 to 3, as suggested by Bendsøe and Sigmund (2003, p. 22). In this work, when such a continuation scheme for p is utilized, it will be noted in the text.

Derivative calculations for compliance problems are easily found from the FEA equations (see Appendix D for a derivation). Specifically,

$$\begin{aligned}\frac{\partial f}{\partial z_e} &= \mathbf{u}_e^T \frac{\partial \mathbf{k}_e\big(\rho_e(\mathbf{z})\big)}{\partial z_e}\mathbf{u}_e = -p z_e^{p-1}(1-E_{min})\mathbf{u}_e^T\mathbf{k}_0\mathbf{u}_e \\ \frac{\partial V}{\partial z_e} &= \frac{\partial}{\partial z_e}\rho_e = \frac{\partial}{\partial z_e} z_e = 1\end{aligned} \tag{4.8}$$

One key deficiency of early optimization approaches is the "checkerboarding" effect, in which the optimizer takes advantage of the simply-connected FEA mesh to create alternating solid and void voxels to avoid the penalization but maintain an effective intermediate-density material (Sigmund and Petersson, 1998). Effective solutions include explicit constraints on perimeter length, as well as filtering of the sensitivity and/or density fields, which create an effective "minimum feature size" larger than one FEA element (Bourdin, 2001). Density filtering was later validated using solid mechanics theory (Sigmund and Maute, 2012). A simple density filter is that of Bruns and Tortorelli (2001), in which the design variable field $\mathbf{z}$ is abstracted from the field $\boldsymbol{\rho}$ used for analysis as follows:

$$\begin{aligned}\rho_e(\mathbf{z}) &= \frac{1}{\sum_{j\in n_e}\omega_{ej}}\sum_{j\in n_e}\omega_{ej} z_j \\ \omega_{ej} &= \max\big(0, r_{min} - \Delta(e,j)\big) \\ \Delta(e,j) &= \sqrt{(j_x - e_x)^2 + \big(j_y - e_y\big)^2}\end{aligned} \tag{4.9}$$

The filter redefines density at each element which depends on a weighted average of the design variables in a circular region around the element, with mesh-independent radius r_{min}. The weighting function is linear in the distance between the centroids of element e (e_x, e_y) and element j (j_x, j_y). The effect of this filter on the sensitivities is derived using the chain rule, as seen in Andreassen et al. (2011).

Additional filters were introduced to help further prevent gray elements at the solid/void transition. For example Guest et al. (2004), which uses a smoothed Heaviside projection of the design variables, and is utilized for SIMP examples in this work unless otherwise stated. Hundreds of other works extend and adapt the SIMP method to a variety of problem domains (Park and Sutradhar, 2015; Sigmund, 1997, 2001a; Zhao et al., 2017), provide new and robust filters and constraints (Sigmund, 2009; Yoon et al., 2004), and adapt the process to produce real-world implementable results (Schramm and Zhou, 2006; Tomlin and Meyer, 2011). A variety of researchers have also provided sample codes for demonstrating the SIMP algorithm (Andreassen et al., 2011; Liu and Tovar, 2014; Sigmund, 2001b).

When topology optimization solutions are compared, especially between different filters or different frameworks, care must be taken to ensure an accurate estimate of the relative quality of each solution. The compliance objective function used in this work includes a penalization term for intermediate-density elements, and different filters and frameworks may inherently possess varying amounts of gray around feature edges. When comparing solutions, then, the "thresholded compliance" will be used, denoted $\bar{f}$. To compute thresholded compliance, the continuous density field (including gray elements) is converted to a black-and-white binary design by selecting a threshold cutoff which satisfies the volume constraint of the problem. The compliance of this binary design is then computed without penalization and reported as the thresholded compliance.

B. Moving Morphable Components: An Explicit Geometric Approach

Moving Morphable Components (MMC), is the title recently given to a class of topology optimization approaches which use parametric primitives that can be translated, rotated, and reshaped under the control of the optimizer (Guo et al., 2014a; Norato et al., 2015). Similar ideas had been presented in the literature before, i.e. in the level set community for defining explicit level-set functions (Hamza et al., 2013; Pingen et al., 2010), in the SIMP community as a way to incorporate deformable void regions (Clausen et al., 2014), in the use of spline curves for shape

optimization problems, including more recent works which handle topology changes and use isogeometric analysis (Haftka and Grandhi, 1986; Seo et al., 2010), and in the shape-morphing topology optimization of Mei et al. (2008).

MMC differs from level set and density approaches in that the decision variables correspond to parameters of the components themselves with explicit geometric meaning, instead of implicitly defining a function over the domain (as both level sets and filtered density methods can be thought of as doing). The bcMMC approach described later in this paper builds on MMC and CMC (connected morphable components, described shortly) formulations from several authors (Deng and Chen, 2016; Norato et al., 2015; W. Zhang et al., 2016b). These works are combined in this section to present a version of MMC which leverages aspects of each in a formulation which forms the foundation for the improvements described in subsequent sections.

The MMC Formulation

Consider the morphable component shown in Figure 4.3, which illustrates the kth component in the domain. The component is parameterized by the locations of each endpoint and the element thickness, enabling translation, rotation, and shape change of the component, and following the same form used in Norato et al. (2015) and Deng and Chen (2016). The portion of the decision variable $\mathbf{z}$ which defines the state of this component is $\mathbf{c}^k = \left[x_1^k, y_1^k, x_2^k, y_2^k, t^k\right]^{\mathrm{T}}$ and the decision variable is constructed by joining together the parameters for each component, i.e. $\mathbf{z} = [(\mathbf{c}^1)^{\mathrm{T}}, (\mathbf{c}^2)^{\mathrm{T}}, \dots, (\mathbf{c}^{n_c})^{\mathrm{T}}]^{\mathrm{T}}$. A Euclidian distance field from the kth component is created, ϕ, similar to the topology description function of W. Zhang et al. (2016b). ϕ has positive values inside the component, zero values on the boundary, and negative values outside. Mathematically, let a component k have end points $\mathbf{P}_1^k = \left[x_1^k, y_1^k, 0\right]^T = \left[c_1^k, c_2^k, 0\right]^T$ and $\mathbf{P}_2^k = \left[x_2^k, y_2^k, 0\right]^T = \left[c_3^k, c_4^k, 0\right]^T$ and half thickness $t^k = c_5^k$, where subscripts of c indicate corresponding elements in the $\mathbf{c}^k$ vector. The distance field from the component to any point $\mathbf{P}$ in the domain is

$$\phi(\mathbf{P}, \mathbf{z}^k) = \begin{cases} \Delta\left(\mathbf{P}, \mathbf{P}_1^k\right) - t^k & \text{if } \left(\mathbf{P} - \mathbf{P}_1^k\right) \cdot \left(\mathbf{P}_2^k - \mathbf{P}_1^k\right) \leq 0 \\ \Delta\left(\mathbf{P}, \mathbf{P}_2^k\right) - t^k & \text{if } \left(\mathbf{P} - \mathbf{P}_2^k\right) \cdot \left(\mathbf{P}_2^k - \mathbf{P}_1^k\right) \geq 0 \\ \dfrac{\left|\left(\mathbf{P}_2^k - \mathbf{P}_1^k\right) \times \left(\mathbf{P} - \mathbf{P}_1^k\right)\right|}{\left|\mathbf{P}_2^k - \mathbf{P}_1^k\right|} - t^k & \text{otherwise} \end{cases}$$

where $\Delta(A, B)$ again represents the Euclidian distance between points A and B. Figure 4.4a-c illustrate the construction of the signed distance field graphically.

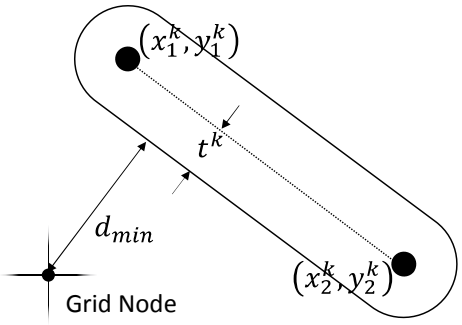

Figure 4.3. A schematic of a moving morphable component.

To construct the density field, a Heaviside (unit step) function is applied to the distance field for each component. To help maintain differentiability of the projection, a smoothed Heaviside function[6] is used instead, similar to that used by W Zhang et al. (2016b), and takes the form,

$$H(\phi, \epsilon, \eta) = \begin{cases} \eta & \text{if } \phi > \epsilon \\ \dfrac{3\eta}{4}\left(\dfrac{\phi}{\epsilon} - \dfrac{\phi^3}{3\epsilon}\right) + \dfrac{\eta}{2} & \text{if } -\epsilon \leq \phi \leq \epsilon \\ 0 & \text{otherwise} \end{cases} \tag{4.10}$$

with parameters ϕ, the distance to the component, ϵ the regularization parameter which sets the width of the smooth transition, and η, the maximum value of the result (equal to 1; see Figure 4.4d). The smoothed Heaviside projection is applied to the signed distance field ϕ to compute the density at each finite element node (shown in 1D in Figure 4.4e and in 2D in Figure 4.4f). Note that the signed distance field representation provides unit gradients for the ϕ field,

[6] All other authors do not include η as a parameter in H, setting it to 1 (fully dense) instead. It is included here to avoid confusion later, and by setting $\eta = 1$ the original papers' algorithm is entirely recovered.

which makes the results of the Heaviside projection more uniform than in the superellipsoid representation selected by W Zhang et al. (2016b), while avoiding the volume fraction construction of Norato et al. (2015).

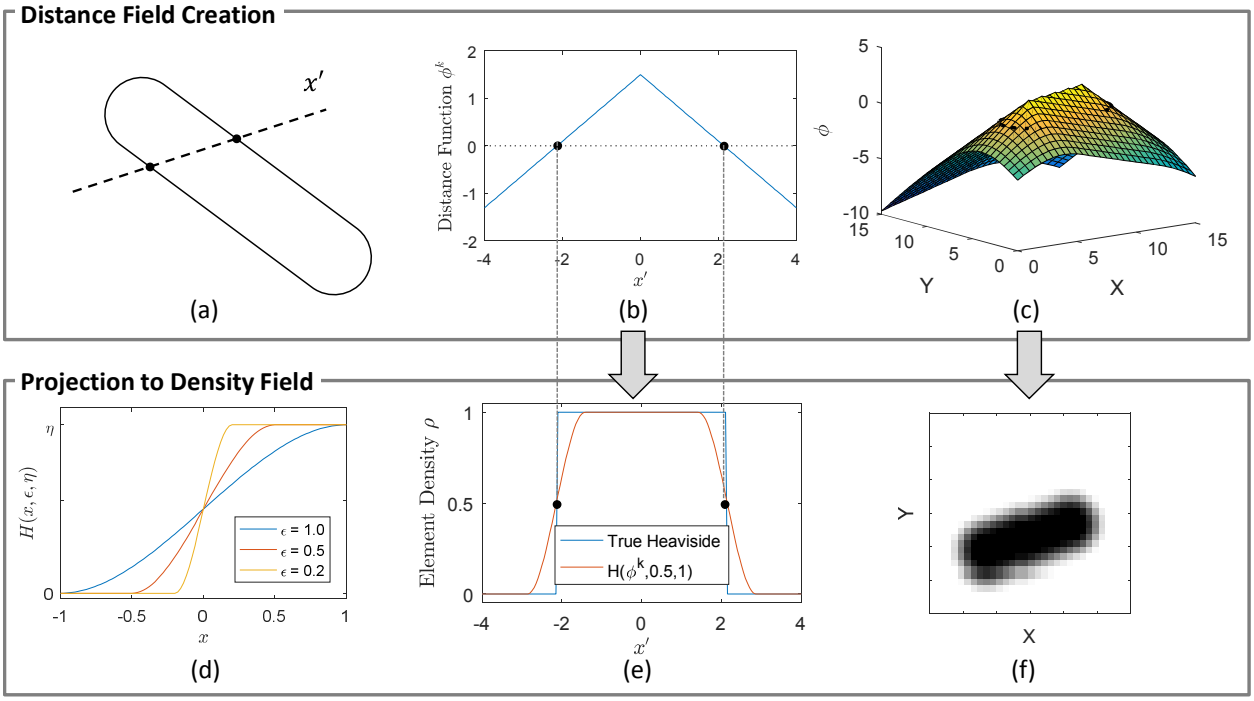

Figure 4.4. Illustration of the signed distance field and smoothed Heaviside projection. (a) a morphable component, intersected by an arbitrary line, x'. (b) The signed distance function ϕ from the morphable component along the x' line. (c) A visualization of the signed distance field over the 2D space. (d) The smoothed Heaviside projection function. (e) The Heaviside projection of the signed distance line plot in (b). (f) The density field created from the Heaviside projection applied to the 2D signed distance field.

When two morphable components are present[7], the combined density field D at point $\mathbf{P}$ is constructed by taking the maximum over the density fields for each individual element, i.e.

$$D(\mathbf{P},\mathbf{z}) = \max_{j=1..n_c} H\left(\phi\left(\mathbf{P},\mathbf{c}^j\right),\epsilon,\eta^k\right). \quad \text{recall } \mathbf{z} = [(\mathbf{c}^1)^{\mathrm{T}},(\mathbf{c}^2)^{\mathrm{T}},\dots,(\mathbf{c}^{n_c})^{\mathrm{T}}]^{\mathrm{T}} \tag{4.11}$$

[7] Most authors, especially W. Zhang et al. (2016b) whose development this section most closely follows, perform the combination of multiple components before the Heaviside function, so that $D(\mathbf{P},\mathbf{z}) = H(\max_j \phi\left(\mathbf{P},\mathbf{z}^j\right),\epsilon,\eta)$. The presentation given here reverses the order of these operations. Since H is monotonically increasing, this has no effect on the results obtained, and avoids confusion later in the paper.

The max function is not differentiable, and some authors use a softmax instead (Norato et al., 2015), while others argue that the discontinuities in the max function are sufficiently rare to not impact the derivative calculations in practice (W. Zhang et al., 2016b).

The function D is sampled at the center of each finite element, similar to the approach of Norato et al. (2015).

$$\rho_e(\mathbf{z}) = D(\mathbf{N}^e, \mathbf{z}) = \max_{j=1..n_c} \left[H\left(\phi\left(\mathbf{N}^e, \mathbf{c}^j\right), \epsilon, \eta\right)\right] \tag{4.12}$$

Finally, the MMC topology optimization problem can again be stated using the general optimization problem in Equation (4.6), with the additional specification of $\mathbf{k}_e(\rho_e(\mathbf{z}))$ as

$$\mathbf{k}_e(\rho_\mathbf{e}(\mathbf{z})) = [E_{min} + \rho_e(\mathbf{z})^p(1 - E_{min})]\mathbf{k}_0 \tag{4.13}$$

which matches the SIMP penalization structure, even though the Heaviside projection restricts intermediate densities to only occur at element boundaries. Unlike SIMP, the design variables $\mathbf{z}$ are the parameters of the bar components, $\mathbf{z} = [(\mathbf{c}^1)^\mathrm{T}, (\mathbf{c}^2)^\mathrm{T}, \dots, (\mathbf{c}^{n_c})^\mathrm{T}]^\mathrm{T}$, where $\mathbf{c}^k = \left[x_1^k, y_1^k, x_2^k, y_2^k, t^k\right]^\mathrm{T}$ specifies the variables of the kth component. Note that the minimum and maximum bounds on $\mathbf{z}$ are more complex than in the SIMP case, dependent on the domain shape and range of acceptable element thicknesses.

Derivatives are computed using the chain rule. The FEA analysis already provides the derivative of the objective function with respect to each element density, so the derivative with respect to the design variables can be obtained as

$$\begin{aligned} \frac{\partial f}{\partial z_j} &= \sum_{e=1}^{n_e} \frac{\partial f}{\partial \rho_e}\left(\frac{\partial \rho_e}{\partial z_j}\right) = -\sum_{e=1}^{n_e} q\rho_e^{q-1}(1 - E_{min})\mathbf{u}_e^T\mathbf{k}_0\mathbf{u}_e\left(\frac{\partial \rho_e}{\partial z_j}\right) \\ \frac{\partial \rho_e}{\partial z_j} &= \frac{\partial D(\mathbf{N}^e, \mathbf{z})}{\partial z_j} \end{aligned} \tag{4.14}$$

The remaining partial derivative, that of each nodal density with respect to each design variable, is computed numerically, following the approach of W Zhang et al. (2016b) and Deng and Chen (2016). Norato et al. (2015) symbolically computes this derivative term in their approach, which uses a soft max function to make ρ_e fully differentiable. Note that the numeric approximation does not require multiple FEA evaluations, only two projections for each design variable onto each density. The benefit is ease of implementation and experimentation, at the cost of additional (linear-scaling) compute time required to numerically estimate the partial derivatives in the last term of Equation (4.14) at each iteration.

Connected Moving Morphable Components

A variant of the general MMC formulation, Connected Morphing Components (CMC), presented by Deng and Chen (2016) is relevant to the current work. Their formulation addresses maximizing compliance (i.e. creating springs), and to prevent degeneration of the design by the optimizer utilizing the low stiffness of void elements to create artificial solutions to the problem they explicitly link components together to form a chain. Consider Figure 4.5, where a series of three components are shown. Deng and Chen explicitly set the endpoints of adjacent components to be equal (i.e. $x_2^1 = x_1^2;\ y_2^1 = y_1^2$) so that the optimizer cannot separate them. This is done before starting the optimization process, and links cannot be added or broken.

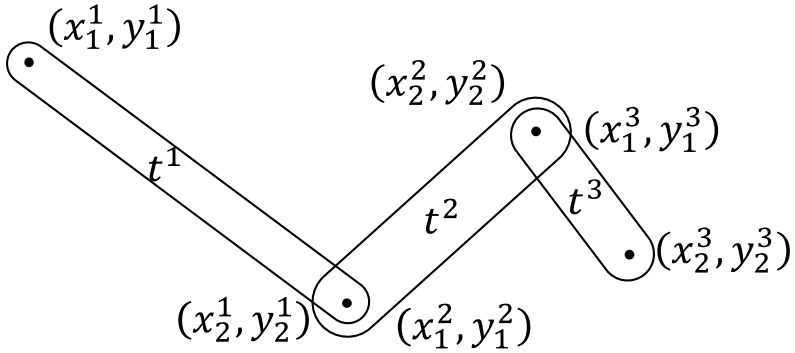

Figure 4.5. Connected morphing components schematic diagram. Recall that superscripts indicate component number and subscripts denote the start/end point on the line. So x_2^1 is the second x coordinate of the first component.

Other Extensions

Various extensions to the basic MMC framework have been proposed, including using different primitive shapes, including trapezoids and offsets of smooth curves (Guo et al., 2016; W. Zhang et al., 2016c, 2016b). Primitives can be connected together to form end-to-end chains either automatically in the problem parameterization, as shown above (Deng and Chen, 2016), or using a penalizing term for loose ends (Hoang and Jang, 2017). Extensions to 3D have been made, where the primitives become plates or bars (S. Zhang et al., 2016; Zhang et al., 2017a). It has been applied to ensure the manufacturability of the resulting structures (when made from readily-available stock) (Norato et al., 2015), provides an explicit upper bound on the resulting complexity (by limiting the number of initial primitives) (Zhang et al., 2017b), and avoids both the checker-boarding effect of SIMP and the level set reinitialization steps required for level set approaches. In a complimentary formulation, "Moving Morphable Voids" sets the parameterized primitives to be B-Spline curves defining the void regions of the domain (W. Zhang et al., 2016a).

C. Bootstrapping Approaches

Bootstrapping refers to the idea of leveraging existing resources to produce a more complex or capable outcome. In this paper, *Bootstrapping* is used to refer to using topology optimization to create an initial condition (or intelligent starting point) for a secondary process, as described in detail in a subsequent section. Although the term is specific to this paper, similar concepts have been applied in various places when transforming the results of topology optimization into manufacturable CAD models.

Bremicker et al. (1991) proposed a bootstrapping approach beginning with a SIMP solution to a given load case, extracting the topology using shape skeletons, and then performing a shape optimization on the resulting truss. Shape skeletons are a tool frequently used in computer vision to extract a single-pixel-wide line that follows the center of a maximally-inscribed ball at each point in the interior of a geometry (Siddiqi and Pizer, 2008), while preserving its topology. This

allowed more accurate, form-fitting FEA meshes to be applied once SIMP had selected a basic shape, and produces more optimal results.

A similar process, whether fully automated or requiring human intervention, is very common in practical applications of topology optimization. For example, the industrial case study by Chang and Tang (2001) utilizes a commercial shape optimization code (OptiStruct), uses a semi-automated process to fit lofted surfaces to the optimization output, and then performs a shape optimization to further refine the design. This further refinement helps alleviate any objective function loss which occurred from imperfections in the fitting process. The flow Chang and Tang use in their process is shown in the flowchart in their paper, reproduced below in Figure 4.6.

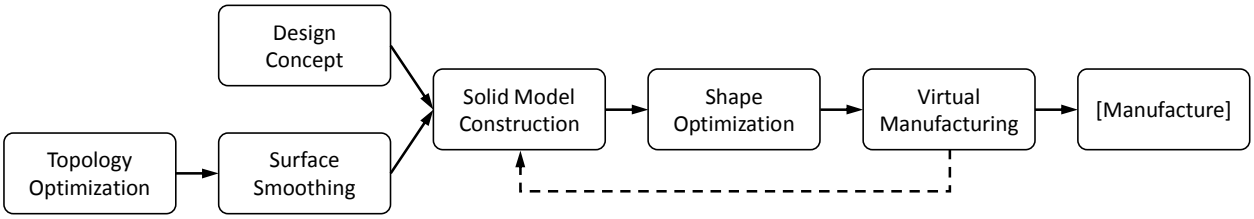

Figure 4.6. Flowchart of the bootstrapping process used by Chang and Tang (2001), adapted from Figure 1 in the same.

In a recent review, Sigmund and Maute point out the need for more topology optimization research in so-called "Hybrid approaches" in which the benefits of two topology optimization approaches are combined to remove initial condition sensitivity and improve convergence (2013, p. 1050). The proposed method seeks to fill this void in the literature.

D. Manufacturing Constraints in Topology Optimization

A recent survey by Liu and Ma (Liu and Ma, 2016) reviews various approaches for incorporating manufacturing constraints into the topology optimization problem, in order to avoid time-consuming post-processing steps which often destroy the (local) optimality of the solution. Constraints in traditional (non-AM) manufacturing processes adapted to various topology optimization approaches include access to interior voids (Ngim et al., 2007), design restrictions

for casting and extrusion (Harzheim and Graf, 2006; Leiva et al., 2004; Schramm and Zhou, 2006; Zhou et al., 2002), and optimization of fiber-layup assemblies (Yan et al., 2017). MMC is proposed as a method to constrain the optimizer to use only materials which can be cut from available stocks in Norato et al. (2015). Industrial interest in topology optimization has pushed additional focus on the manufacturing constraint problem (Tomlin and Meyer, 2011).

For additive manufacturing applications, many constraints are relaxed, and most of the methods proposed above are too stringent (Liu and Ma, 2016). Several Design for Additive Manufacturing (DfAM) frameworks have emerged, involving varying degrees of interaction with the designer (Chu et al., 2008; Vayre et al., 2012). The two most-studied constraints for additive manufacturing are the minimum feature size and the maximum overhang angle.

Minimum feature size has been thoroughly explored in the SIMP approach as a side effect of the filtering used to eliminate checker-boarding and mesh-dependence, and Lazarov et al. (2016) survey these approaches in the context of manufacturability. Level set methods can also constrain the minimum feature size (Wang and Wang, 2004), as can evolutionary structural optimization (Harzheim and Graf, 2006). Constraints on the minimum and maximum thickness associated with the shape skeleton of the design computed at each iteration have been successfully used to simultaneously constrain the minimum and maximum feature, which is desirable for injection molded designs; Guo et al. (2014b) for level sets and Zhang et al. (2014) for SIMP. In the MMC framework, minimum feature size for each component is easy to control by constraining the minimum thickness of each primitive, but narrow hinges can still form where two members overlap just slightly, resulting in researchers enforcing penalties on nearly-overlapping components (Hoang and Jang, 2017).

Overhang angle has also been studied, but far less extensively, and Figure 4.7 presents results from several recent approaches. Figure 4.7a-c utilize asymmetric filters and projections in a density approach to ensure solid elements are only allowed in locations with appropriate support (Driessen, 2016; Gaynor, 2015; Langelaar, 2017). Note in Figure 4.7a the way the inclined faces,

which are usually much shallower, have been constrained to 45°, at the cost of an overall shift in the placement of the beams and additional material spent in supporting members for horizontal elements. The arrow in Figure 4.7b points to a difficulty with the filtering approach, in that intermediate density elements can be leveraged to "build on air," making the design not realizable. In designs which require significant horizontal structures for the optimized configuration, supporting elements are required, which may or may not contribute much to the overall objective, exemplified by Figure 4.7c; note that many of these supporting elements are very thin. The penalty to the objective function from imposing an additional minimum feature size constraint would be significant.

Figure 4.7d presents the work of Guo et al. (2017), in which specific constraints are built into the formulation of the Moving Morphable Voids approach to ensure the result follows the overhang angle constraint, but the changes to the resulting geometry are again severe, resulting in a 14% penalty in the objective function. Figure 4.7e shows a representative result from the MMC formulation included in the same Guo et al. paper in which overhang angle is explicitly constrained. The orientation of the part on the build plate is included as a decision variable for the optimizer, resulting in minimal shape change being required and only a 1% increase in the objective function. Liu and Ma (2016) cite overhang angle constraints as a significant unsolved problem in topology optimization for AM, citing the substantial change in shape (and corresponding objective function penalty) created in most approaches.

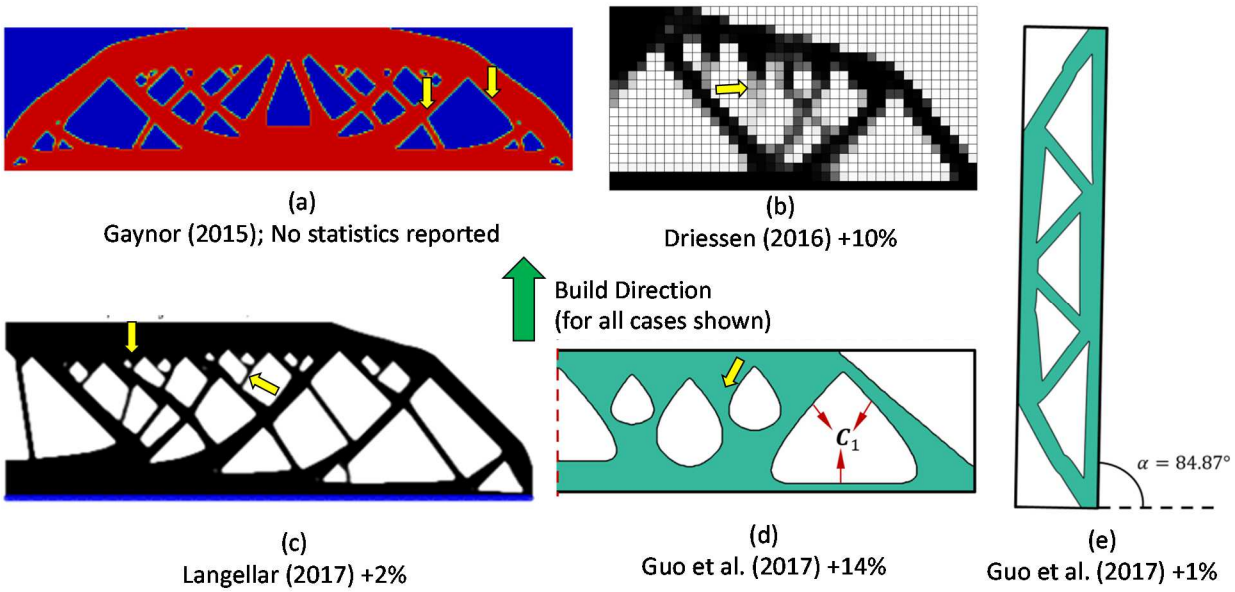

Figure 4.7. Selected results from overhang angle constraint publications. Percentages represent increase over the unconstrained optimization problem. (a) The filter in Gaynor (2015) (b) The filter proposed in Driessen (2016) (c) The explicit downward filter from Langelaar (2017). (d) and (e) show results from Guo et al (2017) for their Moving Morphable Voids and MMC implementations, respectively.

4.6 Data-Driven Manufacturing Constraints

In this section, the conceptual basis for the proposed additive manufacturing constraint is presented; in the next section the details of its implementation in the bcMMC method are discussed in more detail.

In Chapters 2 and 3, the authors created a piecewise-continuous polynomial minimum feature size constraint function for small features applicable to a variety of AM processes, including results for a machine in the material extrusion process category and one in the vat photopolymerization process category. Features are parameterized based on their length/diameter ratio and angle from the build direction (see Figure 4.8), and by fitting polynomial functions to the minimum feature sizes determined for various shapes and orientations, a function of minimum feature size (i.e. minimum feature diameter) is constructed.

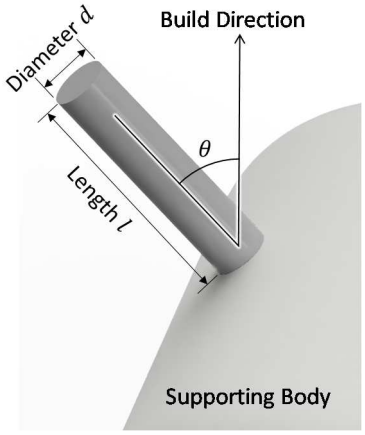

Figure 4.8. Schematic diagram of a parametric small feature.

Instead of an explicit overhang constraint, features which are difficult to produce are experimentally found to require significantly larger minimum diameter. This automatic penalization of longer overhanging features reduces the need for an explicit overhang constraint. Since some data in the experiments include bridging features, bridges can be accounted for in the resulting constraint function and allowed to be present in designs. This ability to incorporate bridges with data-driven sizing information is a major advantage of the present approach over overhang angle constraints, as it reduces the need for the optimization algorithm to change the topology or add supporting features to achieve a manufacturable outcome.

To apply this minimum feature size function to the topology optimization problem, the structure is assumed to extend a relatively small distance into the plane, so that most features are roughly square in cross-section, and manufacturing constraints from small cylinders are assumed valid for these square features. In addition, the constraint function is transformed so as to depend on length and angle directly, making application in topology optimization more direct[8]. The resulting constraint functions for the material extrusion machine, with and without bridging data,

[8] This transformation is done using a dense sampling over the parameter space in the output, and for each point performing a direct search for the best matching feature in the original parameter space. Note that features are constrained to have length/aspect ratios of at most 20, in accordance with the scope of the original experiment. Separate fits for bridging features are used along the 90° axis, with a 5° linear transition to the broader constraint function.

are shown in Figure 4.9, and denoted $S_b(l,\theta)$ and $s_{\bar{b}}(l,\theta)$, respectively, where l is feature length and θ is the angle between the feature axis and the build direction.

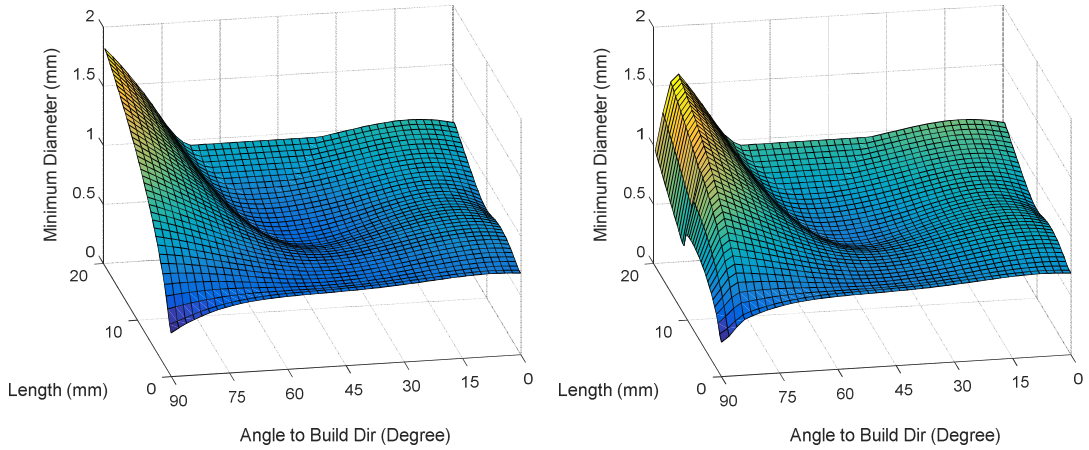

Figure 4.9. The feature-driven constraint function. (a) Without "bridging" features, (b) With "bridging" features at 90°.

The constraint function depends on both the shape and orientation of the feature being manufactured, and is therefore very difficult to implement in a SIMP context, where this information is not readily available. Appendix F presents an early attempt to integrate SIMP with a feature-based constraint function, but the results are oscillatory and noisy due to the computation of the shape skeleton in each iteration.

At each update in the bcMMC framework, each component is assigned a separate minimum thickness value based on its shape and orientation, which are immediately available (they are the decision variables used by the optimizer). Elements with thicknesses smaller than the assigned minimum cannot be produced and should not be included in the final design. Mathematically, the minimum thickness t_{min}^k for the kth component, is computed as,

$$\begin{aligned} t_{min}^k &= t_{min}(\mathbf{c}^k) = \tfrac{1}{2} S\left(l(\mathbf{c}^k), \theta(\mathbf{c}^k)\right) \\ l^k &= l(\mathbf{c}^k) = \Delta(\mathbf{P}_1^k, \mathbf{P}_2^k) + 2t^k \\ \theta^k &= \theta(\mathbf{c}^k) = \cos^{-1}\left(\text{abs}\left(\mathbf{b} \cdot \frac{\mathbf{P}_1^k - \mathbf{P}_2^k}{|\mathbf{P}_1^k - \mathbf{P}_2^k|}\right)\right) \end{aligned} \tag{4.15}$$

where S is one of the constraint functions S_b or $S_{\bar{b}}$, **b** is a unit vector in the manufacturing (build) direction, and $\mathbf{P}_i^k$ are the control points of a moving morphable component, defined as before: $\mathbf{P}_1^k = \left[x_1^k, y_1^k, 0\right]^T = \left[c_1^k, c_2^k, 0\right]^T$ and $\mathbf{P}_2^k = \left[x_2^k, y_2^k, 0\right]^T = \left[c_3^k, c_4^k, 0\right]^T$ along with the half-thickness $t^k = c_5^k$. Note that in order to be compatible with the (half) thickness definition used in the MMC formulation, the t_{min}^k returned is the one half the diameter of the smallest manufacturable feature. Note also that the length of the beam can be found by adding twice the (half) thickness to the distance between the control points (see Figure 4.3). Finally, the features considered in the manufacturing constraint function span between 0° and 90°, since components are always assumed to be supported from the lower edge. The absolute value ensures that the values for θ returned are within that range.

As pointed out in Guo et al. (2017), the design direction used when setting up an optimization problem need not correspond to the orientation in which manufacturing is performed. In that work, the manufacturing orientation is included as an optimization parameter to great effect. For simplicity in the present approach, the manufacturing direction is selectable along any of the sides of the design domain, with the intent that the bcMMC code could be run for a set number of iterations in each orientation, and the best one selected for continued optimization.

Note that the approach presented here does not handle “V”-like connections (see Figure 4.10) between members, where each component is individually manufacturable, but the junction is not supported from below. This situation is easy to detect in post-processing by looking at the component arrangement, and easy to fix by the addition of single point supports which can be removed after manufacture.

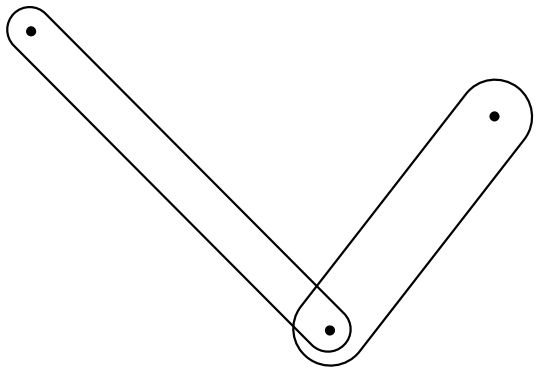

Figure 4.10. A "V"-like connection, where each individual member is manufacturable (satisfying an overhang constraint), but the combination is not supported from the bottom and therefore cannot be created by the AM process.

4.7 Bootstrapped Constrained Moving Morphable Components

In this section, the details of the bcMMC approach are presented, highlighting the unique aspects which enable the data-driven manufacturing constraint to be integrated as well as the bootstrapping method used. The approach builds upon the MMC and CMC formulations presented in Section 4.5, and gives only the salient differences from existing literature.

A high-level overview of the process for bcMMC is shown in Figure 4.11; details of the constraint enforcement and bootstrapping are provided in the following subsections. The algorithm takes as input an optimization domain, load and support conditions, and an "up" direction for manufacturing (Figure 4.11a). In the bootstrapping portion of the process, the domain, loads, and supports are provided to SIMP, which optimizes for 35-70 iterations (Figure 4.11b). Then, the SIMP solution converges quickly to a near-optimal solution, but is unable to handle the feature-driven constraints. Instead, the density field is converted into a set of connected morphable components (Figure 4.11c) which serve as the starting guess for the constrained MMC optimization.

The constrained MMC (cMMC) optimization follows the general form of the typical MMC optimization presented in Section 4.5, with the decision variables linked to the parameters of the

individual morphable components (Figure 4.11d). Every iteration, the minimum manufacturable thickness for each component is assessed using the constraint function described in the previous section (and shown in Figure 4.11e), and the manufacturability margin (the difference between the current and minimum thickness for each component) is computed. As the manufacturability margin of a component approaches zero, its effective density is smoothly reduced from fully dense to the minimum allowed (i.e. E_{min}; see Figure 4.11f). Each component is projected onto the density field, which is then used to define the stiffness in the FEA equations and compute the volume and sensitivity analysis as in normal MMC (Figure 4.11g), resulting in updated locations and shapes for the components at the start of the next iteration.

For example, consider the component labelled with a "Triangle" in Figure 4.11d. Each iteration, the component's orientation and length are used to place it in the manufacturability space, which assigns it a manufacturability margin based on its distance from the surface (yellow triangle in Figure 4.11e). In this case, the triangle is near the constraint surface and marginally manufacturable, so it is assigned an intermediate density, which is used when the component is projected onto the FEA element grid (Figure 4.11e). The process is repeated at every iteration.

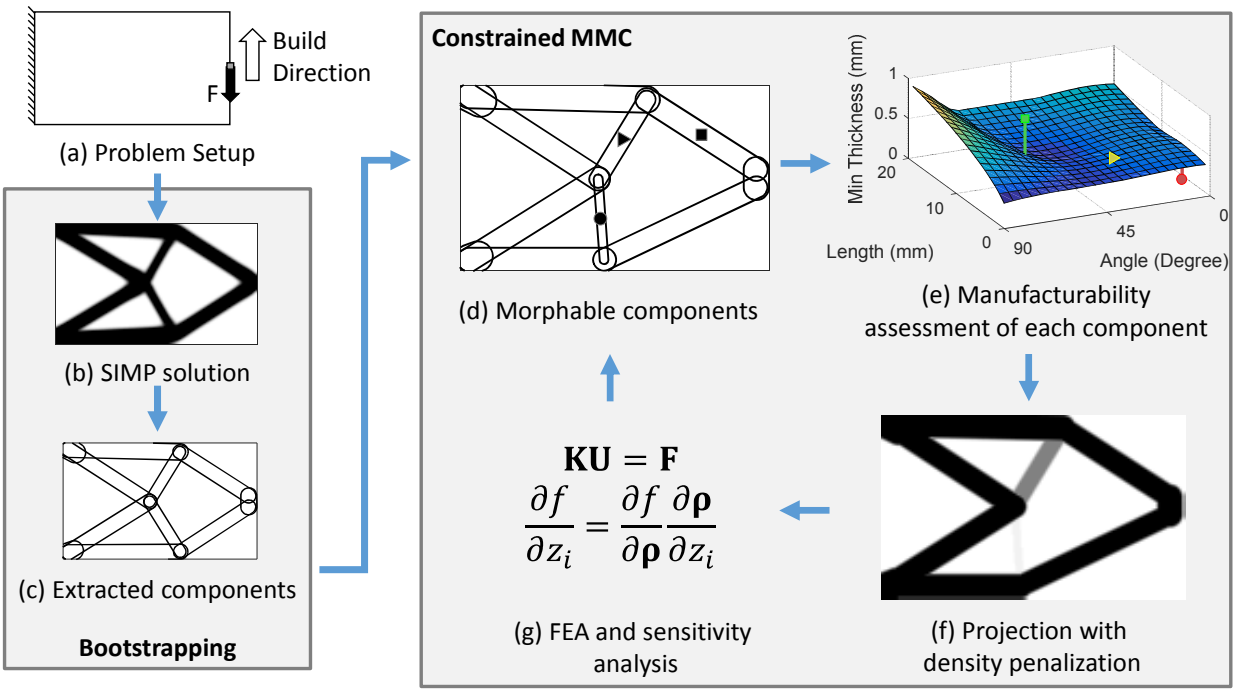

Figure 4.11. Flowchart of the bcMMC process. See text for description.

In this section, details of the constraint application to the MMC method are presented first, followed by a description of the bootstrapping process.

A. Constrained MMC

In order to support the manufacturing constraint presented in Section 4.6, the MMC framework presented above is modified in two key ways. First, the components are explicitly and inexorably connected (as in the CMC approach). Then, the penalization of effective density for unmanufacturable features is discussed. The final implementation of the approach outlined here is implemented in Matlab and follows the same rough structure as the sample code provided by W Zhang et al. (2016b).

For reasons described later, it is desirable to explicitly link the end points of each component to its neighbors. The bootstrapping process provides this information, so shared endpoints (called "junction points") are specified in the initial condition and only one (x_i, y_i) coordinate is included in the design variable vector. Unlike in the CMC approach, more than two components are allowed

to share a junction. To support this functionality, the structure of the decision variable **z** is changed from that presented in Section 4.5 to consist of a series of junction point coordinates followed by a series of component thicknesses, and a separate linkages vector **L** tracks which points are connected by a component. Specifically, let

$$\mathbf{z} = \left[x_1, y_1, x_2, y_2, \ldots x_i, y_i, \ldots, x_{np}, y_{np}, \qquad t^1, t^2, \ldots t^k \ldots, t^{nc}\right]^T$$
$$\mathbf{L} = \left[L_{kj}\right] = \begin{bmatrix} p_1^1 & p_2^1 \\ p_1^2 & p_2^2 \\ \vdots & \vdots \\ p_1^k & p_2^k \\ \vdots & \vdots \\ p_1^{nc} & p_2^{nc} \end{bmatrix} \tag{4.16}$$

where x_i, y_i represent the coordinates of the ith junction point, for each of the n_p junctions (note that junction points are no longer associated with a component using a superscript). t^k represents the thickness of component $k = 1 \ldots n_c$ for each of the n_c components. The linking matrix **L** consists of a row for each component, containing integer indexes $\left(p_1^k, p_2^k\right)$ into the list of junctions in **z** defining the two endpoints of the component, and corresponds to the kth thickness entry (which has index z_{2n_p+k}). In this way, one, two, or more components can share the same coordinates for the endpoints, forcing them to stay linked into a single chain throughout the optimization process. The optimizer cannot unlink the components in the chain.

For example, consider the connected morphing components shown in Figure 4.12, which consists of four junction points and four connected morphable components. Each junction point is listed in the decision variable **z**, followed by the thickness of each component. The linking matrix **L** provides the correspondence between components and junction points; the first row connects junction points 1 and 2 with a component of thickness t^1. Note that junction 3 is shared by three components (and hence has three entries in **L**), while junction 4 is used by only one component.

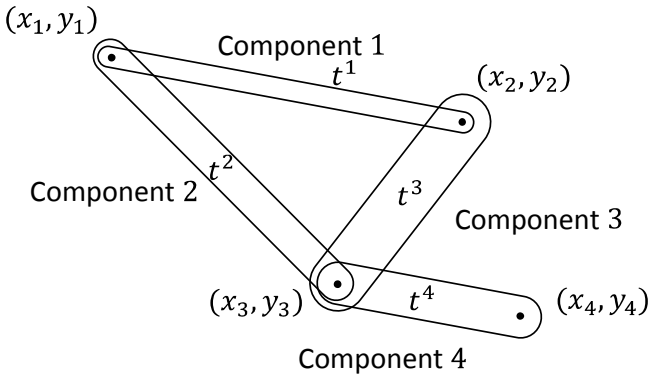

$$\mathbf{z} = [x_1, y_1, x_2, y_2, x_3, y_3, x_4, y_4, t^1, t^2, t^3, t^4]^T$$

$$\mathbf{L} = \begin{bmatrix} 1 & 2 \\ 1 & 3 \\ 2 & 3 \\ 3 & 4 \end{bmatrix}$$

Figure 4.12. Example decision variable ***z*** and linking matrix ***L*** for the set of connected morphing components shown.

Note that the linking matrix can be used to recover the parameters for an individual component $\mathbf{c}^k$ using the following construction, where the expression $z[i]$ is used here only to represent the ith element of **z**.

$$\mathbf{c}^k = \left[z[2L_{k1}], z[2L_{k1}+1], z[2L_{k2}], z[2L_{k2}+1], z[2n_p + k]\right]^T \tag{4.17}$$

The manufacturability information is integrated using a second modification to the MMC method: component density of unmanufacturable features is penalized. Penalization based on member thickness is used successfully in Norato et al. (2015), where members were pushed towards integer sizes so as to be manufacturable from readily-available stock material. They choose this method because it allows the optimizer to remove beams from the problem by exploiting the penalization, while removing components is impossible in most other MMC frameworks[9].

[9] That is, components in most MMC implementations are not removed from the domain, and topology change is achieved through component overlap; unneeded components simply move to overlay an existing, load-carrying component and therefore "disappear". This behavior is disadvantageous in the current approach because multiple overlapping components can, if untracked, violate the manufacturing requirements by combining multiple manufacturable components into a longer, unmanufacturable one.

The penalization is achieved by reducing the effective density of components as they become unmanufacturable. Because the SIMP penalization exponent is still included in the MMC formulation used (i.e. the p in Equation (4.13)), intermediate-density elements are inefficient and the optimizer is incentivized to either bring them back to full density (by thickening them or changing the angle/shape of the feature) or shrink them until they reach zero density, effectively removing them from the solution.

To reduce the density of a component, the upper bound is adjusted on the smoothed Heaviside projection filter used to convert the distance field representation of each component, ϕ, to the density field. Specifically, reduction in density is achieved by reducing the parameter η, which controls the maximum value attainable by the Heaviside function used to set the density of each node in Equation (4.11). In typical MMC approaches, η is a constant, 1, and is never even identified with a variable. Reducing η it from unity causes the entire interior of the component to become less dense (see Figure 4.13).

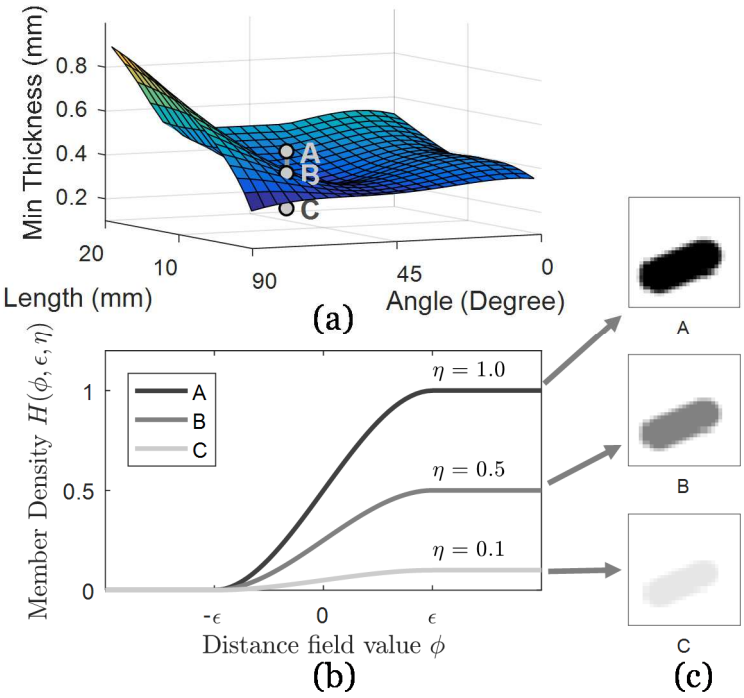

Figure 4.13. The Penalization Process. (a) The parametric manufacturability constraint surface, components above the surface are fully manufacturable. (b) Smoothed Heaviside curve for setting densities of components at each of the points A, B, and C marked in (a), with corresponding values of η. (c) The resulting feature densities.

The parameter η is set using the manufacturability margin, the difference between the current component thickness, $t^k = c_5^k$, and the minimum thickness for the member, t_{min}^k (i.e. the distance between each point in Figure 4.13a and the constraint surface; see Equation (4.15) for the definition of t_{min}^k). Mathematically, the relationship can be stated with a second use of the smoothed Heaviside function,

$$\eta \Rightarrow \eta^k = \eta(\mathbf{c}^k) = H\left(t^k - t_{min}^k, \gamma, 1\right) \tag{4.18}$$

this time with a different regularization (smoothing) parameter, γ, which controls how close to the minimum manufacturable diameter the penalty begins to take effect. Note that this is a different tuning parameter than smoothing of the density projection Heaviside filter (ϵ). The upper limit for the Heaviside function in Equation (4.18) is explicitly set to 1.0 (fully dense). As a result, the expression for the density projection operation, formerly Equation (4.11), becomes

$$D(\mathbf{P},\mathbf{z}) = \max_{k=1..n_c} H\left(\phi\left(\mathbf{P},\mathbf{c}^k\right),\epsilon,\eta(\mathbf{c}^k)\right) \quad (4.19)$$
$$\eta(\mathbf{c}^k) = H\left(t^k - t_{min}(\mathbf{c}^k),\gamma,1\right) \quad \text{supplanted by (4.21)}$$

Note that Equation (4.19) will be replaced by yet another version later in this section.

If derivatives were directly calculated, the introduction of the dependence of η^k on the independent variable **z** (through the convenience variable **c**) would require a more complex expression for the back-projection derivative term, $\partial\rho_e/\partial z_i$, but the use of numeric approximate derivatives in this implementation automatically accounts for this interdependency.

The above approach handles manufacturability constraints for individual components. However, MMC solutions often result in overlapping elements which combine to create a larger effective feature. As a result, if longer features require larger minimum diameters to be manufacturable (as they do in the current manufacturability constraint function), two shorter features could each be manufacturable but join end to end to create an unmanufacturable result. For this reason, components are explicitly joined at the endpoints in the bcMMC approach during the bootstrapping phase. This enables groups of connected features to be evaluated for manufacturability both individually and as a unit. Note that actually, overlapping components which combine to form a thicker (rather than longer) effective feature are of no concern to the method – thicker features are by definition more manufacturable.

For this development, let a *chain* of components be a series of components linked end-to-end by only 2-junctions (that is, each junction connects only two members; see Figure 4.14a). To prevent chains from forming unmanufacturable features, the entire chain is combined into an *equivalent feature* which is also evaluated for manufacturability. Equivalent features are defined by taking the average thickness, the average angle from the build platform, and the sum of the lengths of the components of the chain. Let

$$
\begin{aligned}
l^{eq}(\mathbf{z},k) &= \sum_{j\in Ch(k)} l\left(\mathbf{c}^j\right) \\
\theta^{eq}(\mathbf{z},k) &= \frac{1}{|Ch(k)|}\sum_{j\in Ch(k)} \theta\left(\mathbf{c}^j\right) \\
t^{eq}(\mathbf{z},k) &= \frac{1}{|Ch(k)|}\sum_{j\in Ch(k)} t^j \\
t^{eq}_{min}(\mathbf{z},k) &= \tfrac{1}{2}S(l^{eq}(\mathbf{z},k),\theta^{eq}(\mathbf{z},k)) \\
\eta^{eq}(\mathbf{z},k) &= H\left(t^{eq}(\mathbf{z},k) - t^{eq}_{min}(\mathbf{z},k),\gamma,1\right)
\end{aligned}
\qquad (4.20)[10]
$$

where the function $Ch(k)$ returns the vector of component indices in the chain containing component k, and $|Ch(k)|$ denotes the number of elements in the vector.

Penalizing feature chains is a heuristic way to check manufacturability for a series of components connected together, especially for curved features, but no experimental data on curved features has been collected[11]. The effective penalty ($\bar{\eta}^k$) for each individual component in a chain is the lower of the entire chain's equivalent feature and the lowest penalty among the chain's components (see Figure 4.14b). Formally, the density projection D is redefined one more time as

$$
\begin{aligned}
D(\mathbf{P},\mathbf{z}) &= \max_{k=1..n_c} H\left(\phi\left(\mathbf{P},\mathbf{c}^k\right),\epsilon,\bar{\eta}(\mathbf{z},k)\right) \\
\bar{\eta}(\mathbf{z},k) &= \bar{\eta}^k = \min\left(\min_{i\in Ch(k)} \eta(\mathbf{c}^i), \eta^{eq}(\mathbf{z},k)\right)
\end{aligned}
\qquad (4.21)
$$

This construction causes entire chains to be removed all at once from the design space, preventing dangling components which are not supported and could potentially form thin "hinge" connections with other components or otherwise produce unmanufacturable effects.

[10] Note that taking the sum of the lengths of the components is conservative because the ends of successive components overlap.

[11] And, in the author's experience, curved features appear fairly infrequently in topology optimization results, at least in mechanics problems

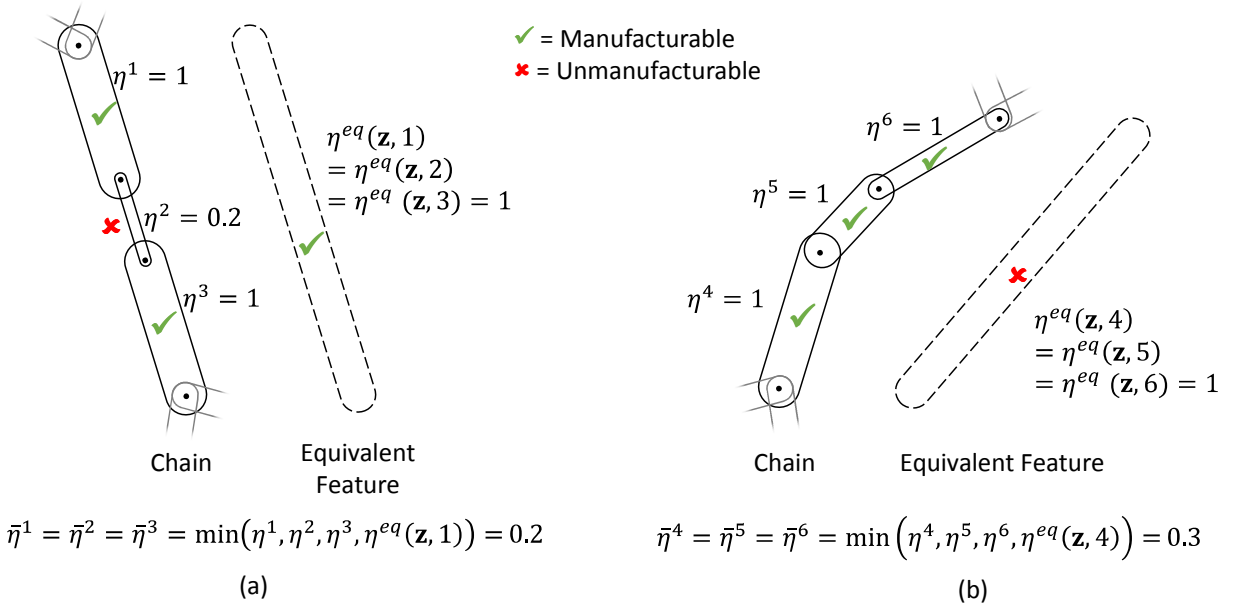

Figure 4.14. Chained components example. (a) An individual component in a chain is not manufacturable, penalizing all members of the chain. (b) The equivalent feature for the chain is not manufacturable, penalizing all members of the chain.

To avoid the premature removal of elements from the design, a continuation approach is utilized during the first 40-80 iterations of the cMMC portion of the bcMMC solution, in which γ is gradually decreased from a larger value down to the final one. The number of iterations to use for continuation was selected by trial-and-error, observing over a variety of test problems how the cMMC algorithm behaved with varying durations of continuation. In the next section, the parameter γ is defined as a fraction of the maximum domain dimension, and decreased from $\gamma_0 = 0.1\max(w_d, h_d)$ to $\gamma_f = 0.008\max(w_d, h_d)$ where w_d and h_d are the domain width and height, respectively, over 60 iterations. This provides a softened penalty ensuring features with initial configurations which are unmanufacturable are not immediately removed from the design and gives the optimizer time to thicken them.

To avoid the optimizer "cheating" the volume constraint by placing part of a component outside the analysis domain, the locations of the junction points are constrained to remain within the middle 90% of the domain in the X and Y directions, except on edges with symmetry boundary conditions. Because features can generally be produced without concern on the build plate,

junction points are also allowed to move all the way to that edge as well. This *Endpoint Keep-out Zone* works to keep all components inside the domain, so that the FEA, volume constraint, and manufacturability assessment can see (almost) all of each component. See Figure 4.15 for a visual explanation. In Figure 4.15a, the component shown can move more than half of its volume outside the design domain, allowing it to become larger (and therefore more likely to be manufacturable) without experiencing the penalty of the volume constraint. In Figure 4.15b, the endpoint keep-out zone ensures most of the component remains inside the domain, except at a line of symmetry, where the other part of the component will appear in the other half of the design, and near the build plate, at which it is assumed the manufacturing process can more easily produce small features.

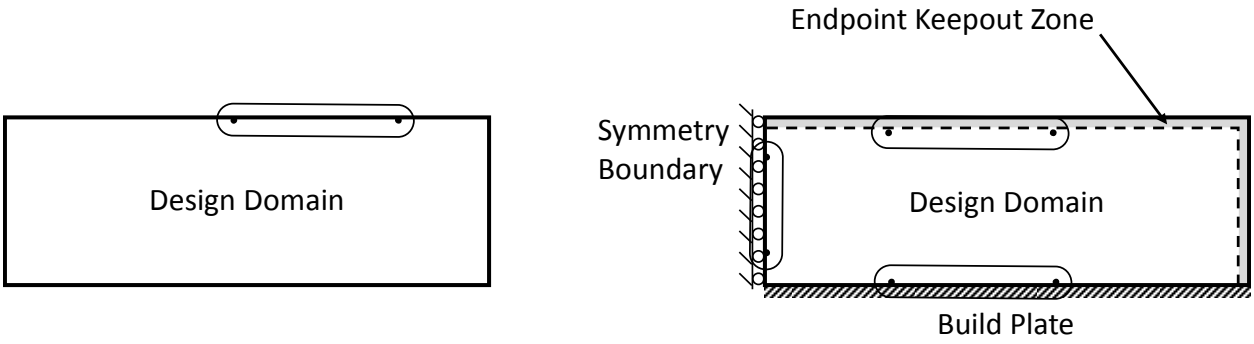

Figure 4.15. Example illustrating the need for endpoint keep-out zone, which is generally a band occupying the last 5% of each side of the domain into which junction points are not allowed to move. In (a), the optimizer can move the component endpoints all the way to the edge of the domain, allowing it to grow the feature significantly and "hide" half of the volume from the volume constraint. In (b), an endpoint keep-out zone prevents this behavior.

B. Bootstrapping Approach

In this section, the bootstrapping approach used to provide the cMMC method with an intelligent and connected initial component configuration is detailed.

First, the SIMP algorithm is run to provide a preliminary density solution to the optimization problem, using the top110 code from Andreassen et al. (2011). The SIMP algorithm can accommodate a single minimum feature size, which is specified to be smaller than the smallest

producible feature in the constraint function. SIMP is selected because it quickly converges from gray initial conditions to near-local-optimum topologies, and has a mature, well-studied theoretical basis. Because SIMP cannot easily accommodate the feature-dependent feature size constraint which is the object of the present study, after a specified number of iterations, the design is transferred ("bootstrapped") into the cMMC framework presented above, and optimization continues in the context of feature-driven design rules. A bootstrapping approach for the MMC formulation such as this has not been found in the literature. The advantage of this approach is dramatically improved convergence to stable equilibria, at the expense of a narrowing of the search space by starting cMMC out near a local minimum. Even though the initial topology is set with the SIMP approach, the cMMC algorithm can still effect topology changes by removing members which it deems inefficient in light of the manufacturing constraints.

The procedure for extracting the morphable components from the SIMP density field follows in the spirit of Bremicker et al. (1991), which used the shape skeleton as a means to extract the beam elements in a SIMP solution. The present approach is described briefly in this section, and the reader is encouraged to follow along in Figure 4.16 and Figure 4.17 for an example.

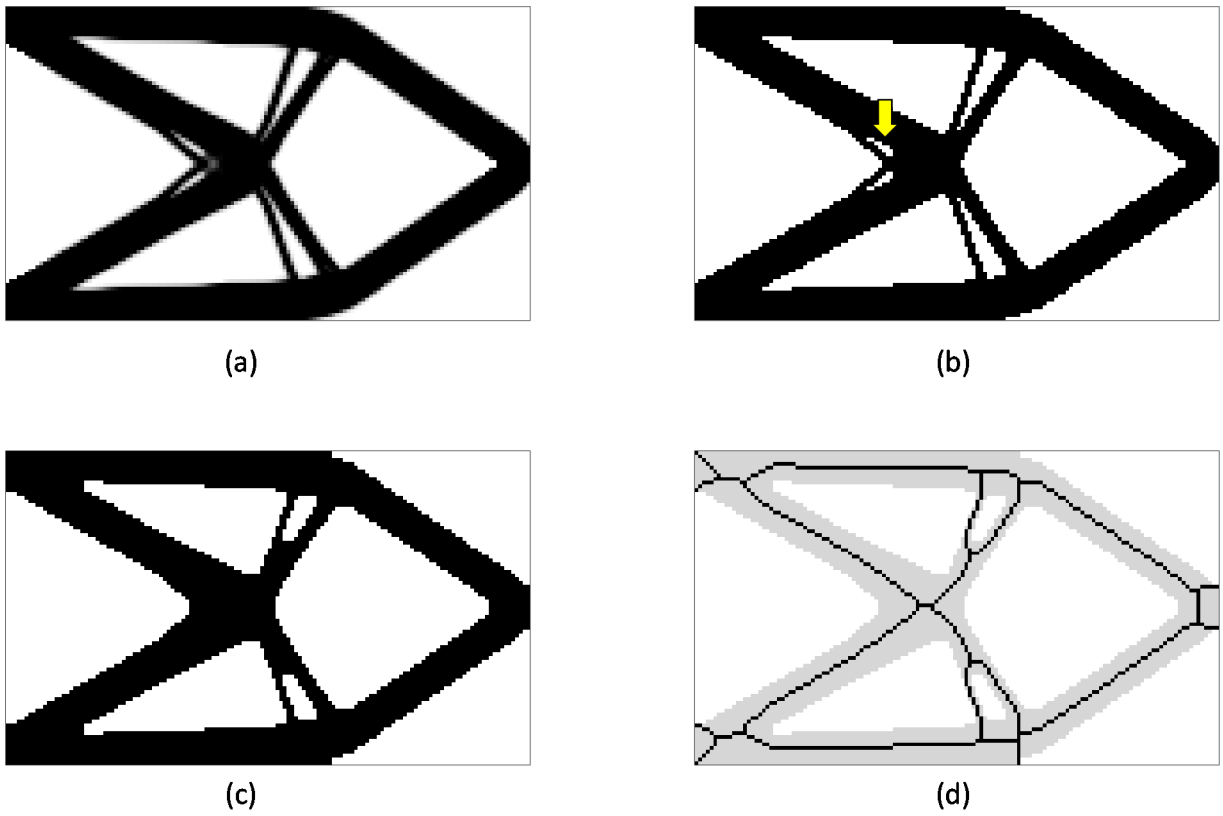

Figure 4.16. Bootstrapping Procedure, Part 1. (a) Input SIMP density field (b) Thresholded field (c) Morphological closing of the thresholded field (d) shape skeleton transform of the result (gray background replicates (c) for reference).

To prepare for topology extraction, the density field is first preprocessed. SIMP creates a continuous density field (Figure 4.16a), and a threshold is applied to obtain a pure black-and-white design (Figure 4.16b). Next, a morphological closing is performed (Figure 4.16c), which eliminates small holes in the domain. Note that the two very small holes near the center of the domain have been removed (see arrow in Figure 4.16b). Experimental evidence suggests that small holes consisting of only a few FEA elements produce large numbers of morphable components and do not contribute to the quality of the optimized design.

The shape skeleton is then computed using the Matlab function `bwmorph` (Figure 4.16d). By design, the shape skeleton preserves the topology of the input, but converts all members to single-pixel-wide features. The junction points in the skeleton, where two or more skeletal

branches come together, are extracted, along with the distance to the boundary at each skeletal point (using the `bwmorph` and `bwdist` Matlab functions).

The skeleton is used as a map to extract the connectivity between the junction points, and the distance of each skeletal point to the boundary is averaged over each segment to set the initial thickness (Figure 4.17a). The connections between the junction points are shown as straight lines, and each corresponds to the centerline of a single morphable cMMC component. Segments which are very short (length less than a pre-determined threshold, l_{min}) are removed and nearby junction points merged.

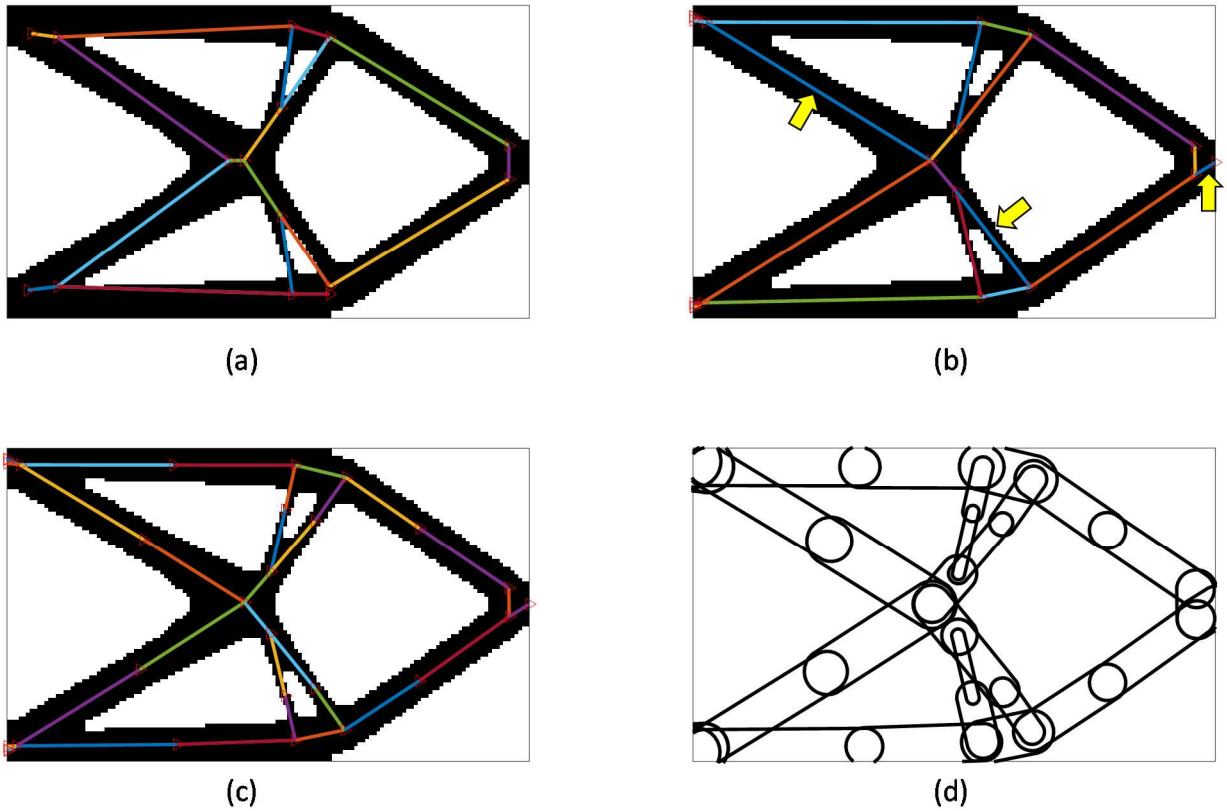

Figure 4.17. Bootstrapping Procedure, Part 2. (a) Connected graph of skeleton junction points (b) Optimized junction point locations (c) Subdivided skeletal segments (d) Segments converted into linked morphable components.

The linear connecting segments retain the topology of the skeleton, but because the original skeletal segments are curved, the lines do not necessarily closely follow the shape of the input

design. To improve the accuracy of the results, a small optimization is performed, in which the locations of all junction points are moved so as to minimize the deviation of the linear segments from the center lines of the features in the density field (Figure 4.17b). For example, note the two segments indicated by the diagonal arrows in Figure 4.17b, which did not previously follow the density field features. Again, nearby junction points are merged, and short segments are removed. In addition, new component segments are added to connect the skeleton to each of the load or support points in the problem setup, ensuring the design does not become disconnected from the boundaries during optimization (see right-most, vertical arrow in Figure 4.17b)

To provide the MMC optimizer with additional flexibility in determining the shape and structure of the final design, long segments (i.e. those with length greater than $5l_{min}$) are divided in half, with a new junction point inserted at the midpoint (Figure 4.17c). Each of these junction points becomes a junction in the cMMC connected component layout, and the connecting segments define component links between them, with initial thicknesses set according to the average distance from the boundary of the SIMP field (Figure 4.17d).

To further ensure the MMC optimizer is provided with a good starting condition, in a final step the thicknesses of all components are scaled so the entire structure meets the volume constraint of the problem definition, accounting for any volume change incurred in the bootstrapping process.

4.8 RESULTS

In this section, some preliminary results obtained using the approach described above are presented. First, validation/characterization studies are reported for the bcMMC approach with no manufacturability penalization (just bootstrapping), followed by several examples demonstrating the value of the feature-driven penalties for manufacturability. For all problems in this section, parameters for the solvers are set according to Table 4.4, unless otherwise stated. The optimizer used is the Method of Moving Asymptotes algorithm by Svanberg (1987); SIMP results

are generated using the code by Andreassen et al. (2011). Slight modifications to each code are required, and details are given in Appendix E.

Table 4.4. Default parameter settings used in generating the results.

Parameter	**Value**	**Note**
Young's Modulus E	1	As in Andreassen et. al (2011) and elsewhere
Poisson's Ratio ν	0.3	
Intermediate Density Penalty p	3	Literature recommendation (Sigmund and Maute, 2013)
Solid Density	1	
Void Density	10^{-9}	For both SIMP and MMC FEA analyses
Heaviside regularization for density ϵ	$0.5w_e$	Where w_e is the width of an FEA element
Final Heaviside regularization for manufacturability penalty γ_f	$0.008w_d$	Where w_d is the domain width
Initial Heaviside regularization for manufacturability penalty γ_0	$0.1w_d$	
Number of steps used in the continuation scheme for γ	60	
MMC Derivative step size, x and y	$2w_e$	
MMC Derivative step size, t	$0.2w_e$	
l_{min} used for bootstrapping	0.1 mm	Minimum component length during bootstrapping before merging

A. Bootstrapped cMMC and the Effect on Convergence

One goal of the bootstrapping approach for the cMMC method presented in this paper is to improve the speed of convergence of the algorithm by providing an initial configuration near a local minimum. To evaluate the approach's effectiveness, a problem using the design domain shown in Figure 4.18a was solved using three configurations: Using only SIMP, using only the

cMMC framework with a set of initially disconnected bars shown in Figure 4.18b, and using the proposed boostrapping technique. For this problem, the 2:1 domain is discretized into 160x80 finite elements, the volume fraction is constrained to 0.4, the SIMP solution utilized is the projection filter from Guest et al. (2004), with filter size of 2.4 elements. The minimum element thickness for the (b)cMMC simulations is also set to 2.4 element widths. Component endpoints were allowed to move freely anywhere within the design domain (no keep-out zone). The non-bootstrapped cMMC study does not chain members and utilizes the same initial configuration as W Zhang et al. (2016b), and the bootstrapped MMC solution does link members by connecting multiple component endpoints to the same optimization variable. No manufacturability penalties are applied in this problem.

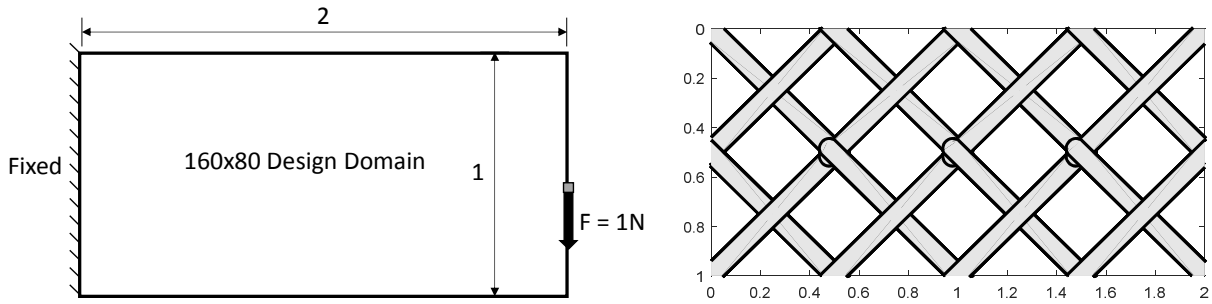

(a) (b)

Figure 4.18. (a) Design domain, loads, and constraints for the Bootstrapping Test Problem. (b) The initial (unconnected) component distribution for the non-bootstrapped cMMC solution to this problem.

Summary results are shown in Table 4.5, and an iteration history plot is shown in Figure 4.19. The SIMP result shows excellent initial convergence to a reasonably-low objective function value, then slow, steady downward movement. The non-bootstrapped MMC solution converges very slowly due to the need to move each individual component into position, but ultimately converges to an objective function value 5.4% higher than SIMP, achieving a visually-similar topology. The bootstrapped approach leveraged 50 iterations of the SIMP solution, then after starting the MMC optimization a few iterations of higher objective value are seen as the optimizer adjusts for irregularities introduced by the component extraction, but then converges quickly to a

topology similar to that produced by SIMP and an objective function value only about 1.6% higher than SIMP. The SIMP approach was not checked for convergence, to see the full effect of the continuation scheme from the projection filter. The non-bootstrapped approach did not converge in the 400 iteration limit, while the bootstrapped approach converged after only 146 iterations of the cMMC (for 196 iterations total). Note that the "bcMMC Bootstrapped" convergence plot in Figure 4.19 exactly overlaps the SIMP solution for the first 50 iterations.

Even though less flexible component primitives and a slightly different density projection are utilized in the non-bootstrapped MMC implementation here than those used in W Zhang et al. (2016b), similar resulting shapes are obtained in the MMC row of Table 4.5 and for the same problem in their work (see W Zhang et al. Table 2). Nevertheless, the value of the objective function they obtain is 0.5% better than the SIMP solution here (74.52-74.66 compared to the SIMP solution here of 74.88), suggesting that with additional adjustments, the bootstrapped MMC formulation could be made to be comparably efficient to the traditional SIMP solution.

Table 4.5. Bootstrapping test results. Compliance reported is for thresholded density field. Compare to literature reported values for this problem using non-bootstrapped MMC of 74.52-74.66 (W. Zhang et al., 2016b)

Solver	Conditions	Output Density Field	Output Component Plot
SIMP	$r_{min} = 2.4$ elements	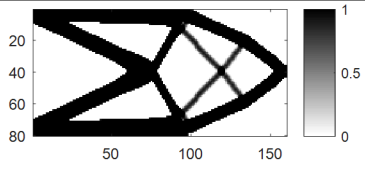 400 iterations, $\bar{f} = 74.88$	
Non-bootstrapped MMC	No manufacturing penalty 16 unlinked components Minimum t of 2.4 elements No keepout zone	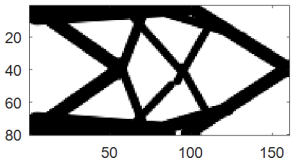 400 iterations, $\bar{f} = 78.97$	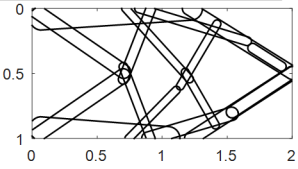
Bootstrapped bcMMC	No manufacturing penalty 50 Iteration SIMP bootstrap $l_{min} = 2.4$ elements	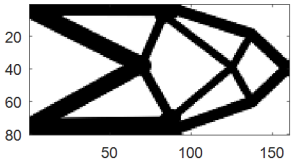 50 SIMP + 146 bcMMC iterations, $\bar{f} = 76.14$	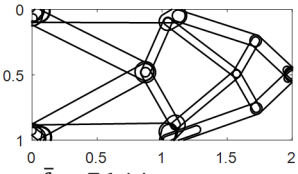

To quantitatively assess the differences in convergence, the number of iterations required for thresholded compliance to drop and remain below 80 is considered (see dashed line in Figure 4.19). The bcMMC solution reaches this threshold in only 70 iterations, which though worse than SIMP shows a 72% improvement over non-bootstrapped MMC.

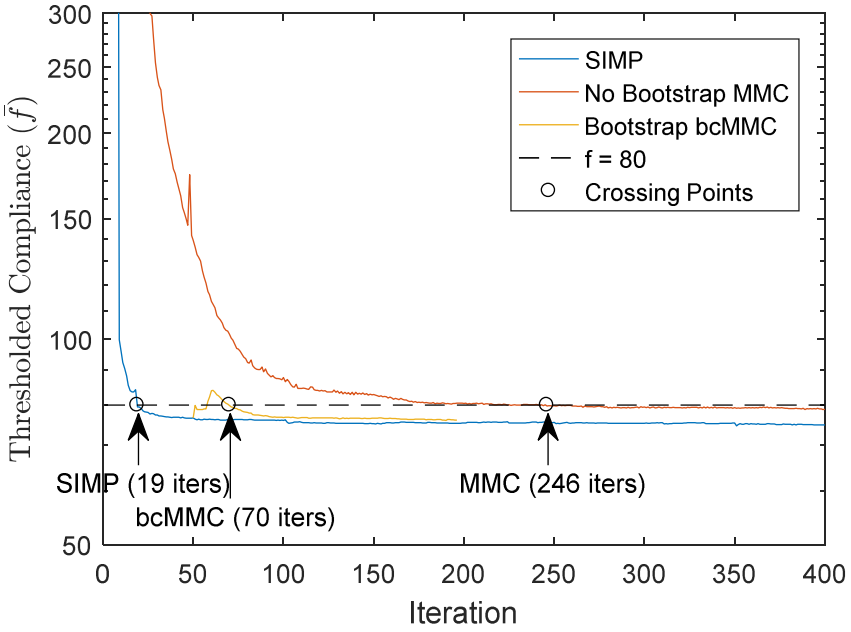

Figure 4.19. Bootstrapping test convergence history; vertical axis is thresholded compliance. Lower values are better.

B. Mesh Independence Study

To validate that the bootstrapped MMC approach is independent of mesh resolution, a mesh refinement study was performed. The design domain used is shown in Figure 4.20, and discretized into various numbers of FEA elements. Manufacturability constraints are again disabled, and component endpoints are allowed to freely move within the domain. The SIMP implementation used for bootstrapping utilizes a density filter (as in Equation (4.9)), because the projection filter used elsewhere in this paper does present some degree of mesh-dependence. The SIMP filter size and MMC minimum member half-thickness are set at 1.5% of the domain width, irrespective of grid resolution. No minimum component thickness is required of the MMC solution. The volume fraction was set to 0.5. The SIMP algorithm was run for 50 iterations in each case, and the MMC code allowed to run until convergence, or 200 iterations, whichever came first.

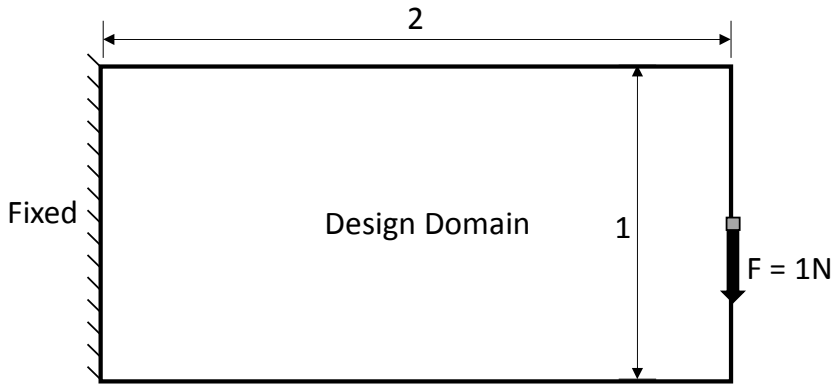

Figure 4.20. Problem setup for Mesh Independence Study

The resulting density field and component map is shown in Table 4.6. In each case, the SIMP fields look nearly identical, and the bcMMC field changes it very little (as expected, since the bcMMC problem setup has no additional constraints). In both coarser cases, the final value of the objective function is within 0.2% of the finest resolution. Histories of the objective function value and the constraint function value are shown in Figure 4.21. Note that the first 50 iterations of each plot correspond to the SIMP solution, and the remainder is the cMMC algorithm. Because of the construction of the optimality criteria optimizer used in the SIMP code, the volume constraint is automatically satisfied. In all three cases, the behavior is similar. For the few iterations just after bootstrapping, the compliance value becomes somewhat large as the design corrects the non-optimality introduced by the bootstrapping.

Table 4.6. Mesh independence study density and component plots. Percentages represent the difference in compliance of the thresholded design with respect to the Fine case

FEA Mesh	Bootstrap Initial Layout	bcMMC Component Plot	bcMMC Density Plot
Coarse 120x72	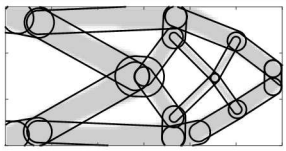	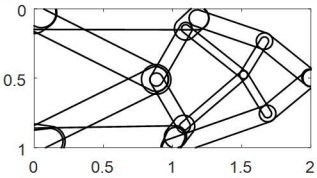	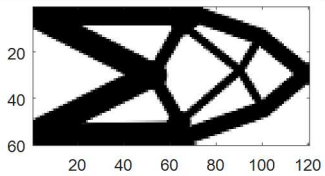
		50+192 iterations, $\bar{f} = 62.342$ $(+0.2\%)$	
Medium 160x96	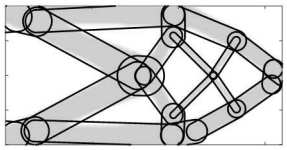	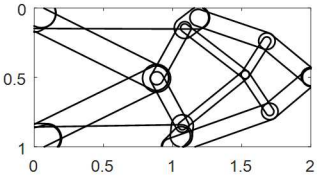	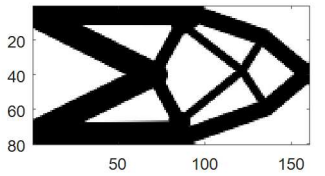
		50+200 iterations, $\bar{f} = 62.121$ (-0.1%)	
Fine 200x120	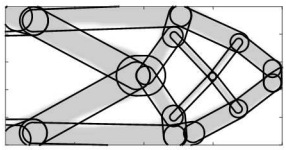	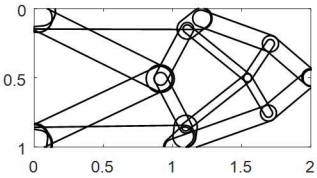	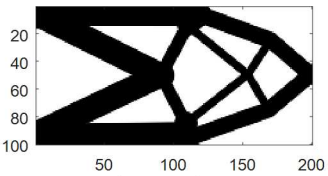
		50+200 iterations, $\bar{f} = 62.192$ $(\equiv 0\%)$	

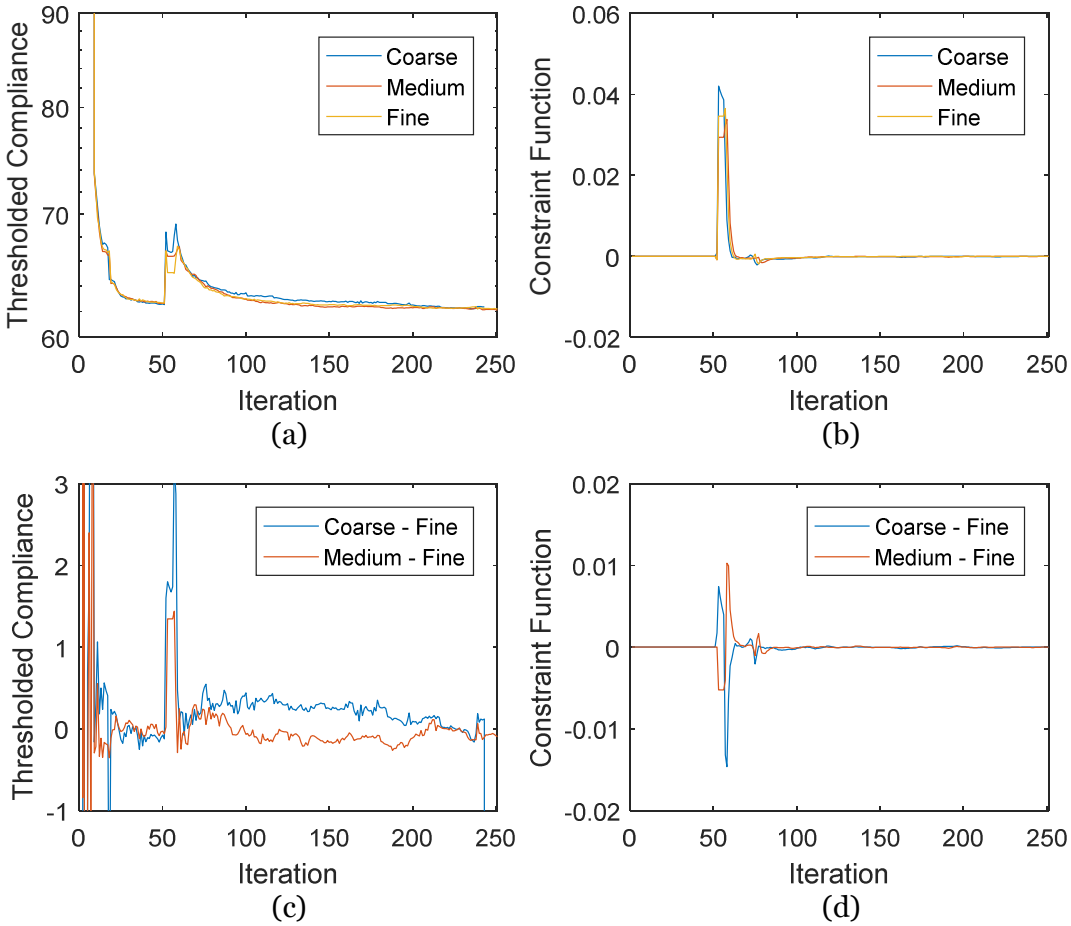

Figure 4.21. Mesh independence study objective function history (a), and constraint function history (b). Differences between coarse, medium, and fine resolution for each case shown in (c) and (d).

The mesh independence study provides an opportunity to examine the speed and complexity of the proposed algorithms, and a summary is shown in Table 4.7. Both the derivative computation time and the FEA time grow roughly linearly with the number of FEA elements. The derivative computation has a significant overhead and is also expected to grow linearly in the number of MMC components present (see Figure 4.22).

Table 4.7. Timings for mesh independence study. Data taken on a 2.3 GHz Intel Core i7-3610QM with 16 GB of ram running Windows 10 and Matlab R2016b.

Case	Total Time (sec)			Time/MMC Iteration (ms)			
	SIMP	Bootstrap	MMC	Projection	Derivatives	FEA	Other
Coarse	9.2	6.3	151.5	26	512	130	89
Medium	15.3	8.1	206.6	40	651	248	95
Fine	23.9	10.4	173.5	58	901	413	98

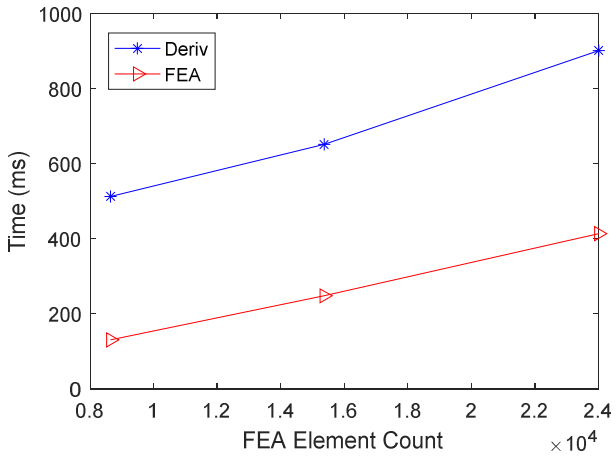

Figure 4.22. Time per iteration for the derivative computation vs. the number of FEA elements used in the mesh independence study.

C. The Short Beam Problem

After validating the efficacy and mesh independence of the bcMMC approach, several examples present the impact of imposing feature-dependent minimum size constraints for manufacturability. First, the short beam problem is considered, as shown in Figure 4.23. The 200x100 FEA domain has dimensions 40 mm by 20 mm, and the build plate is initially placed on the lower edge, as shown in Figure 4.23b. The bootstrapping SIMP algorithm again uses the Heaviside projection filter of Guest et al. (2004). Manufacturability constraints are active, including bridging data, with 60 iterations of continuation on the penalty regularization parameter γ, and component endpoints are restricted from the right and top edges of the design domain as shown in Figure 4.23b. The SIMP filter size is set to 0.3 mm (to create 0.6mm thickness features), which is just less than the smallest manufacturable feature size. The volume fraction is

set to 50%. The SIMP algorithm is run for 50 iterations in each case, and the MMC code allowed to run until convergence up to 200 iterations.

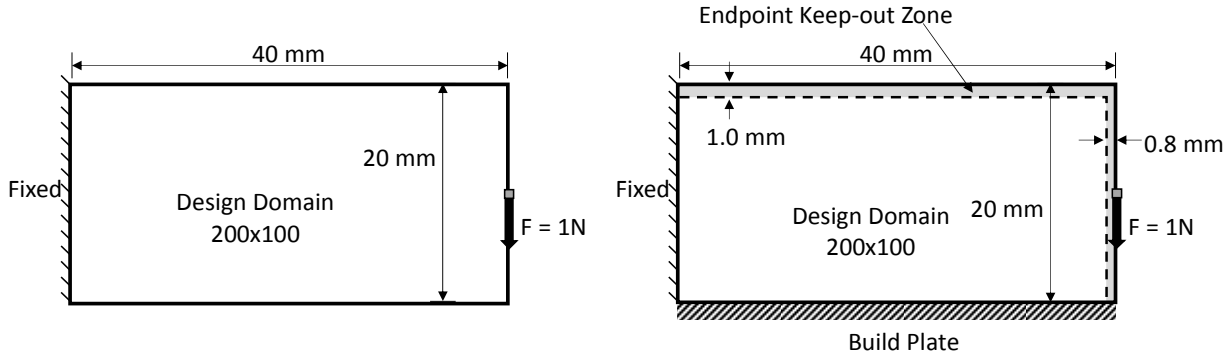

(a) (b)

Figure 4.23. Domain setup for the short beam problem. (a) SIMP domain (b) MMC domain with additional details for manufacturing constraints.

Results for the bootstrapping of the short beam problem is shown in Figure 4.24. After 50 iterations, the SIMP code produces geometry with fine details (Figure 4.24a), but some are lost in the bootstrapping process and do not show up as components in Figure 4.24b, which shows the initial component layout for all of the cMMC solutions in this section with $V_f = 0.5$. Figure 4.24c shows a reference solution using SIMP on a refined grid with r_{min} set to produce members with a minimum diameter of 1.0mm, which should be manufacturable on the selected material extrusion process (without considering overhang).

Figure 4.25 show the bcMMC layouts and density fields for two different build directions. In both cases, the manufacturability penalty is applied (bridging data included; see Figure 4.9b). In the top row, the build direction is as shown in Figure 4.23b. All of the small features present in the SIMP design are retained, though some are reshaped, resulting in a thresholded compliance of $\bar{f} = 62.39$, which is 1.2% higher than the reference SIMP solution. Even though many overhanging members exist in this configuration, they all lie above the experimentally-determined minimum feature diameter for their respective orientations.

In the second row of Figure 4.25, the same problem is solved, but with the build direction rotated 90°. In this configuration, the vertical and diagonal members require much less overhang,

except for two nearly-horizontal components (see arrows) which have been removed as inefficient by the optimizer by penalizing so that the effective density is zero. The objective function value for this case, $\bar{f} = 62.55$, lags the SIMP solution by 1.45%. The central large features in this design show some asymmetry, though the problem should be entirely symmetric. This is due to differences in the way the bootstrapping method selected and connected junction points, and is a clear shortcoming of this approach.

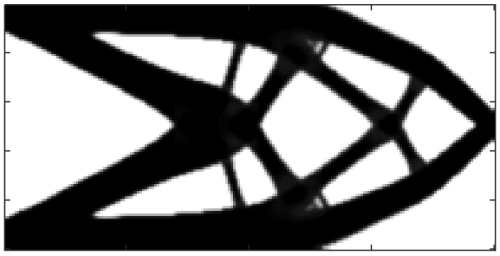

SIMP, 50 Iterations, $\bar{f} = 63.4$
(a)

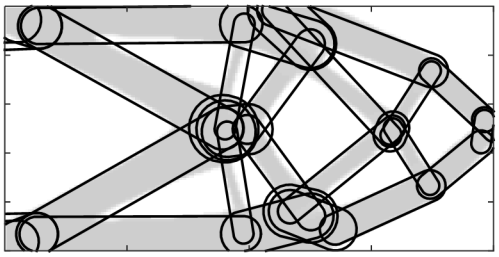

Extracted Components
(b)

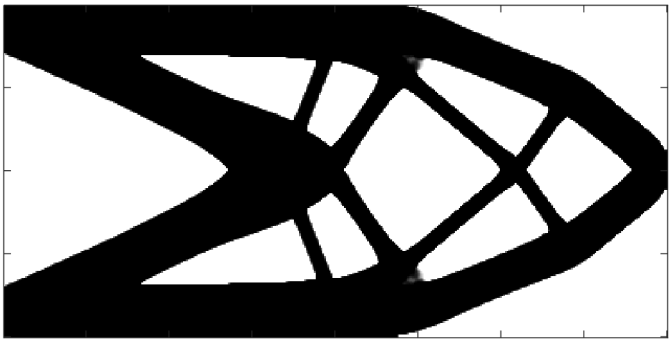

SIMP, 400x200 domain, $r_{min} = 0.5\ mm$, 400 Iterations, $f = 61.65$
(c)

Figure 4.24. Bootstrapping for the short beam problem, $V_f = 0.5$. (a) SIMP solution after 50 iterations. (b) Extracted initial component layout. (c) Reference SIMP solution with manufacturable, 1.0 mm feature size, after 400 iterations.

Solver	Conditions	Output Component Plot	Output Density Field
bcMMC	Build direction 0° $V_f = 0.5$	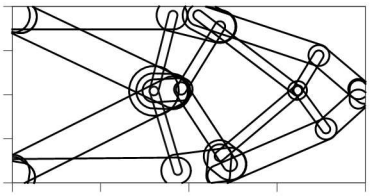	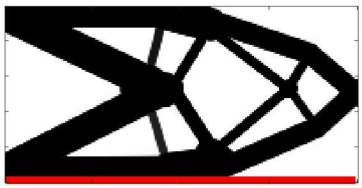
	50+200 iterations, $\bar{f} = 62.39$ (+1.2%)		
bcMMC	Build direction 90° $V_f = 0.5$	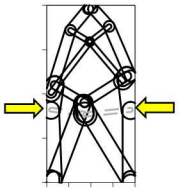	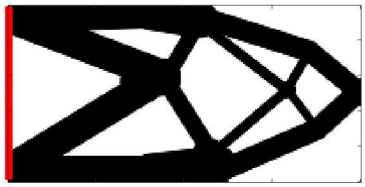
	50+200 iterations, $\bar{f} = 62.55$ (+1.5%)		

Figure 4.25. Short Beam results for two orientations. The red line in the output density field indicates the build platform.

Different topologies are obtained as the volume fraction is varied. Figure 4.26 shows three other solutions for different volume fractions in the vertical manufacturing orientation. Generally, the output topology is similar to that present at bootstrapping, with small members removed or rearranged. In the 15% case, all of the diagonal members in the structure are just above the manufacturability constraint surface, resulting in slight penalization of the component densities (note the lighter shade of the components in the density map for the 15% case). When computing the thresholded compliance, $\bar{f}$, the threshold value which maintains the volume constraint removes entirely one of the diagonal elements (see the arrow in the bottom row of Figure 4.26), resulting in a very large compliance value. The objective function value for this case, in which the gray elements are penalized instead of thresholded, is only 317.

Volume Fraction	Bootstrap Initial Layout	bcMMC Components	bcMMC Density
40%	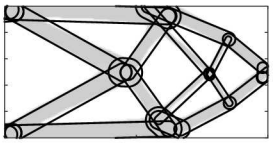	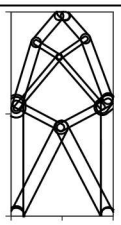	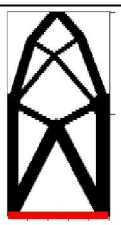
		50+200 iterations, $\bar{f} = 75.25$	
25%	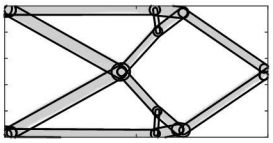	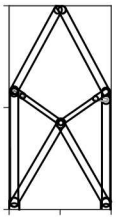	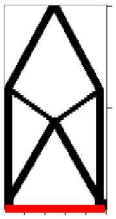
		50+200 iterations, $\bar{f} = 116.85$	
15%	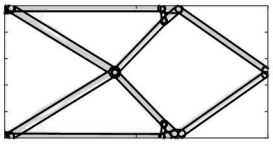	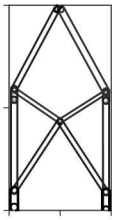	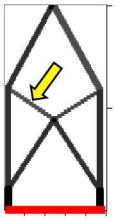
		50+118 iterations, $\bar{f} = 1260.3$	

Figure 4.26. Short beam problem for various volume fractions.

For a 50% volume fraction case, three models were manufactured. An “aggressive” SIMP solution uses the minimum feature size of 0.71 mm suggested by Stratasys for a similar FDM manufacturing process (“Design Guidelines: Fused Deposition Modeling (FDM),” n.d.). This is only a reasonable minimum diameter for short features which have little overhang. This SIMP design is shown in Figure 4.27a. A “conservative” SIMP model uses the minimum feature size of 1.0 mm suggested by Materialse, m.v. in their design guidelines (Materialise mv, n.d.). This provides a safe thickness for all small overhang angles, and the corresponding design is shown in Figure 4.27b. Finally, the bootstrapped MMC optimized design for the vertical orientation is manufactured (same as the bottom row in Figure 4.25), shown again in Figure 4.27c. Models were generated with a fixed depth of 4mm mm, and a small plate was attached to the bottom to ensure

good connection with the platform. All three designs are produced acceptably, though the nearly horizontal bars show some surface finish deterioration in the SIMP cases. The bcMMC solution removes these features as unmanufacturable and is produced nicely.

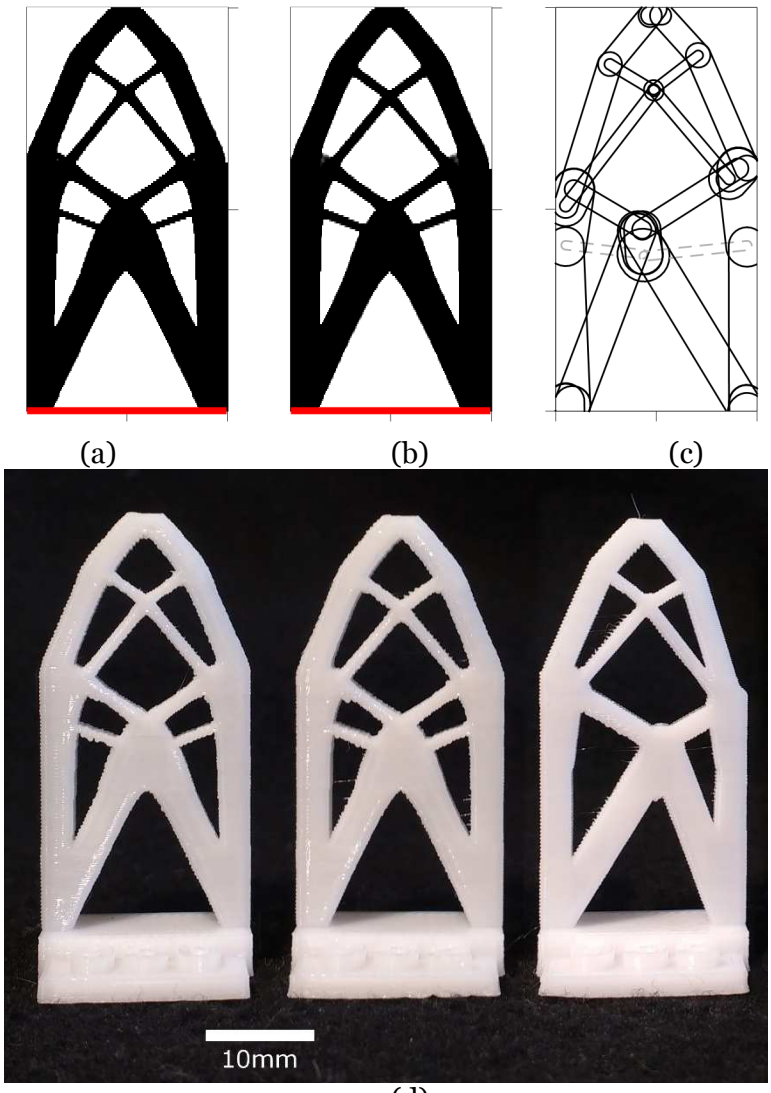

Figure 4.27. Three manufactured SIMP designs. (a) SIMP, minimum diameter of 0.71mm, (b) SIMP, minimum thickness of 1.0mm, (c) Bootstrapped MMC with manufacturable minimum thickness. (d) Manufactured form of each of the above.

Finally, some intermediate steps of the optimization process are shown for the original 50% volume fraction bootstrapped MMC case (as seen in the first row of Figure 4.25) are presented in Figure 4.28. The MMC process makes slow, gradual changes to the shape and topology of the

structure. Because the bootstrapping provides a performant solution from the start, less dramatic changes are needed than in other MMC procedures.

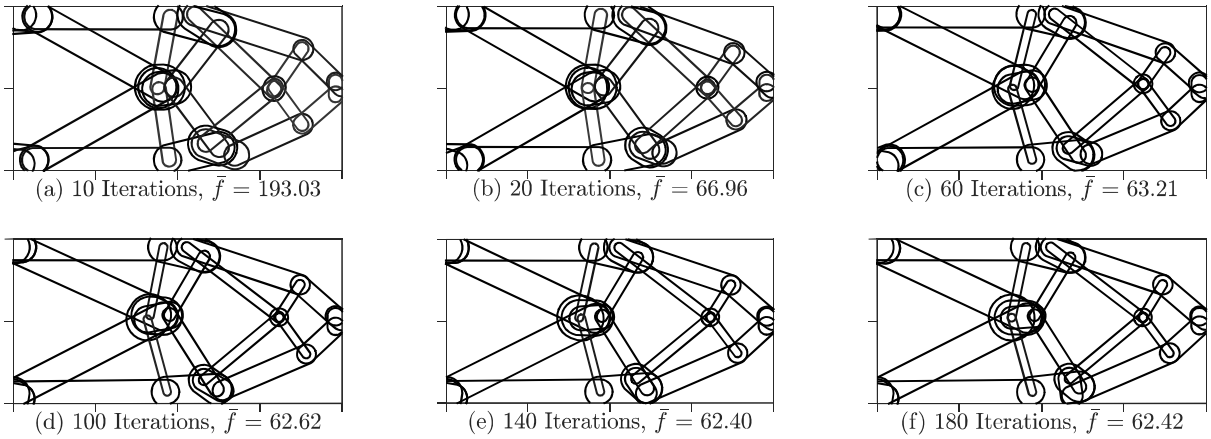

Figure 4.28. Intermediate steps of the MMC solution for a short beam; horizontal build orientation, 50% dense, bridging manufacturing constraints. Iteration numbers indicate iterations after bootstrapping.

D. The MBB Beam Problem

A second example problem is the well-known Messerschmitt-Blölkw-Blohm (MBB) beam problem[12]. The domain is shown in Figure 4.29a, and represents a half of a bridge-like structure; the complete geometry is created by mirroring about the left side of the domain. The 225x75 FEA domain has dimensions 45mm by 15 mm (3:1), and the build plate is initially placed on the lower edge, as shown in Figure 4.29b. The SIMP implementation used for bootstrapping uses a p-continuation approach to resolve the more intricate microstructure in the center of the domain by incrementing p from 1.0 to 3.0 in steps of 0.1 every 50 iterations. After p reaches 3.0, the beta parameter of the Heaviside projection filter of Guest et al. (2004) is incremented until convergence or 1200 iterations, whichever comes first. Manufacturability constraints are active in the cMMC solution, including bridging data, with 60 iterations of continuation for γ, and component endpoints are restricted from the right and top edges of the design domain as shown

[12] This problem was put forth by the company Messerschmitt-Blölkw-Blohm Gmbh in Germany as a test problem to the literature (Bulman et al., 2001)

in Figure 4.29b. The SIMP filter size is set to 0.3 mm (to create 0.6mm thick features), which is just less than the smallest manufacturable feature size. The volume fraction is set to 0.40. The SIMP code is run for 1200 iterations as described above, producing the result shown in Figure 4.29c, and skeletal segments are converted into junction points and component information following the graph in Figure 4.29d. A SIMP solution with a minimum feature thickness of 1.0 mm (r_{min} = 0.5 mm) is shown in Figure 4.30.

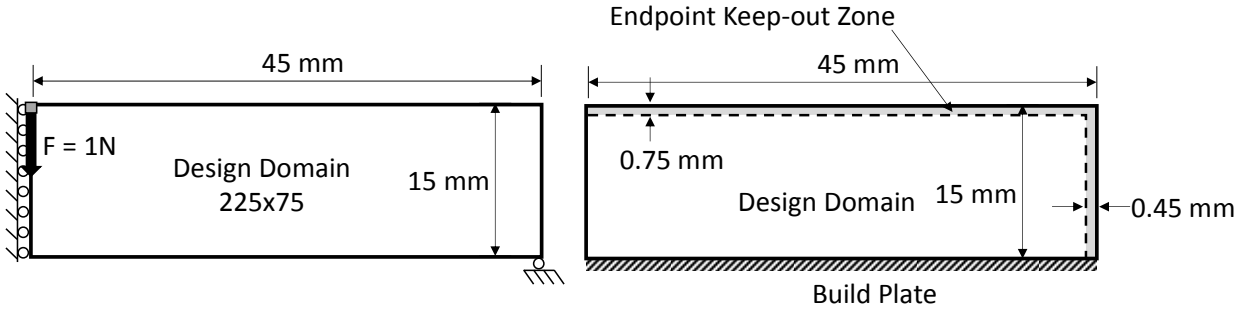

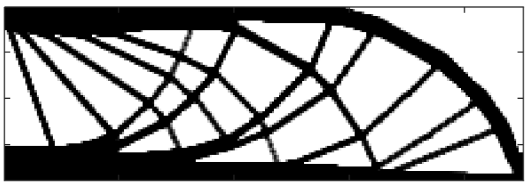

SIMP, 50 iterations, $r_{min} = 0.3\ mm$, $\bar{f} = 219.71$

(c).

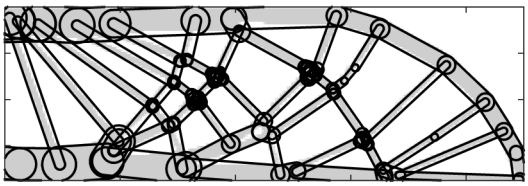

(d)

Figure 4.29. Problem domain for the MBB problem. (a) SIMP domain and loads/supports. (b) MMC domain with manufacturing information. MMC optimization uses the same load and support configuration as that in (a). (c) the SIMP solution after 1200 iterations used for bootstrapping, with minimum element thickness of 0.6mm (d) The extracted junction and component information

Figure 4.30. Reference manufacturable SIMP solution, 1200 iterations, minimum element thickness of 1.0mm. $\bar{f} = 219.43$

Figure 4.31 presents the bcMMC result for this configuration, with manufacturing penalties allowing bridging enabled. The cMMC code is allowed to run until convergence up to 200

iterations. In this case, many of the smaller features have been removed from the design, producing a solution which resembles the reference configuration in Figure 4.30, and a thresholded compliance of $\bar{f} = 222.35$ is obtained, which is 1.3% worse than the SIMP result for a 1.0 mm minim feature thickness shown in Figure 4.30. However, the ability of the manufacturing constraint to allow bridging members allows the top element to be retained without additional supports, unlike the other overhang topology optimization approaches surveyed (see Figure 4.7). Some intermediate solutions from the bcMMC solution are shown in Figure 4.32.

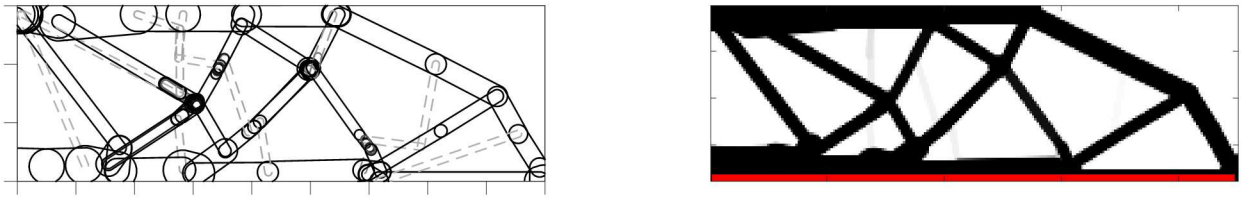

(a) (b)

Figure 4.31. Bootstrapped bcMMC solution for the MBB problem. Volume fraction of 40%, manufacturing penalization enabled, $\bar{f} = 222.35$ after 50+200 iterations.

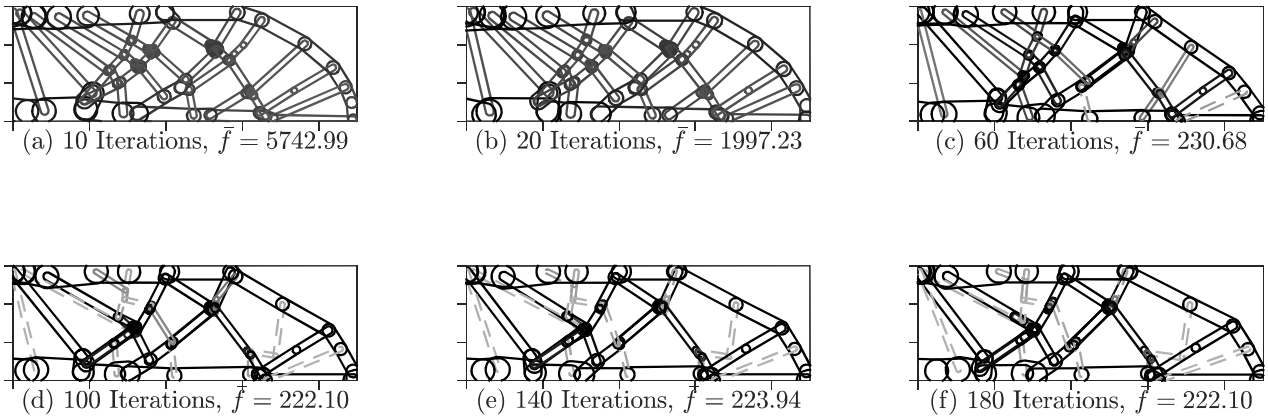

(a) 10 Iterations, $\bar{f} = 5742.99$ (b) 20 Iterations, $\bar{f} = 1997.23$ (c) 60 Iterations, $\bar{f} = 230.68$

(d) 100 Iterations, $\bar{f} = 222.10$ (e) 140 Iterations, $\bar{f} = 223.94$ (f) 180 Iterations, $\bar{f} = 222.10$

Figure 4.32. Intermediate steps of the results shown in Figure 4.31.

As with the short beam problem, three designs were manufactured, with results shown in Figure 4.33. All three manufactured results struggle with surface finish in the overhanging features, however the drooping in the very thin members in the more aggressive SIMP case (with minimum member thickness of 0.71 mm) result in a significant fraction of each beam not being fully manifested. In the MMC solution, all drooping features occur for thicker beams which

ensures that the integrity of the structure is not compromised by the poor surface finish. Note the way that the bcMMC optimizer adjusts the overhang angle and thickness of major features in the design to be better supported, and thickens some of the smaller elements to increase manufacturing performance (see arrows in Figure 4.33).

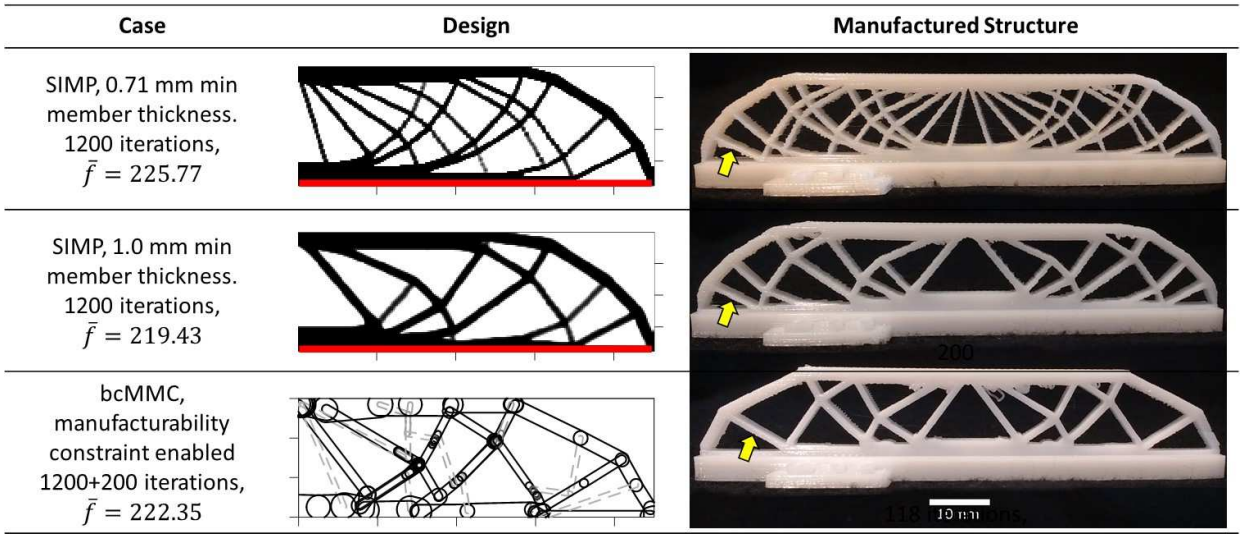

Figure 4.33. Manufactured SIMP and MMC designs.

A volume fraction study was also performed for the MBB beam problem, with results shown in Figure 4.34. As the volume fraction decreases, both the number of elements retained in the final design is also reduced. In the 30% case (bottom row of the table), the slender horizontal features cannot be manufactured even with the bridging allowance in the design rule function, resulting in a major change in topology to achieve a manufacturable design, at the expense of a significant performance penalty.

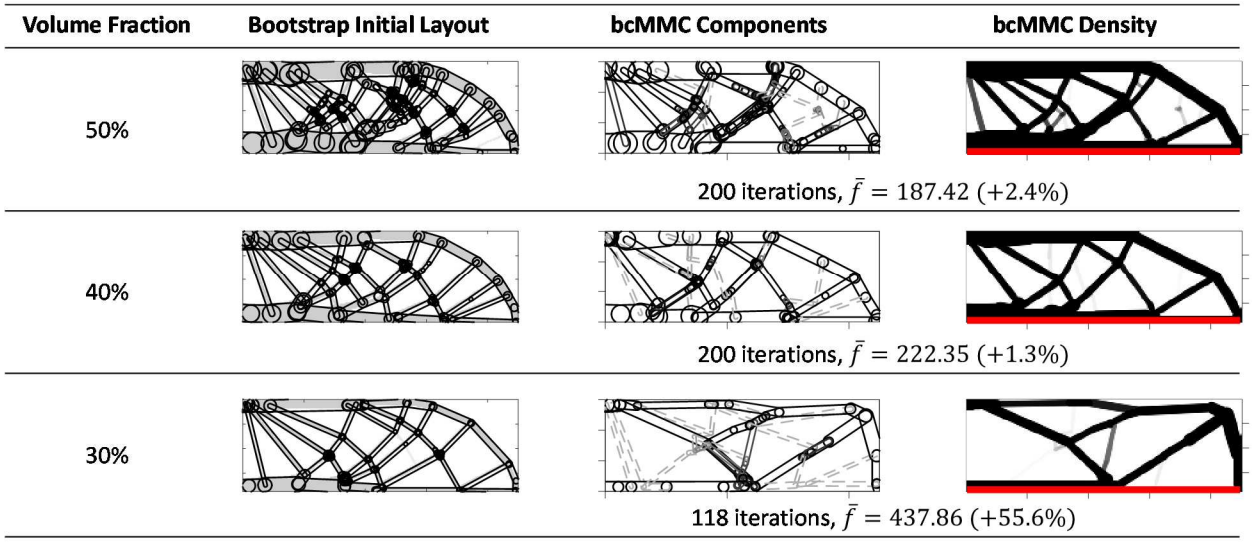

Figure 4.34. Volume fraction study for the MBB problem. Percentages shown are difference from an equivalent SIMP solution with minimum member thickness of 1.0 mm.

E. The Bottom-Loaded Span Problem

Another load case, shown in Figure 4.35, presents one more test of the bcMMC framework. The domain is symmetric, and solutions should be reasonably symmetric as well. The 160x80 FEA domain has dimensions 30mm by 15 mm (2:1), and the build plate is placed outside the domain with external supporting elements connecting it to the optimized structure, as shown in Figure 4.35b. Three solid non-designable regions connect the loads and supports to the interior of the design domain instead of including explicit components linking the load and support points to the structure. The SIMP implementation used for bootstrapping uses the Heaviside projection filter of Guest et al. (2004) over 50 iterations with no p continuation. Manufacturability constraints are active, including bridging data, with 60 iterations of continuation for γ. The SIMP filter size is set to 0.3 mm (to create 0.6mm features), which is just less than the smallest manufacturable feature size. The volume fraction is set to 0.30.

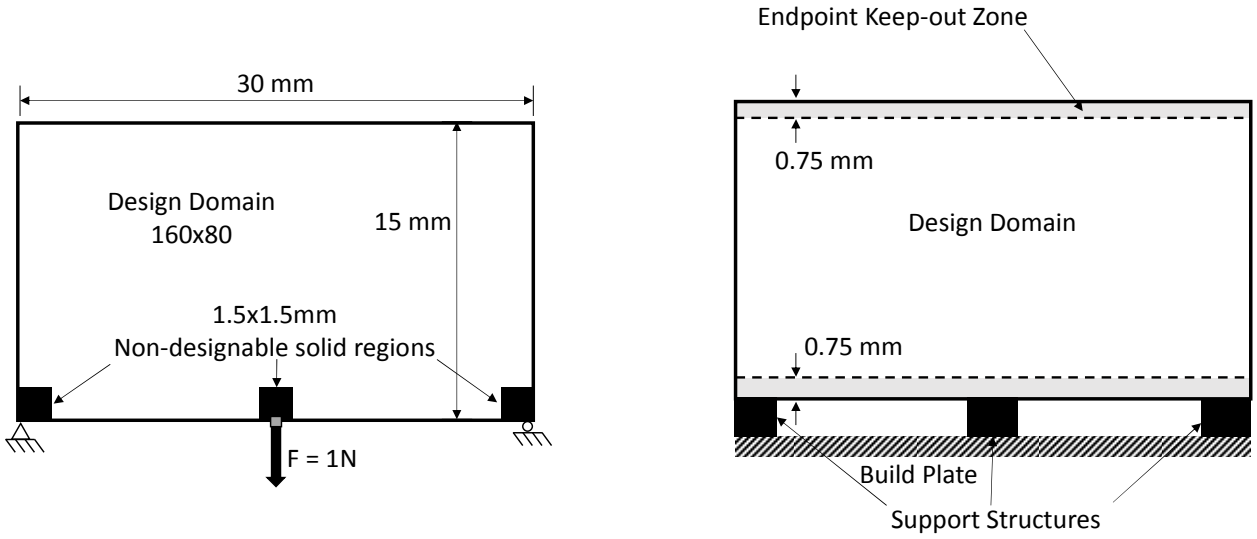

(a) (b)

Figure 4.35. Design domain for the bottom-loaded span problem. (a) SIMP domain. (b) MMC domain with build information. Note that the black boxes refer to different structures in (a) and (b).

The SIMP algorithm is run for 50 iterations, as shown in Figure 4.36a, and skeletal segments are converted into junction points and component information following the graph in Figure 4.36b. The MMC code allowed to run until convergence up to 400 iterations. The results show symmetric topologies similar to the SIMP solution, except for small topology changes to eliminate thin features and two very thick components on each side (Figure 4.36c, d). The imposed manufacturing constraints result in a 4.5% increase in the objective function compared to a converged SIMP result with 1.0mm constant minimum member thickness.

SIMP, 50 iterations. $\bar{f} = 22.08$
(a)

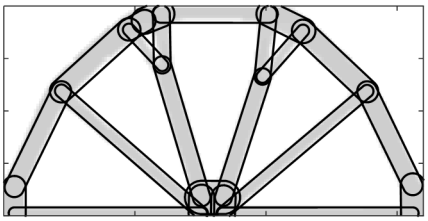

Extracted initial component layout
(b)

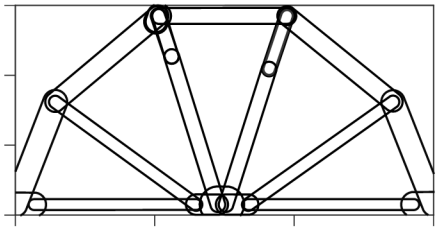

bcMMC, 50+400 iterations, $\bar{f} = 22.37$ (+4.5%)
(c)

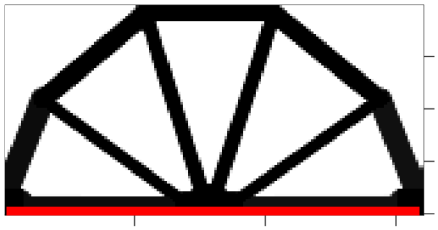

Density plot for bcMMC solution in (c)
(d)

Figure 4.36. Bottom-loaded span example problem, for a volume fraction of 30%. (a) SIMP bootstrap design. (b) Component graph extracted from the SIMP design. (c) Converged MMC component plot, after 400 cMMC iterations, $\bar{f} = 22.37$, which is 4.5% greater than the converged SIMP solution with $r_{min} = 1.0$ mm. (d) Converged MMC density field.

Typically, the bootstrapped MMC algorithm makes only small changes to the structure topology. In this case, significant changes are seen with the use of the two different constraint functions for a volume fraction of 28%, see Figure 4.37[13]. The SIMP design used for bootstrapping resembles the 30% case shown in Figure 4.36b. When bridging data is included in the constraint function (see Figure 4.9b), the horizontal members are manufacturable with less material (all members in the design domain are above the build platform in this example) and the design can follow the general shape of the SIMP design (top row, Figure 4.37). However, without including the bridging data (i.e. using Figure 4.9a), horizontal features are significantly penalized, and the additional material that must be supplied to the horizontal members results in a reorganization of the structure's topology to remove as many horizontal members as possible, and a 16.2% penalty incurred for manufacturability compared with the 1.0 mm SIMP solution (bottom row,

[13] Is this example contrived? Absolutely. Interesting behavior for the bcMMC algorithm occurs just on the transition between fully manufacturable designs and impossible-to-manufacture designs. Finding that transition to best highlight the capabilities of this approach required a little guesswork.

Figure 4.37). Manufactured forms of each of these designs are shown in the last column of Figure 4.37. Note that two additional supporting structures are required to ensure the "V" junction noted by the arrow in Figure 4.37 can be manufactured.

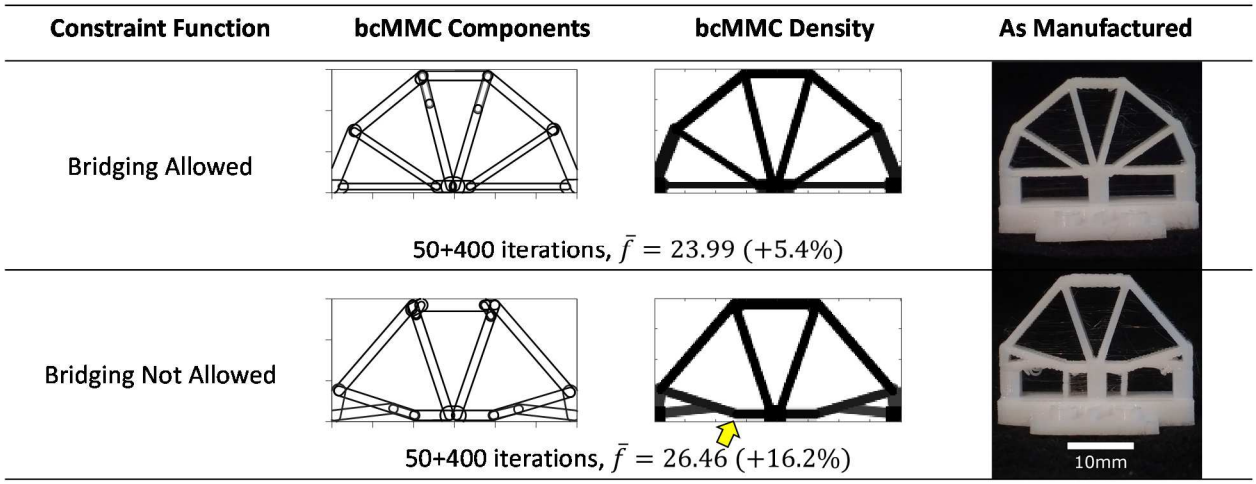

Figure 4.37. MMC results for the bottom-loaded span example problem, with and without bridging data included in the constraint. Volume fraction is 28%. Percentages indicate deviation from converged SIMP solution with 1.0 mm minimum feature size.

4.9 CONCLUSION

A data-driven manufacturing constraint function for additive manufacturing of topology-optimized designs has been presented and applied to the solution of several compliance minimization problems. To support this constraint, which provides a different minimum member thickness based on the shape and orientation of each straight segment in a design, a variant of the Moving Morphable Components (MMC) framework which utilizes SIMP to generate preliminary designs to serve as starting points is presented and validated. This "bootstrapped" MMC approach provides faster convergence to optimized solutions in the absence of constraints than reference MMC implementations, and allows the manufacturability constraint to be applied component-by-component in the MMC framework to create the bootstrapped constrained MMC method (bcMMC).

The more detailed manufacturing constraint considered here utilizes the results of a previously-reported thorough experiment to create a detailed map of the minimum

manufacturable diameter of small features of various shapes and in different orientations (see Chapters 2 and 3). Compared to other manufacturing constraints for topology optimization in AM, which typically utilize a single fixed minimum feature size and a maximum overhang angle, this functional constraint helps take better advantage of the space of manufacturable geometries, increasing the design complexity the optimizer can achieve. For example, very short features can be manufactured on the selected material extrusion AM platform at almost any angle, regardless of the overhang limit, but such features are excluded from the space of possible designable features if an overhang angle constraint is imposed.

The topology optimization approach presented is combined with the additive manufacturing constraint functions in several examples for compliance minimization manufactured on an example material extrusion AM platform, but the approach is easily generalized to other objective functions and AM processes. The results obtained show the modified optimization process makes relatively small changes to the part topology and component orientation and/or size to ensure the existing design is both optimized and manufacturable, generally with a penalty to the objective function less than 5% compared with the unconstrained solution. Significant topology changes are occasionally seen, however, when key members in a design cannot be produced. The output geometries have been manufactured on the target AM platform, and require at most only point supports in locations where "V"-like junctions are present.

Several exciting possibilities for extensions of this work present themselves, including adapting the approach to 3D problems, different objective functions, and other AM processes. In addition, enabling the bcMMC framework to instantiate new members midway through the optimization process would be an exciting direction, the solid equivalent of the void-generating "Bubble Method" (Eschenauer et al., 1994), and allowing more significant changes in topology. The automatic generation of fully self-supporting structures by penalizing or constraining "V"-

like joints (see Figure 4.10), or by automatically adding members to ensure such joints are supported, is also a significant area of interest.

CONCLUSION

In the previous chapters, an approach for determining parametric design rules from experimental trials on an additive manufacturing process has been presented and applied to three AM platforms, and the results used in automated design methods (topology optimization). As such, this work forms the first attempt to explicitly bring together experimental data for minimum feature size in an AM process with the topology optimization framework to achieve optimized structures which obey a parametric manufacturability constraint.

Chapter 2 reported a preliminary method for characterizing the minimum feature size across a parameter space of small features of different shapes and orientations in a polyamide laser powder bed fusion process. The unique iterative process for determining minimum feature size helped adjust the experiments to focus on the region of most useful data in order to provide highly accurate minimum feature size estimates which also account for the statistical variation of the process. The study reported in Chapter 2 explored the space of oriented slot features more thoroughly than any other work available and demonstrated more than an order of magnitude in variation across the shape and orientation space sampled. The resulting design rule improved the prediction accuracy using a test dataset by a factor of two compared to a design rule derived from the NIST-approved test artifact (reducing error from 67% to 34%; see Moylan et al. (2014)).

This approach was extended and applied to example processes from the material extrusion and vat photopolymerization additive manufacturing process categories in Chapter 3, which was the first study to quantitatively explore the relationship between the amount of data collected and design rule quality, assessing the importance of the number of shapes and orientations sampled and the amount of data to collect for each. For the material extrusion process, a 30-50% reduction in prediction error was realized when comparing a linear fit with minimal data and one based on 30 sampled points in the parameter space. A Maximum Entropy design of experiments approach (Shewry and Wynn, 1987) was used, enabling the experiment size to be varied as the experiment

progresses, helping create the best design rules possible within a resource constraint for new AM platforms. As in Chapter 2, the minimum feature size for the material extrusion process was seen to grow an order of magnitude above the physical limits of the process resolution for some sets of parameters. Overhanging features were seen to require significantly larger minimum feature sizes without support on the material extrusion process, consistent with expectations from the process physics. An industry-accepted minimum wall thickness of 1.0mm for a similar process in the material extrusion process category ("Design Guide: ABS 3D Printing," n.d.) was found to over-estimate the true minimum manufacturable wall thickness by 0.591 mm on average for features not exceeding a 45° overhang angle, while also underestimating the achievable minimum feature size for some slender vertical features. The contributions in this chapter represent the greatest contributions made in this dissertation.

Finally, Chapter 4 addressed the need expressed in the literature for better integration of manufacturing constraints for AM in the topology optimization process (Rosen, 2014). To that end, the novel parametric design rule developed in Chapter 3 was applied to a variant of moving morphable components (MMC) topology optimization to penalize unmanufacturable features. To support the application of the design rule function, a bootstrapped, constrained MMC topology optimization framework (bcMMC) was developed and demonstrated on several test problems. Generally, the manufacturability penalty ensures the resulting design consists of manufacturable geometries and incurs a penalty in the objective function of around 5% compared to comparable SIMP solutions. As such, it is the first work to use a penalization based on a function of feature shape to ensure manufacturability.

5.1 Future Work

The preliminary results reported in this manuscript suggest several areas of future research. Based on the learnings from the assessment of vat photopolymerization minimum feature size, several adjustments to the approach are mentioned in Chapter 3, including modifying the

parameter space to specify width and length of features explicitly (instead of using aspect ratios), supporting both ends of all small features, not just horizontal ones, and providing more precise definitions for "passing" features. In addition, a more precise criterion for stopping the iterative sub-experiment should be developed. After these changes, the characterization process could be condensed onto a smaller number of more complete test artifacts, reducing the time and resource costs of evaluating a new platform.

As additional data is gathered, the limitations on the scope of the features assessed could be relaxed by increasing the number of factors considered in the experimental design. Curved features and slanted features (where the planar feature is rotated about the feature axis) are not considered in this work, yet appear frequently in design problems. Further incorporating the subtleties of feature interactions, where multiple small features in proximity affect each other, process parameter settings, and environmental conditions are all additional variables worthy of further study, but can be harder to quantify. Ultimately, some degree of expert knowledge will still need to be utilized when applying these design rules to account for these unmodeled characteristics.

In addition to characterizing a process, the statistical information already gathered about minimum feature size could be used to create a small, efficient test artifact for frequent inclusion in builds, providing tools for ongoing quality assurance and process stability measurements using techniques from statistical process control.

Alternative design rule functions could also be explored, such as radial basis functions, Fourier series, or wavelet interpolation. In addition, the statistical information from the logistic regression can be propagated to the design rule fit, providing additional controls on the conservativeness of the design rule function. Specifically, this could be achieved by incorporating the confidence interval of the minimum feature size into the fitting operation or adjusting the manufacturing probability associated with minimum feature size assessment.

The topology optimization approach presented here is a first step, and significant work remains to increase robustness, explore performance when using constraint functions from other AM processes, and further improve convergence. A simple penalization of the objective function for features which require supports to avoid unacceptable surface finish would be straightforward to implement, as would automatically detecting and supporting down-facing "V" junctions. Extension to 3D problems and automatic generation of new members to increase the topology change capabilities of the process would also bring significant improvements. Finally, the build orientation could be included as an optimization variable, as in Guo et al. (2017).

5.2 Parting Thought

A method to create design rules for additive manufacturing of small features using extensive experimental data has been developed and presented and forms the culminating contribution of this work. In addition to applications in typical design problems, the resulting design rules have been integrated into an automated design process to ensure manufacturable results. The approaches presented fill a felt need in the literature, and provide a reproducible process for generating design rules and integrating them into optimized designs.

BIBLIOGRAPHY

3D Printing with FDM [WWW Document], n.d. . Strat. Direct Manuf. URL https://www.stratasysdirect.com/resources/fdm-video/ (accessed 11.7.17).

Andreassen, E., Clausen, A., Schevenels, M., Lazarov, B.S., Sigmund, O., 2011. Efficient topology optimization in MATLAB using 88 lines of code. Struct. Multidiscip. Optim. 43, 1–16. https://doi.org/10.1007/s00158-010-0594-7

ASTM International, 2015. ASTM ISO/ASTM52900-15 Standard Terminology for Additive Manufacturing — General Principles — Terminology.

Bendsøe, M., 1988. Generating optimal topologies in structural design using a homogenization method. Comput. Methods Appl. Mech. Eng. 71, 197–224.

Bendsøe, M.P., Sigmund, O., 2003. Topology optimization: theory, methods, and applications. Springer, Berlin ; New York.

Borrvall, T., Petersson, J., 2003. Topology optimization of fluids in Stokes flow. Int. J. Numer. Methods Fluids 41, 77–107. https://doi.org/10.1002/fld.426

Bourdin, B., 2001. Filters in topology optimization. Int. J. Numer. Methods Eng. 50, 2143–2158. https://doi.org/10.1002/nme.116

Bremicker, M., Chirehdast, M., Kikuchi, N., Papalambros, P.Y., 1991. Integrated Topology and Shape Optimization in Structural Design. Mech. Struct. Mach. 19, 551–587. https://doi.org/10.1080/08905459108905156

Bruns, T.E., Tortorelli, D.A., 2001. Topology optimization of non-linear elastic structures and compliant mechanisms. Comput. Methods Appl. Mech. Eng. 190, 3443–3459. https://doi.org/10.1016/S0045-7825(00)00278-4

Bulman, S., Sienz, J., Hinton, E., 2001. Comparisons between algorithms for structural topology optimization using a series of benchmark studies. Comput. Struct. 79, 1203–1218. https://doi.org/10.1016/S0045-7949(01)00012-8

Burger, M., Osher, S.J., 2005. A survey on level set methods for inverse problems and optimal design. Eur. J. Appl. Math. 16, 263–301. https://doi.org/10.1017/S0956792505006182

Byun, H.-S., Lee, K.H., 2006. Determination of the optimal build direction for different rapid prototyping processes using multi-criterion decision making. Robot. Comput.-Integr. Manuf. 22, 69–80. https://doi.org/10.1016/j.rcim.2005.03.001

Byun, H.-S., Lee, K.H., 2003. Design of a New Test Part for Benchmarking the Accuracy and Surface Finish of Rapid Prototyping Processes, in: Kumar, V., Gavrilova, M.L., Tan, C.J.K., L'Ecuyer, P. (Eds.), Computational Science and Its Applications — ICCSA 2003. Springer Berlin Heidelberg, Berlin, Heidelberg, pp. 731–740.

Castillo, L., 2005. Study about the rapid manufacturing of complex parts of stainless steel and titanium (Technical Report). TNO report with the collaboration of AIMEE.

Chang, K.-H., Tang, P.-S., 2001. Integration of design and manufacturing for structural shape optimization. Adv. Eng. Softw. 32, 555–567. https://doi.org/10.1016/S0965-9978(00)00103-4

Chu, C., Graf, G., Rosen, D.W., 2008. Design for Additive Manufacturing of Cellular Structures. Comput.-Aided Des. Appl. 5, 686–696. https://doi.org/10.3722/cadaps.2008.686-696

Clausen, A., Aage, N., Sigmund, O., 2014. Topology optimization with flexible void area. Struct. Multidiscip. Optim. 50, 927–943. https://doi.org/10.1007/s00158-014-1109-8

Coelho, P.G., Cardoso, J.B., Fernandes, P.R., Rodrigues, H.C., 2011. Parallel computing techniques applied to the simultaneous design of structure and material. Adv. Eng. Softw. 42, 219–227. https://doi.org/10.1016/j.advengsoft.2010.10.003

Deaton, J.D., Grandhi, R.V., 2014. A survey of structural and multidisciplinary continuum topology optimization: post 2000. Struct. Multidiscip. Optim. 49, 1–38. https://doi.org/10.1007/s00158-013-0956-z

Deng, J., Chen, W., 2016. Design for structural flexibility using connected morphable components based topology optimization. Sci. China Technol. Sci. 59, 839–851. https://doi.org/10.1007/s11431-016-6027-0

Design Guide: ABS 3D Printing [WWW Document], n.d. . i.materialise. URL https://i.materialise.com/3d-printing-materials/abs/design-guide (accessed 11.7.17).

Design Guidelines: Fused Deposition Modeling (FDM) [WWW Document], n.d. . Stratasys. URL https://www.stratasysdirect.com/resources/fused-deposition-modeling/ (accessed 2.3.17).

Design Guides: Gray Resin 3D Printing [WWW Document], n.d. . i.materialise. URL https://i.materialise.com/3d-printing-materials/gray-resin/design-guide (accessed 11.7.17).

Design rules and detail resolution for SLS 3D printing [WWW Document], n.d. . Shapeways.com. URL https://www.shapeways.com/tutorials/design_rules_for_3d_printing (accessed 2.3.17).

Driessen, A.M., 2016. Overhang constraint in topology optimisation for additive manufacturing: A density gradient based approach. Delft University of Technology, Delft, Netherlands.

EnableCommunityFoundation, 2016. e-NABLE Phoenix Hand v2 [WWW Document]. URL http://www.thingiverse.com/thing:1453190 (accessed 9.29.16).

Eschenauer, H.A., Kobelev, V.V., Schumacher, A., 1994. Bubble method for topology and shape optimization of structures. Struct. Optim. 8, 42–51. https://doi.org/10.1007/BF01742933

Gao, W., Zhang, Y., Ramanujan, D., Ramani, K., Chen, Y., Williams, C.B., Wang, C.C.L., Shin, Y.C., Zhang, S., Zavattieri, P.D., 2015. The status, challenges, and future of additive manufacturing in engineering. Comput.-Aided Des. 69, 65–89. https://doi.org/10.1016/j.cad.2015.04.001

Gaynor, A., 2015. Topology Optimization Algorithms for Additive Manufacturing (Ph. D.). John Hopkins University, Baltimore, Maryland.

Gersborg-Hansen, A., Bendsøe, M.P., Sigmund, O., 2006. Topology optimization of heat conduction problems using the finite volume method. Struct. Multidiscip. Optim. 31, 251–259. https://doi.org/10.1007/s00158-005-0584-3

Govett, T., Kim, K., Lundin, M., Pinero, D., 2012. Design Rules for Selective Laser Sintering (Sr. Design Project). University of Texas at Austin, Austin, TX.

Gu, X.J., Zhu, J.H., Zhang, W.H., 2012. The lattice structure configuration design for stereolithography investment casting pattern using topology optimization. Rapid Prototyp. J. 18, 353–361. https://doi.org/10.1108/13552541211250355

Guedes, J., Kikuchi, N., 1990. Preprocessing and postprocessing for materials based on the homogenization method with adaptive finite element methods. Comput. Methods Appl. Mech. Eng. 83, 143–198. https://doi.org/10.1016/0045-7825(90)90148-F

Guest, J.K., Prévost, J.H., Belytschko, T., 2004. Achieving minimum length scale in topology optimization using nodal design variables and projection functions. Int. J. Numer. Methods Eng. 61, 238–254. https://doi.org/10.1002/nme.1064

Guirguis, D., Hamza, K., Aly, M., Hegazi, H., Saitou, K., 2015. Multi-objective topology optimization of multi-component continuum structures via a Kriging-interpolated level set approach. Struct. Multidiscip. Optim. 51, 733–748. https://doi.org/10.1007/s00158-014-1154-3

Guo, X., Zhang, W., Zhang, J., Yuan, J., 2016. Explicit structural topology optimization based on moving morphable components (MMC) with curved skeletons. Comput. Methods Appl. Mech. Eng. 310, 711–748. https://doi.org/10.1016/j.cma.2016.07.018

Guo, X., Zhang, W., Zhong, W., 2014a. Doing Topology Optimization Explicitly and Geometrically—A New Moving Morphable Components Based Framework. J. Appl. Mech. 81, 081009. https://doi.org/10.1115/1.4027609

Guo, X., Zhang, W., Zhong, W., 2014b. Explicit feature control in structural topology optimization via level set method. Comput. Methods Appl. Mech. Eng. 272, 354–378. https://doi.org/10.1016/j.cma.2014.01.010

Guo, X., Zhou, J., Zhang, W., Du, Z., Liu, C., Liu, Y., 2017. Self-supporting structure design in additive manufacturing through explicit topology optimization. Comput. Methods Appl. Mech. Eng. 323, 27–63. https://doi.org/10.1016/j.cma.2017.05.003

Gustafson, P., 2012. 3D Printing and the Future of Manufacturing.

Haftka, R.T., Grandhi, R.V., 1986. Structural shape optimization—A survey. Comput. Methods Appl. Mech. Eng. 57, 91–106. https://doi.org/10.1016/0045-7825(86)90072-1

Hague, R., Mansour, S., Saleh, N., 2004. Material and design considerations for rapid manufacturing. Int. J. Prod. Res. 42, 4691–4708. https://doi.org/10.1080/00207840410001733940

Hamza, K., Aly, M., Hegazi, H., 2013. An Explicit Level-Set Approach for Structural Topology Optimization. ASME, p. V03AT03A001. https://doi.org/10.1115/DETC2013-12155

Harzheim, L., Graf, G., 2006. A review of optimization of cast parts using topology optimization: II-Topology optimization with manufacturing constraints. Struct. Multidiscip. Optim. 31, 388–399. https://doi.org/10.1007/s00158-005-0554-9

Hiller, J.D., Lipson, H., 2009. Multi material topological optimization of structures and mechanisms. ACM Press, p. 1521. https://doi.org/10.1145/1569901.1570105

Hoang, V.-N., Jang, G.-W., 2017. Topology optimization using moving morphable bars for versatile thickness control. Comput. Methods Appl. Mech. Eng. 317, 153–173. https://doi.org/10.1016/j.cma.2016.12.004

Hollister, S.J., 2005. Porous scaffold design for tissue engineering. Nat. Mater. 4, 518–524. https://doi.org/10.1038/nmat1421

ISO 10791-7, 2014. Test conditions for machining centres -- Part 7: Accuracy of finished test pieces.

Jeepguy42, 2015. Seattle Space Needle [WWW Document]. URL www.thingiverse.com/thing:930296 (accessed 10.10.17).

Johnson, W.M., Rowell, M., Deason, B., Eubanks, M., 2011. Benchmarking Evaluation of an Open Source Fused Deposition Modelling Additive Manufacturing System, in: Proceedings of the 22nd International Solid Freeform Fabrication Symposium. Presented at the Solid Freeform Fabrication Symposium, Laboratory for Freeform Fabrication, University of Texas at Austin, Austin, TX.

Kintel, M., n.d. OpenSCAD [WWW Document]. URL http://openscad.org (accessed 10.10.17).

Kranz, J., Herzog, D., Emmelmann, C., 2015. Design guidelines for laser additive manufacturing of lightweight structures in TiAl6V4. J. Laser Appl. 27, S14001. https://doi.org/10.2351/1.4885235

Kruth, J., Van Vaerenbergh, J., Mercelis, P., 2005. Benchmarking of Different SLS/SLM Processes as Rapid Manufacturing Techniques. Presented at the International Conference on Polymers & Moulds Innovations (PMI), Gent, Belgium.

Kruth, J.P., 1991. Material Incress Manufacturing by Rapid Prototyping Techniques. CIRP Ann. - Manuf. Technol. 40, 603–614. https://doi.org/10.1016/S0007-8506(07)61136-6

Langelaar, M., 2017. An additive manufacturing filter for topology optimization of print-ready designs. Struct. Multidiscip. Optim. 55, 871–883. https://doi.org/10.1007/s00158-016-1522-2

Lantada, A.D., Morgado, P.L., 2012. Rapid Prototyping for Biomedical Engineering: Current Capabilities and Challenges. Annu. Rev. Biomed. Eng. 14, 73–96. https://doi.org/10.1146/annurev-bioeng-071811-150112

Lazarov, B.S., Wang, F., Sigmund, O., 2016. Length scale and manufacturability in density-based topology optimization. Arch. Appl. Mech. 86, 189–218. https://doi.org/10.1007/s00419-015-1106-4

Leiva, J., Watson, B., Kosaka, I., 2004. An Analytical Directional Growth Topology Parameterization to Enforce Manufacturing Requirements. American Institute of Aeronautics and Astronautics. https://doi.org/10.2514/6.2004-1645

Li, G., 2007. Online and Offline Approximations for Population based Multi-objective Optimization (PhD Dissertation). University of Maryland, College Park, MD.

Liu, J., Ma, Y., 2016. A survey of manufacturing oriented topology optimization methods. Adv. Eng. Softw. 100, 161–175. https://doi.org/10.1016/j.advengsoft.2016.07.017

Liu, K., Tovar, A., 2014. An efficient 3D topology optimization code written in Matlab. Struct. Multidiscip. Optim. 50, 1175–1196. https://doi.org/10.1007/s00158-014-1107-x

Luo, Z., 2013. A Short Survey: Topological Shape Optimization of Structures Using Level Set Methods. J. Appl. Mech. Eng. 02. https://doi.org/10.4172/2168-9873.1000123

Maher, M., Smith, A., Margiotta, J., 2014. A synopsis of the Defense Advanced Research Projects Agency (DARPA) investment in additive manufacture and what challenges remain, in: Helvajian, H., Piqué, A., Wegener, M., Gu, B. (Eds.), . p. 897002. https://doi.org/10.1117/12.2044725

Mahesh, M., 2004. Rapid Prototyping and Manufacturing Benchmarking (PhD Dissertation). National University of Singapore, Singapore.

Mahesh, M., Wong, Y.S., Fuh, J.Y.H., Loh, H.T., 2004. Benchmarking for comparative evaluation of RP systems and processes. Rapid Prototyp. J. 10, 123–135. https://doi.org/10.1108/13552540410526999

Materialise mv, n.d. 3D Printing Materials Design Guides [WWW Document]. URL https://i.materialise.com/3d-printing-materials/design-guides (accessed 9.29.16).

Mei, Y., Wang, X., Cheng, G., 2008. A feature-based topological optimization for structure design. Adv. Eng. Softw. 39, 71–87. https://doi.org/10.1016/j.advengsoft.2007.01.023

Meisel, N., Williams, C., 2015. An Investigation of Key Design for Additive Manufacturing Constraints in Multimaterial Three-Dimensional Printing. J. Mech. Des. 137, 111406–111406. https://doi.org/10.1115/1.4030991

Mertens, R., Clijsters, S., Kempen, K., Kruth, J.-P., 2014. Optimization of Scan Strategies in Selective Laser Melting of Aluminum Parts With Downfacing Areas. J. Manuf. Sci. Eng. 136, 061012. https://doi.org/10.1115/1.4028620

Moylan, S., Slotwinski, J., Cooke, A., Jurrens, K., Donmez, M.A., 2014. An Additive Manufacturing Test Artifact. J. Res. Natl. Inst. Stand. Technol. 119, 429–459. https://doi.org/10.6028/jres.119.017

Munk, D.J., Vio, G.A., Steven, G.P., 2015. Topology and shape optimization methods using evolutionary algorithms: a review. Struct. Multidiscip. Optim. 52, 613–631. https://doi.org/10.1007/s00158-015-1261-9

Nelaturi, S., Kim, W., Kurtoglu, T., 2015. Manufacturability Feedback and Model Correction for Additive Manufacturing. J. Manuf. Sci. Eng. 137, 021015. https://doi.org/10.1115/1.4029374

Ngim, D.B., Liu, J.-S., Soar, R.C., 2007. Design optimization for manufacturability of axisymmetric continuum structures using metamorphic development. Int. J. Solids Struct. 44, 685–704. https://doi.org/10.1016/j.ijsolstr.2006.05.016

Norato, J.A., Bell, B.K., Tortorelli, D.A., 2015. A geometry projection method for continuum-based topology optimization with discrete elements. Comput. Methods Appl. Mech. Eng. 293, 306–327. https://doi.org/10.1016/j.cma.2015.05.005

Park, J., Sutradhar, A., 2015. A multi-resolution method for 3D multi-material topology optimization. Comput. Methods Appl. Mech. Eng. 285, 571–586. https://doi.org/10.1016/j.cma.2014.10.011

Pingen, G., Waidmann, M., Evgrafov, A., Maute, K., 2010. A parametric level-set approach for topology optimization of flow domains. Struct. Multidiscip. Optim. 41, 117–131. https://doi.org/10.1007/s00158-009-0405-1

Ponche, R., Kerbrat, O., Mognol, P., Hascoet, J.-Y., 2014. A novel methodology of design for Additive Manufacturing applied to Additive Laser Manufacturing process. Robot. Comput.-Integr. Manuf. 30, 389–398. https://doi.org/10.1016/j.rcim.2013.12.001

Rosen, D., 2014. Design for Additive Manufacturing: Past, Present, and Future Directions. J. Mech. Des. 136, 090301. https://doi.org/10.1115/1.4028073

Rozvany, G.I.N., 2001. Aims, scope, methods, history and unified terminology of computer-aided topology optimization in structural mechanics. Struct. Multidiscip. Optim. 21, 90–108. https://doi.org/10.1007/s001580050174

Rozvany, G.I.N., Zhou, M., Birker, T., 1992. Generalized shape optimization without homogenization. Struct. Optim. 4, 250–252. https://doi.org/10.1007/BF01742754

Schramm, U., Zhou, M., 2006. Recent Developments in the Commercial Implementation of Topology Optimization, in: IUTAM Symposium on Topological Design Optimization of Strucutres, Machines, and Materials: Status and Perspectives. Presented at the IUTAM, pp. 239–248.

Schwerdtfeger, J., Wein, F., Leugering, G., Singer, R.F., Körner, C., Stingl, M., Schury, F., 2011. Design of Auxetic Structures via Mathematical Optimization. Adv. Mater. 23, 2650–2654. https://doi.org/10.1002/adma.201004090

Seepersad, C., Govett, T., Kim, K., Lundim, M., Pinero, D., 2012. A Designer's Guide for Dimensioning and Tolerancing SLS parts. Presented at the 23rd Annual International Solid Freeform Fabrication Symposium, Austin, TX, pp. 921–931.

Seo, Y.-D., Kim, H.-J., Youn, S.-K., 2010. Isogeometric topology optimization using trimmed spline surfaces. Comput. Methods Appl. Mech. Eng. 199, 3270–3296. https://doi.org/10.1016/j.cma.2010.06.033

Sheskin, D., 2011. Handbook of parametric and nonparametric statistical procedures, 5th ed. ed. CRC Press, Boca Raton.

Shewry, M.C., Wynn, H.P., 1987. Maximum entropy sampling. J. Appl. Stat. 14, 165–170. https://doi.org/10.1080/02664768700000020

Siddiqi, K., Pizer, S. (Eds.), 2008. Medial representations: mathematics, algorithms and applications, Computational imaging and vision. Springer, Dordrecht.

Sigmund, O., 2011. On the usefulness of non-gradient approaches in topology optimization. Struct. Multidiscip. Optim. 43, 589–596. https://doi.org/10.1007/s00158-011-0638-7

Sigmund, O., 2009. Manufacturing tolerant topology optimization. Acta Mech. Sin. 25, 227–239. https://doi.org/10.1007/s10409-009-0240-z

Sigmund, O., 2001a. Design of multiphysics actuators using topology optimization – Part II: Two-material structures. Comput. Methods Appl. Mech. Eng. 190, 6605–6627. https://doi.org/10.1016/S0045-7825(01)00252-3

Sigmund, O., 2001b. A 99 line topology optimization code written in Matlab. Struct. Multidiscip. Optim. 21, 120–127. https://doi.org/10.1007/s001580050176

Sigmund, O., 1997. On the Design of Compliant Mechanisms Using Topology Optimization*. Mech. Struct. Mach. 25, 493–524. https://doi.org/10.1080/08905459708945415

Sigmund, O., Maute, K., 2013. Topology optimization approaches: A comparative review. Struct. Multidiscip. Optim. 48, 1031–1055. https://doi.org/10.1007/s00158-013-0978-6

Sigmund, O., Maute, K., 2012. Sensitivity filtering from a continuum mechanics perspective. Struct. Multidiscip. Optim. 46, 471–475. https://doi.org/10.1007/s00158-012-0814-4

Sigmund, O., Petersson, J., 1998. Numerical instabilities in topology optimization: A survey on procedures dealing with checkerboards, mesh-dependencies and local minima. Struct. Optim. 16, 68–75. https://doi.org/10.1007/BF01214002

Svanberg, K., 1987. The method of moving asymptotes—a new method for structural optimization. Int. J. Numer. Methods Eng. 24, 359–373. https://doi.org/10.1002/nme.1620240207

Takalloozadeh, M., Yoon, G.H., 2017. Implementation of topological derivative in the moving morphable components approach. Finite Elem. Anal. Des. 134, 16–26. https://doi.org/10.1016/j.finel.2017.05.008

Thomas, D., 2009. The Development of Design Rules for Selective Laser Melting (Ph. D.). University of Wales Institue, Cardiff.

Thompson, M.K., Moroni, G., Vaneker, T., Fadel, G., Campbell, R.I., Gibson, I., Bernard, A., Schulz, J., Graf, P., Ahuja, B., Martina, F., 2016. Design for Additive Manufacturing: Trends, opportunities, considerations, and constraints. CIRP Ann. - Manuf. Technol. 65, 737–760. https://doi.org/10.1016/j.cirp.2016.05.004

Tomlin, M., Meyer, J., 2011. Topology Optimization of an Additive Layer Manufactured (ALM) Aerospace Part, in: 7th Altair CAE Technology Conference 2011. Presented at the 7th Altair CAE Technology Conference 2011, Altair.

Vayre, B., Vignat, F., Villeneuve, F., 2012. Designing for Additive Manufacturing. Procedia CIRP 3, 632–637. https://doi.org/10.1016/j.procir.2012.07.108

Wang, G.G., Shan, S., 2007. Review of Metamodeling Techniques in Support of Engineering Design Optimization. J. Mech. Des. 129, 370. https://doi.org/10.1115/1.2429697

Wang, M., Wang, X., 2004. PDE-Driven Level Sets, Shape Sensitivity and Curvature Flow for Structural Topology Optimization. Comput. Model. Eng. Sci. 6, 379–396. https://doi.org/10.3970/cmes.2004.006.373

Wang, M.Y., Wang, X., Guo, D., 2003. A level set method for structural topology optimization. Comput. Methods Appl. Mech. Eng. 192, 227–246. https://doi.org/10.1016/S0045-7825(02)00559-5

Wegner, A., Witt, G., 2012. Design rules for laser sintering. J. Plast. Technol. 8, 253–277.

Weiss, B., Diegel, O., Storti, D., Ganter, M., 2018. A Process for Estimating Minimum Feature Size in Selective Laser Sintering. Rapid Prototyp. J. 24.

What is Stereolithography (SLA)? [WWW Document], n.d. . 3D Syst. URL /resources/information-guides/stereolithography/sla (accessed 11.7.17).

Xu, F., Wong, Y.S., Loh, H.T., 2001. Toward generic models for comparative evaluation and process selection in rapid prototyping and manufacturing. J. Manuf. Syst. 19, 283–296. https://doi.org/10.1016/S0278-6125(01)89001-4

Yan, J., Duan, Z., Lund, E., Wang, J., 2017. Concurrent multi-scale design optimization of composite frames with manufacturing constraints. Struct. Multidiscip. Optim. 56, 519–533. https://doi.org/10.1007/s00158-017-1750-0

Yasa, E., Demir, F., Akbulut, G., Cizioglu, N., Pilatin, S., 2014. Benchmarking of different powder-bed metal fusion processes for machine selection in additive manufacturing, in: Proceedings of International Solid Freeform Fabrication Symposium. Austin, TX, pp. 390–403.

Yoon, G.H., Kim, Y.Y., Bendsøe, M.P., Sigmund, O., 2004. Hinge-free topology optimization with embedded translation-invariant differentiable wavelet shrinkage. Struct. Multidiscip. Optim. 27, 139–150. https://doi.org/10.1007/s00158-004-0378-z

Zhang, S., Norato, J.A., Gain, A.L., Lyu, N., 2016. A geometry projection method for the topology optimization of plate structures. Struct. Multidiscip. Optim. 54, 1173–1190. https://doi.org/10.1007/s00158-016-1466-6

Zhang, W., Li, D., Yuan, J., Song, J., Guo, X., 2017a. A new three-dimensional topology optimization method based on moving morphable components (MMCs). Comput. Mech. 59, 647–665. https://doi.org/10.1007/s00466-016-1365-0

Zhang, W., Yang, W., Zhou, J., Li, D., Guo, X., 2016a. Structural Topology Optimization Through Explicit Boundary Evolution. J. Appl. Mech. 84, 011011. https://doi.org/10.1115/1.4034972

Zhang, W., Yuan, J., Zhang, J., Guo, X., 2016b. A new topology optimization approach based on Moving Morphable Components (MMC) and the ersatz material model. Struct. Multidiscip. Optim. 53, 1243–1260. https://doi.org/10.1007/s00158-015-1372-3

Zhang, W., Zhang, J., Guo, X., 2016c. Lagrangian Description Based Topology Optimization—A Revival of Shape Optimization. J. Appl. Mech. 83, 041010. https://doi.org/10.1115/1.4032432

Zhang, W., Zhong, W., Guo, X., 2014. An explicit length scale control approach in SIMP-based topology optimization. Comput. Methods Appl. Mech. Eng. 282, 71–86. https://doi.org/10.1016/j.cma.2014.08.027

Zhang, W., Zhou, J., Zhu, Y., Guo, X., 2017b. Structural complexity control in topology optimization via moving morphable component (MMC) approach. Struct. Multidiscip. Optim. 56, 535–552. https://doi.org/10.1007/s00158-017-1736-y

Zhao, W., Chen, L., Zheng, C., Liu, C., Chen, H., 2017. Design of absorbing material distribution for sound barrier using topology optimization. Struct. Multidiscip. Optim. 56, 315–329. https://doi.org/10.1007/s00158-017-1666-8

Zhou, M., Fleury, R., Shyy, Y.-K., Thomas, H., Brennan, J., 2002. Progress in Topology Optimization with Manufacturing Constraints. American Institute of Aeronautics and Astronautics. https://doi.org/10.2514/6.2002-5614

Zhou, M., Rozvany, G.I.N., 1991. The COC algorithm, Part II: Topological, geometrical and generalized shape optimization. Comput. Methods Appl. Mech. Eng. 89, 309–336. https://doi.org/10.1016/0045-7825(91)90046-9

APPENDIX A: ADDITIONAL INFORMATION FOR CHAPTER 2

6.1 TEST ARTIFACT ITERATION

When a statistically reasonable logistic fit to the data is possible (i.e. if p < 0.5 and the fit region stays roughly within the range of manufactured features), the Green boundary is taken to be the 95% probability of a Green feature. To help prevent inverted results, an artificial data point of Not Green is included at 0 thickness. The transition is reported with a 90% Wald confidence interval, which highlights the uncertainty present when few trials have been used.

When a sharp Green transition occurs, no probability distribution is present and the 95% Green transition is approximated from the largest Not Green characteristic dimension d_{yr} and the smallest Green diameter d_g according to,

$$p_{95} = \frac{d_g + d_{yr}}{2} + \max\left(\left|d_g - d_{yr}\right|, d_\Delta\right)$$

where d_Δ is the dimension step size in the previous iteration. No confidence interval is possible for this case.

When a reasonable logistic fit is possible, the range of feature sizes to include in the next iteration is set to be the 5%-95% probability interval. When no logistic fit is available, a heuristic is utilized. The procedure utilized is summarized in the following pseudocode.

Listing A. Feature Range Update Heuristic Logic

```
Given: last_min, last_max (minimum and maximum feature thickness of last run)
       all_min, all_max (minimum and maximum feature thickness over all runs)
       lowest_green, highest_notgreen (data over all previous samples of this feature)
       logistic_05, logistic_95 (5% and 95% probability from a logistic fit)
       logistic_p_value (p value from the logistic fit)
       min_allowed (smallest allowable feature thickness)
Return: next_min, next_max (minimum and maximum feature thickness for next run)
Function NextFeatureRange:
  IF logistic_p_value < 0.5 AND logistic_95 – logistic_05 < 2 * (all_max – all_min):
    next_min ← logistic_05
    next_max ← logistic_95
  ELSE:
    center ← (lowest_green + highest_notgreen) / 2
```

```
center_percent ← (center – last_min) / (last_max – last_min)
centered ← (center_percent > 0.35) AND (center_percent < 0.65)
IF NOT centered AND last_min == min_allowed AND center_percent < 0.5:
    centered ← True
IF centered:
    new_span ← (last_max – last_min) * 0.75
    new_center ← center
ELSE IF lowest_green NOT FOUND:
    new_span ← (last_max – last_min) * 2
    new_center ← last_max
ELSE IF highest_notgreen NOT FOUND:
    new_span ← (last_max – last_min) * 2
    new_center ← last_min
ELSE:
    new_span ← (last_max – last_min)
    new_center ← center
next_min ← MAX(min_allowed, new_center – new_span / 2)
next_max ← MAX(min_allowed, new_center + new_span / 2)
```

6.2 Suitability of Logistic Regression

Underlying the use of logistic regression to analyze the data for each feature shape and orientation assumes that the physical system follows a logistic probability curve. To evaluate this, an additional test artifact with five features shapes was selected and manufactured 16 times, to produce 96 data points (6 copies per part x 16 manufacturing runs). No iteration was performed over the 16 manufacturing runs, and the 16 parts produced were of identical design. Figure 6.1a shows the coding for a single feature shape at 6 scales over the manufacturing runs, and Figure 6.1b shows a plot of the logistic fit obtained and the percentage of green features in each scale “bin”.

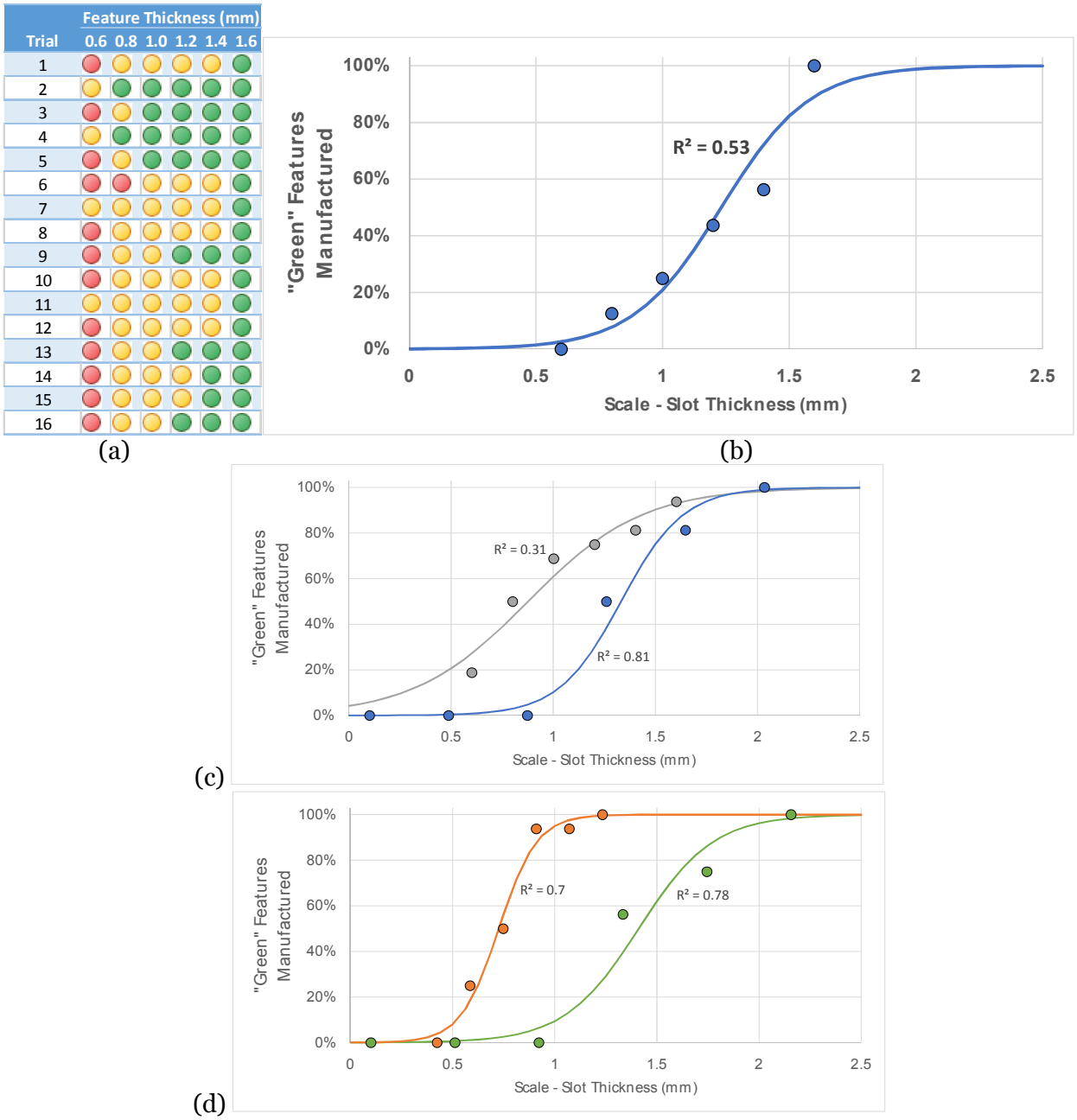

Figure 6.1. Logistic Regression fit evaluation. (a) Coding of six scales of a single feature over 16 manufacturing runs. (b) Experimentally-determined probability of success (points) plotted with the obtained logistic regression. (c), (d) Results obtained for the other four feature shapes and orientations evaluated.

6.3 VALIDATION

The validation test artifact provides an iterative mechanism to evaluate features of arbitrary coordinate in the parameter space in a manner similar to that used in the main test

artifact. The validation test performed in this study involved a series of points sampled on a sphere in the parameter space (see the main paper for the sphere size chosen). Figure 6.2 shows a digital rendering and photograph of this test part in its first iteration.

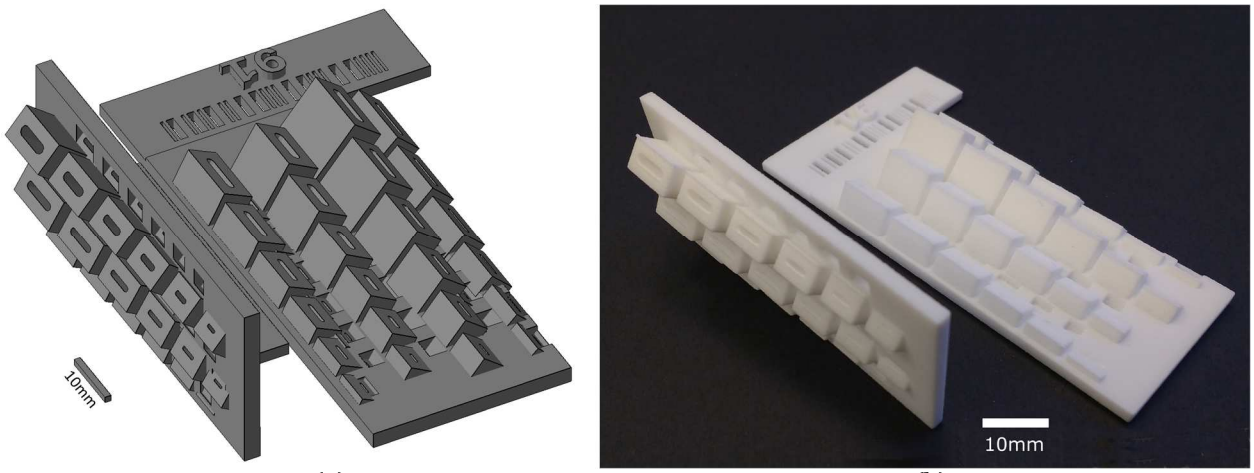

(a) (b)

Figure 6.2. Validation test artifact, first iteration. (a) model (b) as manufactured.

The results of the validation study are shown in Figure 6.3. Each validation data point corresponds to one coordinate sampled as described above and reported in the data table attached to the plot in Figure 6.3. The measured values obtained from the manufacture of five copies over three iterations of the validation test artifact are compared with the expected value based on the trilinear interpolation from the main test artifact, and good agreement is shown.

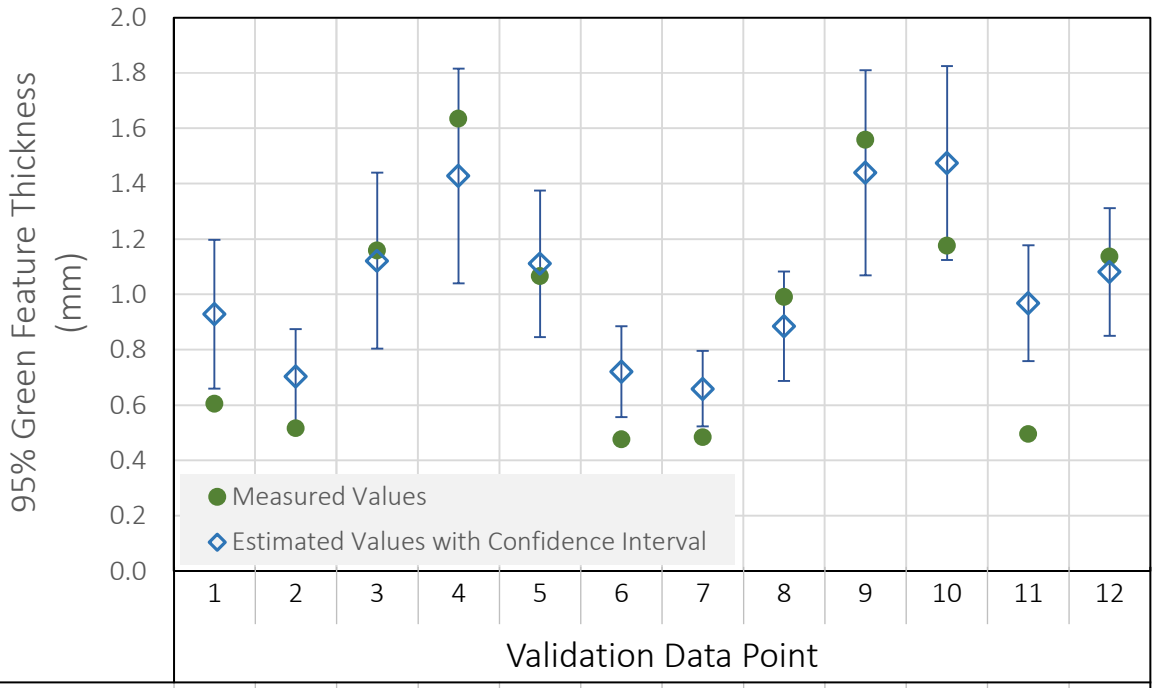

Measured 95% pt. (mm)		0.605	0.516	1.159	1.634	1.065	0.476	0.484	0.991	1.558	1.176	0.496	1.138
Est. 95% pt. (mm)		0.928	0.704	1.122	1.428	1.111	0.720	0.659	0.885	1.439	1.474	0.968	1.081
Est. Confidence Interval (mm)		0.268	0.171	0.318	0.388	0.265	0.165	0.137	0.197	0.371	0.351	0.209	0.231
Error (mm)		0.323	0.188	-0.037	-0.206	0.045	0.244	0.175	-0.106	-0.119	0.298	0.471	-0.057
Error (%)		53.4%	36.3%	-3.2%	-12.6%	4.3%	51.3%	36.1%	-10.7%	-7.7%	25.4%	95.0%	-5.0%
Coordinate	r_l	5.86	3.38	5.38	7.38	6.62	4.15	2.62	3.38	5.85	6.62	4.62	4.14
	r_w	0.125	0.143	0.166	0.190	0.181	0.152	0.210	0.219	0.248	0.257	0.234	0.275
	ϕ	45.0	39.5	27.1	39.5	59.5	59.5	50.5	30.5	30.5	50.5	62.9	45.0
Green Features		19	20	16	16	16	16	18	18	14	17	13	18
Total Features		30	30	30	30	30	30	30	30	30	30	30	30

Figure 6.3. Measured and estimated 95% Green Transition thicknesses for the 12 points in the validation dataset. Estimates use Equation 1; measurements represent five manufacturing runs over three iterations of the validation test artifact.

APPENDIX B: SAMPLE SHAPES AND ORIENTATIONS FOR ASSESSING MINIMUM FEATURE SIZE

In this appendix, the oriented features sampled for each of the datasets listed in Table 3.2 is presented. Each coordinate is given in both normalized (0-1) and parametric form for the experiment performed and reported in this manuscript. The parameters used here were $1 \leq r_l \leq 20$, $0.1 \leq r_w \leq 1.0$, and $0° \leq \phi \leq 90°$, but these can be adjusted by appropriately scaling the normalized coordinates to the range of features desired (for example, if assessing features above a certain overhang angle is not desired, the upper bound of ϕ could be adjusted).

For positive features in the material extrusion example process, the exact experiment used here replaced all features in the main MED dataset having $\phi = 90°$ with corresponding ones having $\phi = 80°$. Should the reader wish to replicate the separate bridging and main design rules, it would be better to simply set the upper bound for ϕ to 80 from the start.

In another variation, the parameters could be changed to represent width, length, and angle (instead of aspect ratios), requiring appropriate selections for the upper and lower bounds for each parameter based on the capabilities of the process and space of designs of interest to the user.

In the first two tables, MED experiments are listed. The order of features in these experiments is important, and sections of the first experiment must be performed before the supplementary bar dataset can be considered a correct MED.

Table 7.8 Main Maximum Entropy Design training dataset

Feature No	**Normalized Coordinate**			**Parameter Coordinate**		
	x_1	x_2	x_3	$r_l = 1 + 19x_1$	$r_w = 0.1 + 0.9x_2$	$\phi = 90x_3$
MED1	0.5	0.5	0.5	10.5	0.55	45
MED2	0	0	0	1	0.1	0
MED3	0	0	1	1	0.1	90

MED4	0	1	0	1	1	0
MED5	0	1	1	1	1	90
MED6	1	0	0	20	0.1	0
MED7	1	0	1	20	0.1	90
MED8	1	1	0	20	1	0
MED9	1	1	1	20	1	90
MED10	1	0.5	0.683333	20	0.55	61.5
MED11	0.683333	0.5	0	13.98333	0.55	0
MED12	0.3	0.5	1	6.7	0.55	90
MED13	0	0.5	0.3	1	0.55	27
MED14	0.5	1	0.683333	10.5	1	61.5
MED15	0.316667	0	0.5	7.016667	0.1	45
MED16	0.866667	0	0.5	17.46667	0.1	45
MED17	0.5	1	0.133333	10.5	1	12
MED18	0.5	0	1	10.5	0.1	90
MED19	0	1	0.5	1	1	45
MED20	1	1	0.5	20	1	45
MED21	0.5	0	0	10.5	0.1	0
MED22	0.733333	0.616667	1	14.93333	0.655	90
MED23	0	0.366667	0.716667	1	0.43	64.5
MED24	1	0.433333	0.25	20	0.49	22.5
MED25	0.266667	0.583333	0	6.066667	0.625	0
MED26	0.433333	1	1	9.233333	1	90
MED27	0	0	0.416667	1	0.1	37.5
MED28	0.683333	0.25	0.783333	13.98333	0.325	70.5
MED29	0.183333	0.716667	0.683333	4.483333	0.745	61.5
MED30	0.75	0.766667	0.333333	15.25	0.79	30
MED31	0.316667	0.266667	0.2	7.016667	0.34	18
MED32	1	0.366667	1	20	0.43	90
MED33	0	0.616667	1	1	0.655	90
MED34	0.683333	0.2	0.266667	13.98333	0.28	24
MED35	0.266667	0.8	0.316667	6.066667	0.82	28.5
MED36	0	0.35	0	1	0.415	0
MED37	1	0.65	0	20	0.685	0
MED38	0.8	0.816667	0.716667	16.2	0.835	64.5
MED39	0.3	0.2	0.783333	6.7	0.28	70.5
MED40	1	0.3	0	20	0.37	0

MED41	0	0.7	0	1	0.73	0
MED42	1	0.166667	0.7	20	0.25	63
MED43	0.7	0.833333	0	14.3	0.85	0
MED44	0	0	0.716667	1	0.1	64.5
MED45	1	0.7	1	20	0.73	90
MED46	0	0.3	1	1	0.37	90
MED47	0.6	0	0.666667	12.4	0.1	60
MED48	0.716667	1	1	14.61667	1	90
MED49	0.5	0.666667	0.783333	10.5	0.7	70.5
MED50	0.283333	1	0	6.383333	1	0
MED51	1	0.1	0.283333	20	0.19	25.5
MED52	0.183333	1	0.75	4.483333	1	67.5
MED53	1	0.716667	0.416667	20	0.745	37.5
MED54	0.216667	0.333333	0.483333	5.116667	0.4	43.5
MED55	0.55	0.316667	1	11.45	0.385	90

Table 7.9 presents the 21 supplemental MED coordinates sampled for cylindrical "bar" oriented features. This design is built assuming the following samples from the main MED experiment are already available as prior information: MED4, MED5, MED8, MED9, MED14, MED17, MED19, MED20, MED26, MED48, MED50, MED52.

Table 7.9 Supplemental MED design for Bar features ($r_w = 1$). Requires some elements from the main MED design (see text)

Feature No	**Normalized Coordinate**			**Parameter Coordinate**		
	x_1	x_2	x_3	$r_l = 1 + 19x_1$	$r_w = 0.1 + 0.9x_2$	$\phi = 90x_3$
Z1	0.283333	1	0.366667	6.383333	1	33
Z2	0.716667	1	0.383333	14.61667	1	34.5
Z3	0.833333	1	0.733333	16.83333	1	66
Z4	0.733333	1	0	14.93333	1	0
Z5	0	1	0.25	1	1	22.5
Z6	1	1	0.233333	20	1	21
Z7	0	1	0.766667	1	1	69
Z8	1	1	0.766667	20	1	69
Z9	0.2	1	1	4.8	1	90
Z10	0.5	1	0.45	10.5	1	40.5

Z11	0.5	1	0	10.5	1	0
Z12	0.283333	1	0.566667	6.383333	1	51
Z13	0.8	1	0.183333	16.2	1	16.5
Z14	0.166667	1	0.15	4.166667	1	13.5
Z15	0.616667	1	0.85	12.71667	1	76.5
Z16	0.683333	1	0.6	13.98333	1	54
Z17	0.35	1	0.85	7.65	1	76.5
Z18	0.116667	1	0.4	3.216667	1	36
Z19	0.866667	1	0.916667	17.46667	1	82.5
Z20	0.883333	1	0.4	17.78333	1	36
Z21	0.133333	1	0	3.533333	1	0

The main test dataset is presented in Table 7.10. The Latin Hypercube design requires that all 20 sample points be manufactured in order for it to effectively cover the parameter space. If a smaller Latin Hypercube design is desired, the Matlab command `lhsdesign(ND, 3, 'criterion', 'maximin', 'iterations', 100)` can be used to generate the normalized coordinates, where `ND` is the number of samples desired.

Table 7.10 3D Test dataset constructed using Latin Hypercubes

Feature No	**Normalized Coordinate**			**Parameter Coordinate**		
	x_1	x_2	x_3	$r_l = 1 + 19x_1$	$r_w = 0.1 + 0.9x_2$	$\phi = 90x_3$
LH1	0.398601	0.319453	0.13699	8.573422	0.387508	12.3291
LH2	0.224932	0.866401	0.37871	5.273713	0.879761	34.08388
LH3	0.680147	0.928029	0.283378	13.9228	0.935226	25.50398
LH4	0.475647	0.476524	0.988876	10.0373	0.528872	88.99884
LH5	0.426619	0.352382	0.400209	9.105769	0.417144	36.01877
LH6	0.628867	0.269247	0.158892	12.94848	0.342322	14.3003
LH7	0.956341	0.815184	0.031135	19.17048	0.833666	2.802109
LH8	0.16298	0.212943	0.476877	4.096622	0.291648	42.91891
LH9	0.105615	0.527878	0.749026	3.006693	0.57509	67.41236
LH10	0.322196	0.727648	0.234218	7.121728	0.754883	21.0796
LH11	0.921563	0.588881	0.697671	18.5097	0.629993	62.79041
LH12	0.782284	0.115368	0.759192	15.8634	0.203831	68.32725

LH13	0.058335	0.65842	0.53404	2.108374	0.692578	48.06361
LH14	0.263335	0.621402	0.622087	6.003363	0.659262	55.98785
LH15	0.840968	0.405166	0.574076	16.9784	0.464649	51.6668
LH16	0.743175	0.783009	0.901762	15.12032	0.804708	81.1586
LH17	0.867219	0.026486	0.326359	17.47716	0.123837	29.37231
LH18	0.013389	0.190297	0.845878	1.254385	0.271267	76.12899
LH19	0.573412	0.066539	0.885777	11.89483	0.159885	79.71993
LH20	0.527459	0.986748	0.091513	11.02172	0.988073	8.236151

Two auxiliary test datasets were constructed using Latin Hypercube design to provide validation data for bar and bridge subsets of the parameter space, and are given in

Table 7.11 Test dataset for bar features constructed using Latin Hypercube design

Feature No	**Normalized Coordinate**			**Parameter Coordinate**		
	x_1	x_2	x_3	$r_l = 1 + 19x_1$	$r_w = 0.1 + 0.9x_2$	$\phi = 90x_3$
BARLH1	0.46478	1	0.01969	9.830829	1	1.772114
BARLH2	0.993522	1	0.243345	19.87691	1	21.90108
BARLH3	0.056898	1	0.391855	2.081056	1	35.26698
BARLH4	0.594199	1	0.584805	12.28978	1	52.63244
BARLH5	0.305743	1	0.830053	6.809119	1	74.70479
BARLH6	0.720845	1	0.946429	14.69606	1	85.17859

Table 7.12 Test dataset for bar features constructed using Latin Hypercube design

Feature No	**Normalized Coordinate**			**Parameter Coordinate**		
	x_1	x_2	x_3	$r_l = 1 + 19x_1$	$r_w = 0.1 + 0.9x_2$	$\phi = 90x_3$
BRIDGELH1	0.993522	0.243345	1	19.87691	0.319011	90
BRIDGELH2	0.720845	0.946429	1	14.69606	0.951786	90
BRIDGELH3	0.594199	0.584805	1	12.28978	0.626324	90
BRIDGELH4	0.46478	0.01969	1	9.830829	0.117721	90
BRIDGELH5	0.305743	0.830053	1	6.809119	0.847048	90
BRIDGELH6	0.056898	0.391855	1	2.081056	0.45267	90

APPENDIX C: DETAILED RESULTS FOR THE VAT PHOTOPOLYMERIZATION EXPERIMENT

The results presented here are generated after removing the six outlier data points. The minimum feature size for individual oriented shapes is strongly influenced by a very small number of failed features (in the positive case) and passing features (for the negative case) caused by the stochasticity of the process but with minimal correlation with the feature scale. As a result, heuristic fits for individual feature types after four iterations are likely too low (because not enough data is collected to see the full variability of the process), while logistic fits may produce overly conservative design rules.

Following the same pattern as in Section 3.7, the results for bar features are presented first, followed by the 3D fit and separate bridge features. Note that the design rule functions constructed here use a different lower bounds function than that presented in Equation (3.4) which only utilizes the smallest collected data point instead of the mean of the smallest three.

A. Bar and Circular Hole Features for the Vat Photopolymerization Process Studied

The trends in the bar and circular hole data for the vat photopolymerization process selected are shown by visualizing the collected minimum feature size data in Figure 8.1. The estimated minimum feature size is significantly below the design rule set forth by i.materialze (1.0 mm) ("Design Guides: Gray Resin 3D Printing," n.d.), and no trend in the data supports the overhang angle constraint, despite its significant impact on the process at larger scales. Note that even the longest features $r_l = 20$ have a realized length of only 2-3 mm because $t_{min} < 0.2$. Positive features exhibit very large minimum diameters, and both datasets show a significant amount of noise.

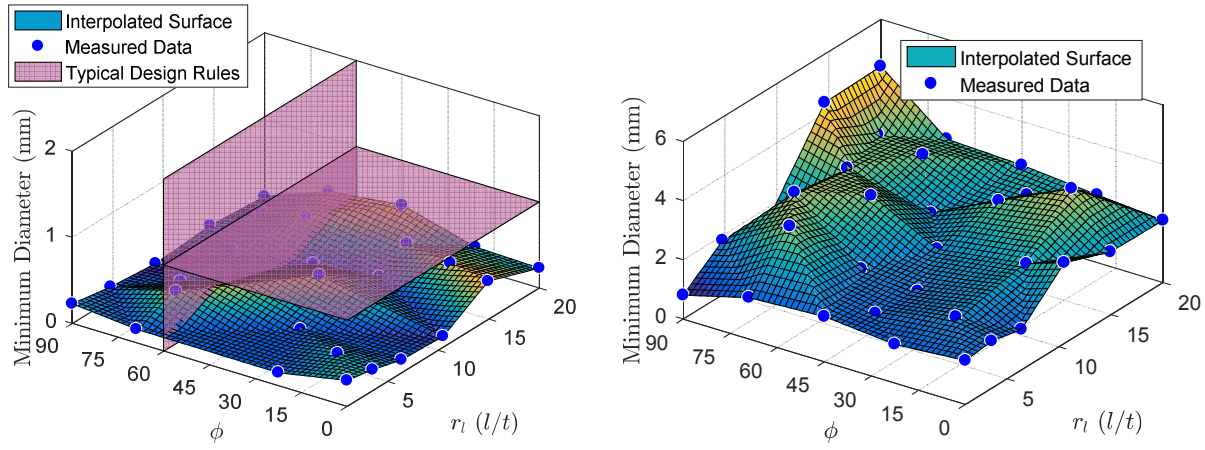

Figure 8.1. Positive and negative "bar" features. Positive features (a) include industry-specified design rules. Negative features shown in (b). Process: Form2 vat photopolymerization process

Figure 8.2 shows the same data with the sample points from NIST's test artifact (Moylan et al., 2014) overlaid on the $\phi = 0$ plane. The features on Moylan's test artifact for positive cylinders are of similar length scale to the geometry produced in the current study, so good agreement is seen. For negative features, the NIST test artifact's blind holes cause excessive buildup of resin which is difficult to remove, resulting in all holes failing to be produced.

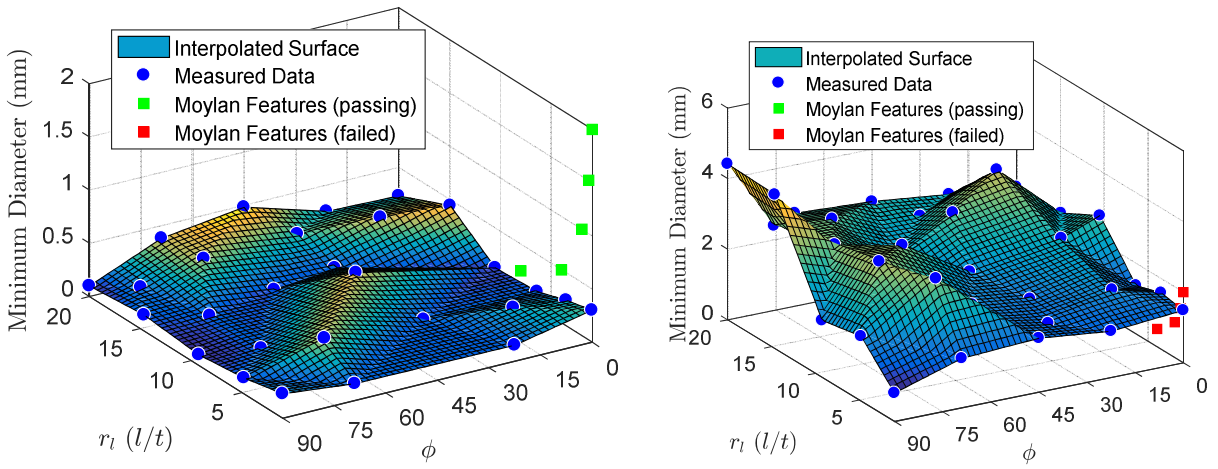

Figure 8.2. Positive and negative "bar" features along with the corresponding features from the NIST test artifact (Moylan et al., 2014), which all lay in the $\phi = 0$ plane. Positive features (a); negative features (b). Process: Form2 vat photopolymerization

As for the material extrusion case, a series of fitting functions is used to estimate a polynomial design rule for the data. Since no validation data in the bar feature space was

manufactured in the studied vat photopolymerization process, the error metric is defined against all of the relevant training data, regardless of experiment size, as shown in Figure 8.3. The high-frequency noise characteristics of the data cause even the 3rd order fit to provide negligible improvement in fit quality, and the order of the RMS error is roughly the order of the data. Three candidate fits (marked "Vis Points" in Figure 8.3) are visualized in Figure 8.4, with limited success.

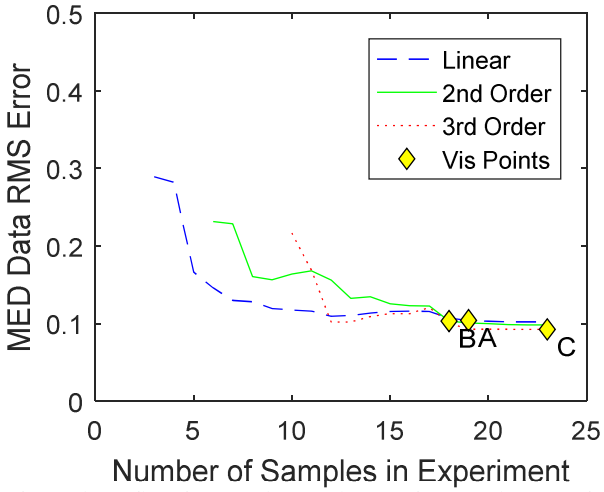

Figure 8.3. Design rule function fits for various sizes of experiment for positive bar features for the studied vat photopolymerization process. Errors are plotted with respect to the bar MED data.

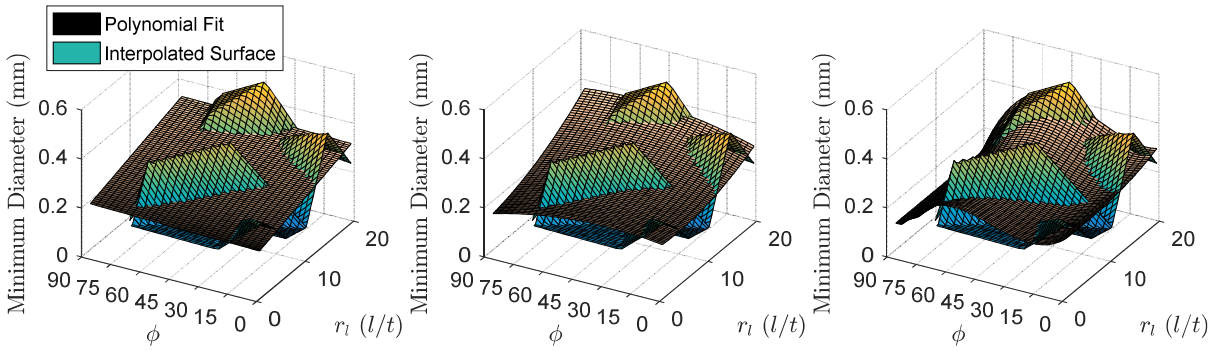

(A) Linear, 18 samples (B) Quadratic, 17 samples (C) Cubic, 21 samples

Figure 8.4. Design rule function fits at the points shown in the "Vis Points" A, B, and C in Figure 8.3.

B. 3D Design Rules for Features for the Vat Photopolymerization Process Studied

For the full 3D dataset, polynomial fit functions were used to define parametric design rules for various sizes of experiment. In Figure 8.5, the performance of these fit functions is evaluated against the test dataset, as well as against the full MED data. Note that for positive features, bridging features were again separated into a different study, presented in the next subsection. The trends for positive features over the whole domain are similar to those for bar features – noise and large errors are generally independent of the fit order, and show slow decline with increasing number of samples. For negative features, cubic fits do perform well above about 30 data points on both test and MED error metrics, with errors only about 35% of the mean value of the data.

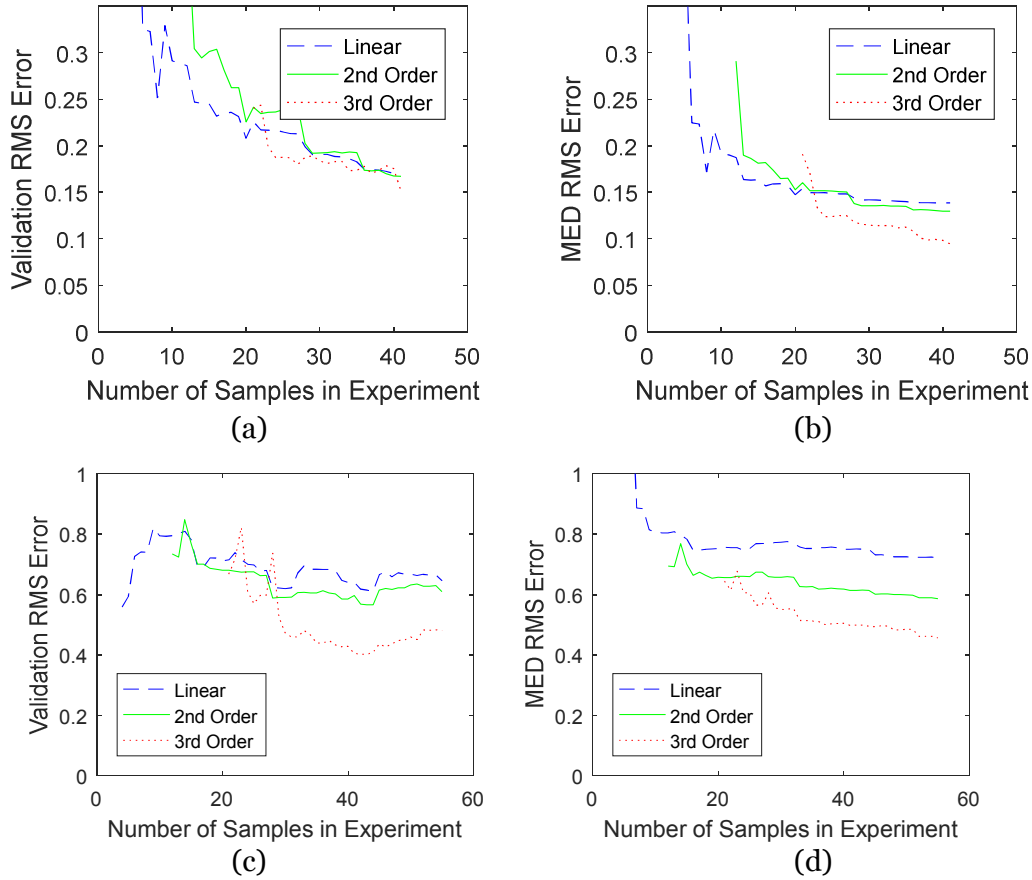

Figure 8.5. Design rule function fits for various sizes of experiment in the studied vat photopolymerization process. Top row: positive features. Bottom row: negative features (a), (c) show error against the test dataset, (b), (d) show error against the MED dataset.

C. Positive Bridging Features for the Vat Photopolymerization Process Studied

Even though it may not have any effect on the trends, because different supports cause different behavior, the bridging data for positive features in the studied vat photopolymerization process was again removed from the main MED dataset and treated separately. Figure 8.6 shows the fit performance for various degrees of polynomial, and Figure 8.7 presents two example fit surfaces. Although numerically the quality of the fit is fairly good (evaluated against the bridging MED data because no test data was available), the trends in the data do not seem well captured by the fitting functions in Figure 8.7.

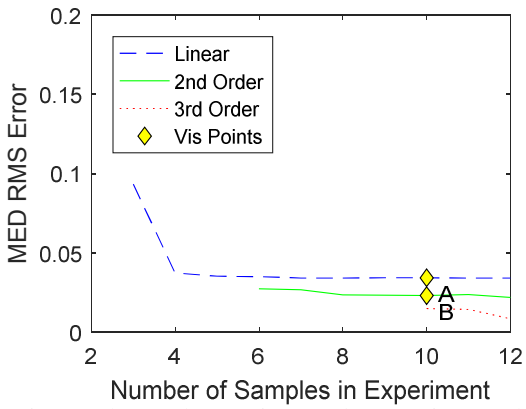

Figure 8.6. Design rule fits for various sizes of experiment for positive bridging features. Errors computed against the MED dataset for bridging features. Process: Form2 vat photopolymerization

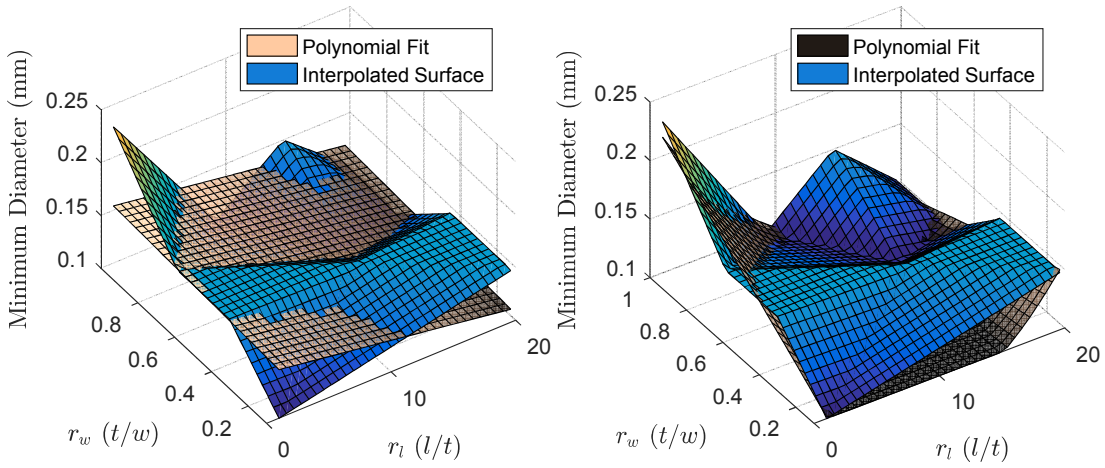

(A) Linear Fit, 8 samples (b) Quadratic fit, 8 samples

Figure 8.7. Two possible fits for the bridging dataset, highlighted in Figure 8.6 as “Vis Points”

APPENDIX D: DERIVATION OF THE SENSITIVITY IN SIMP

Most papers do not explain the origin of the negative sign in the last phrase of Equation (4.8a), reproduced below for reference:

$$\frac{\partial f}{\partial z_e} = \mathbf{u}_e^T \frac{\partial \mathbf{k}_e\left(\rho_e(\mathbf{z})\right)}{\partial z_e}\mathbf{u}_e = -p z_e^{p-1}(1 - E_{min})\mathbf{u}_e^T \mathbf{k}_0 \mathbf{u}_e \tag{4.8a}$$

Takalloozadeh and Yoon (2017) demonstrate the full derivation as follows. It is included here for reference. The derivatives of the compliance objective $f = \mathbf{U}^T\mathbf{K}\mathbf{U}$ and the FEA state equation $\mathbf{F} = \mathbf{K}\mathbf{U}$ are as follows

$$\frac{\partial f}{\partial x_e} = \frac{\partial}{\partial x_e}(\mathbf{U}^T\mathbf{K}\mathbf{U}) = \frac{\partial \mathbf{U}^T}{\partial x_e}\mathbf{K}\mathbf{U} + \mathbf{U}^T\frac{\partial \mathbf{K}}{\partial x_e}\mathbf{U} + \mathbf{U}^T\mathbf{K}\frac{\partial \mathbf{U}}{\partial x_e} \tag{9.22a}$$

$$\frac{\partial \mathbf{F}}{\partial x_e} = \frac{\partial \mathbf{K}}{\partial x_e}\mathbf{U} + \mathbf{K}\frac{\partial \mathbf{U}}{\partial x_e} \quad \Rightarrow \quad \frac{\partial \mathbf{U}}{\partial x_e} = \mathbf{K}^{-1}\frac{\partial \mathbf{F}}{\partial x_e} - \mathbf{K}^{-1}\frac{\partial \mathbf{K}}{\partial x_e}\mathbf{U} \tag{9.22b}$$

Substituting (9.22b) into (9.22a),

$$\begin{aligned}\frac{\partial f}{\partial x_e} &= \left(\mathbf{K}^{-1}\frac{\partial \mathbf{F}}{\partial x_e} - \mathbf{K}^{-1}\frac{\partial \mathbf{K}}{\partial x_e}\mathbf{U}\right)^T \mathbf{K}\mathbf{U} + \mathbf{U}^T\frac{\partial \mathbf{K}}{\partial x_e}\mathbf{U} + \mathbf{U}^T\mathbf{K}\left(\mathbf{K}^{-1}\frac{\partial \mathbf{F}}{\partial x_e} - \mathbf{K}^{-1}\frac{\partial \mathbf{K}}{\partial x_e}\mathbf{U}\right) \\ &= 2\mathbf{U}^T\frac{\partial \mathbf{F}}{\partial x_e} - \mathbf{U}^T\frac{\partial \mathbf{K}}{\partial x_e}\mathbf{U}\end{aligned} \tag{9.23}$$

Since the force does not vary with the design, $\frac{\partial \mathbf{F}}{\partial x_e} = 0$. Noting that $\frac{\partial \mathbf{K}}{\partial x_e}$ is nonzero only for element e, Equation (4.8a) is recovered.

APPENDIX E: MODIFICATIONS TO EXISTING CODES

The Method of Moving Asymptotes optimizer by Svanberg (1987) is used for the bcMMC approach, with the following modifications to mmasub.m, which adjust the move limits and stepping parameters to improve convergence.

```
epsimin = 10^(-10);
raa0 = 0.01;
move = 0.2;
albefa = 0.4;
asyinit = 0.1;
asyincr = 0.9;
asydecr = 0.7;
```

In addition, a modified version of top110.m, which is one of the sample codes provided by Andreassen (2011) and posted online at http://www.topopt.dtu.dk/?q=node/751

The top110 code was modified as follows. The load and support definitions (lines 19 and 21) are adjusted based on the conditions of each problem being solved. Finally, the `while` loop in line 58 is modified to run for a fixed number of iterations instead of stopping at a convergence criteria.

APPENDIX F: A DENSITY-BASED FEATURE-DRIVEN MANUFACTURING CONSTRAINT

A preliminary attempt at integrating an orientation-dependent minimum length scale into a density approach was created as part of the development of the MMC-based solution presented in Chapter 4, and a short description is included here for reference.

For this initial implementation, the constraint is created by manipulating the sensitivity filter already present in the SIMP code to avoid checker-boarding effects by imposing a static minimum feature size (Equation (4.9)). The radius of the sensitivity filter is normally set once and retained for the entire optimization process, but in this method an algorithm will change the radius dynamically for different regions of the parameter space depending on the nearest feature. This is admittedly unusual and may produce non-optimal results, because no gradient information is supplied for changes to the constraint, but it provides an easy initial implementation. For simplicity, the design domain is constrained to 2D, and feature diameter is taken to be only a function of orientation, though extension to dependence on other variables and to 3D are straightforward.

The filter radius to use at each point is determined based on its proximity to a detected feature. First, a 2D medial axis transform is used to extract a rough skeleton of the shape, then the skeleton is segmented to eliminate spurious “wing” segments. Each segment is approximated with a single linear segment, and the filter radius is defined based on its angle from the build direction (arbitrarily taken to be in the +y direction). The resulting filter radii are then projected back on the image using the Voronoi regions of the skeletal segments. Medial axis extraction from SIMP results has been used before to define optimization constraints, but in a simpler context (Zhang et al., 2014).

For example, consider the density field in Figure 11.1a. The threshold of the image is first computed, then the 2D discrete medial axis transform (implemented with Matlab function `bwmorph`) is taken, shown in Figure 11.1b.

The skeleton is then divided by finding branch points (again using Matlab's `bwmorph`). Branch points, where three branches of the skeleton come together, are cleared with a 3x3 "cross" stencil to separate the branches (see Figure 11.1c). This separates the skeletal branches so that a connected components routine (Matlab `bwconncomp`) can isolate each branch. The best-fit line for each branch is computed (Figure 11.1d). At this point, the angle and length of the best-fit line can be obtained and used to calculate the minimum size for this feature. This minimum size is then used to set the sensitivity filter radius everywhere in its Voronoi region in the density field (Figure 11.1e).

The above algorithm has been implemented as a modification of the well-known 99-line Topology Optimization Matlab Code (Sigmund, 2001b), with the feature radii updated every solution iteration. Although the 99-line code is somewhat outdated, it is easy to understand and provides a simple starting point. Newer codes avoid the grey transitions near the end of the members with more advanced filters, such as (Guest et al., 2004). My algorithm could be easily adapted to these newer filters.

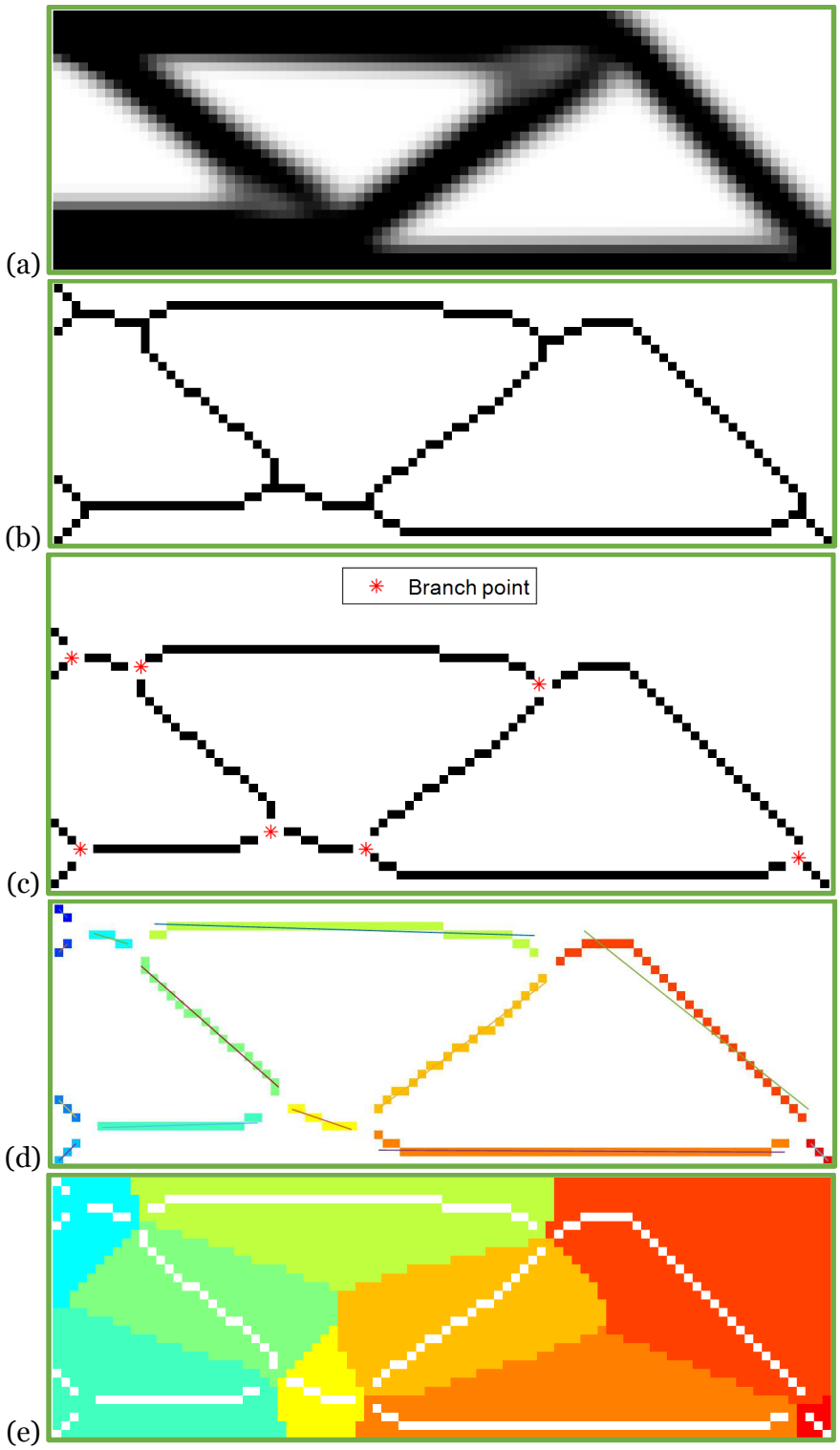

Figure 11.1. (a) An example density field (black = solid). (b) Skeleton. (c) Segmented skeleton with branch points. (D) Connected skeletal components with overlaid best-fit lines. (e) Voronoi regions for applying new filter radii across the domain based on skeleton segments

A. Preliminary Results

Despite not providing the optimizer with gradient information for the changing feature size, the approach presented above succeeds in producing solutions that satisfy the constraints and almost converge. The sensitivity of the medial axis transform to small boundary changes causes the optimizer to converge to a limit cycle near the optimum in some cases, where branches appear or shift slightly, producing a slight change in the density field, in turn causing the skeleton to change back to its previous state.

Consider the truss problem in Figure 11.2, top. The domain is six times longer than it is wide, with a unit load applied at the middle. Because the domain is symmetric, the problem can be simplified (Figure 11.2, middle). A reference solution from (Sigmund, 2001b) is shown in the bottom of Figure 11.2 for comparison with the current results.

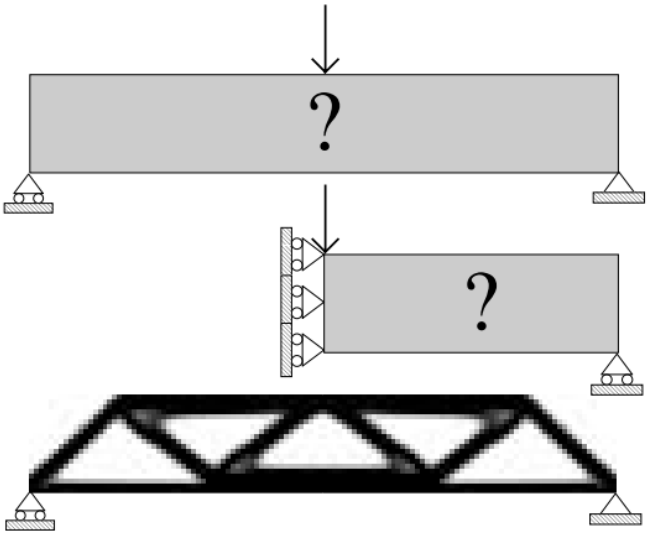

Figure 11.2. Top: Full Design domain. Middle: Symmetric equivalent domain. Bottom: Result from the 99-line code. Figure from (Sigmund, 2001b)

Figure 11.3 shows the results for three different feature size/feature angle relationships on a 60x20 grid with 30% volume fraction, and a mean filter size of 2.4. In (a), no relationship between feature angle and feature size is used, resulting in a solution which closely resembles the result from Sigmund (Sigmund used a volume fraction of 50%, however). In (b), diagonal

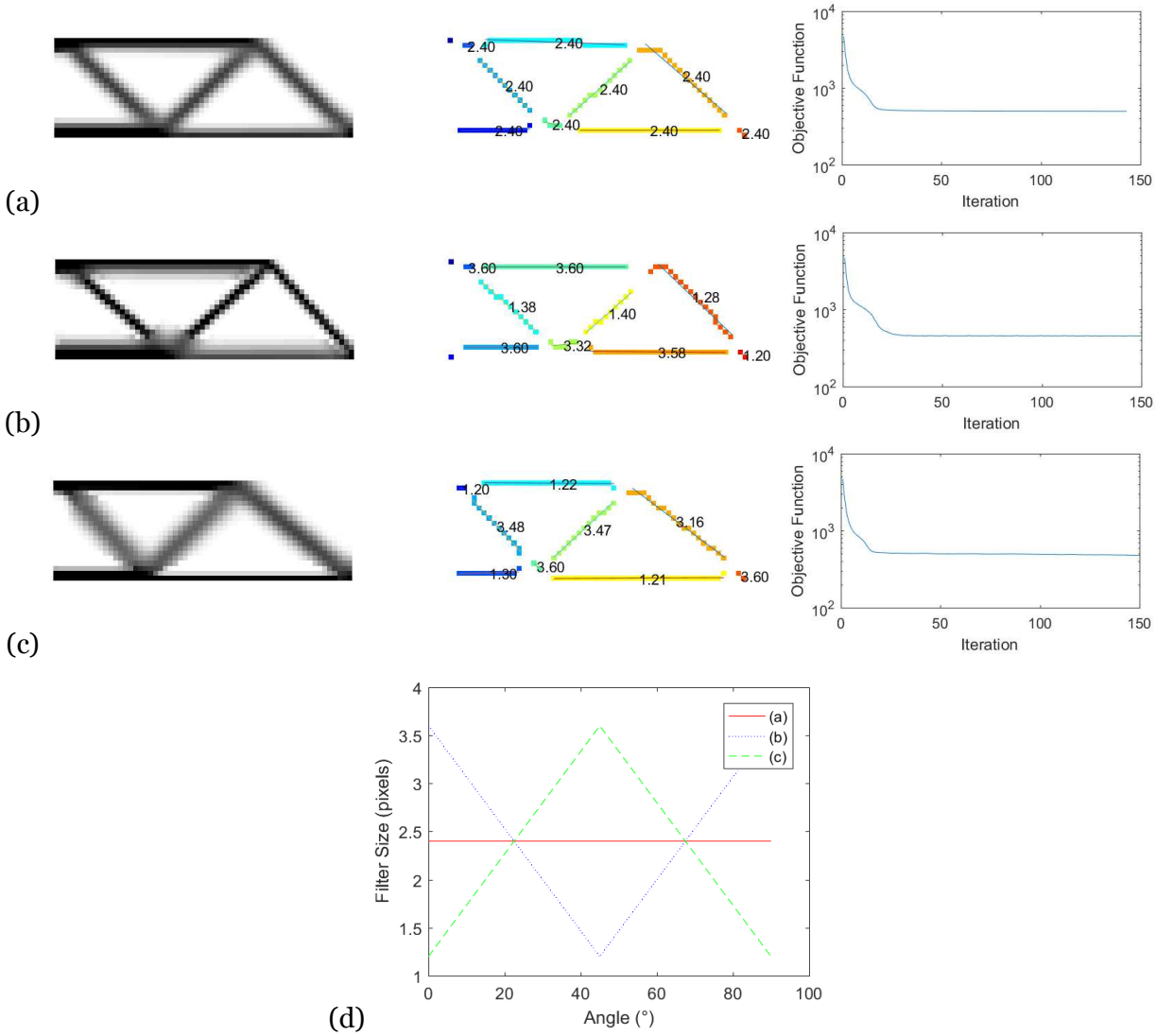

Figure 11.3 Results of feature-based algorithm for the (Sigmund, 2001b) test case, with angle-feature size relationships shown in (d). In each row, the density field is on the left, followed by the feature parameterization with overlaid feature sizes, with objective function convergence on the right.

elements are given much smaller feature sizes than horizontal elements, resulting in a truss with the same topology but significantly less material spent on the cross elements. Finally (c) reverses the relationship, penalizing diagonal features with a comparatively higher feature size. The resulting diagonal features are blurred because of the large radius filter applied, and the optimizer moves material away from the horizontal members (which can be small) and shortens the top segment of the span to allow for the high cost of the diagonals.

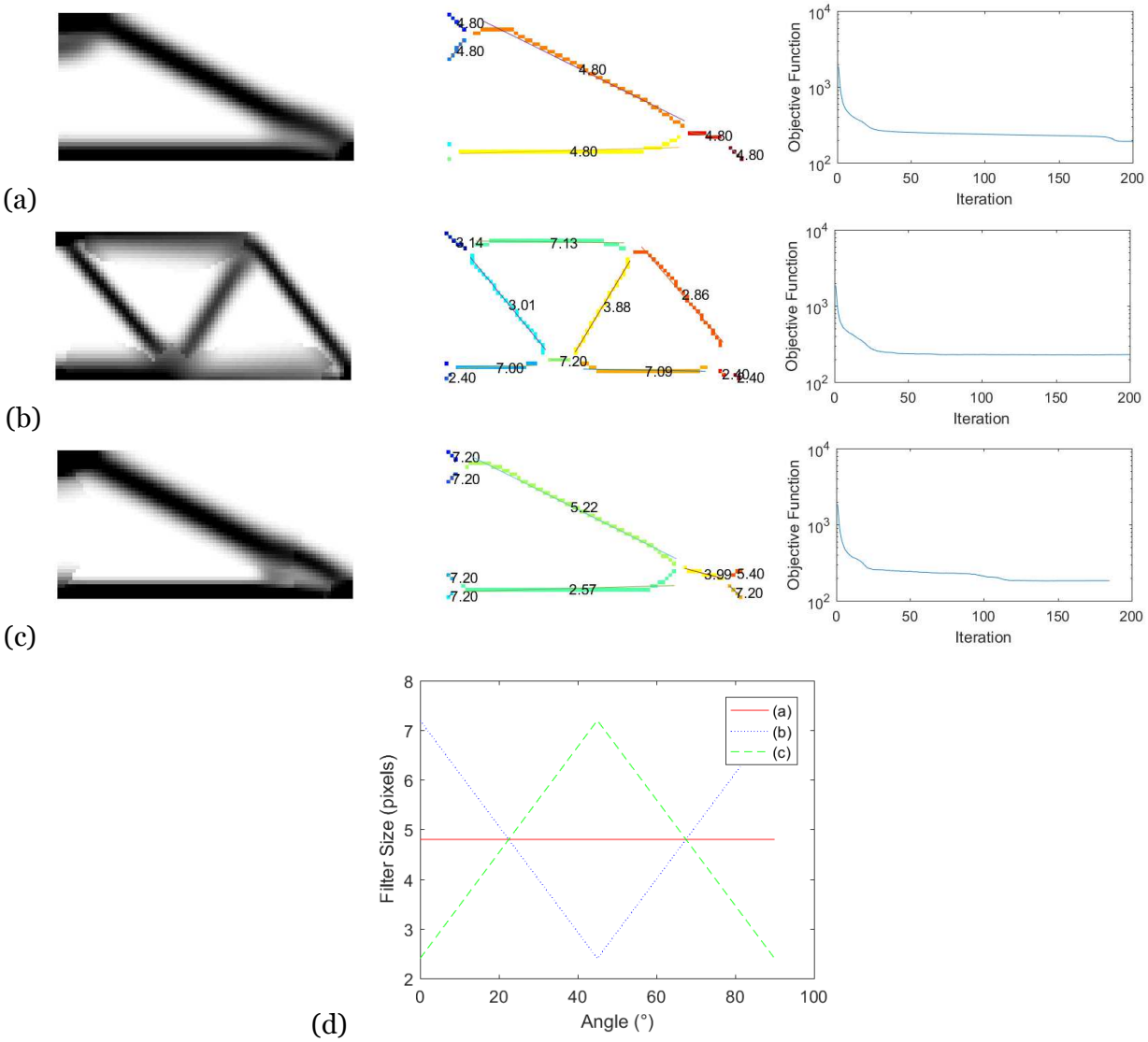

Figure 11.4. Results of feature-based algorithm for a different truss test case, with angle-feature size relationships shown in (d). In each row, the density field is on the left, followed by the feature parameterization with overlaid feature sizes, with objective function convergence on the right.

A different truss configuration is shown in Figure 11.4. This time, the 80x40 grid in the same load configuration as above is optimized with a 30% volume fraction and a mean filter size of 4.8. Again (a) reflects the uniformly-filtered SIMP approach. Note that bracing elements were present in the design until iteration 180 (resulting in the slight drop in the objective function). (b) and (c) show results for two different mappings between feature angle and feature size (shown in (d)). In (b), the relatively low cost of diagonal elements allows the development of a full truss, while in (c)

the high cost of diagonals results in a single element of higher angle. This result shows that the feature mapping can affect topology as well as the size of various members.

VITA

Benjamin M. Weiss is an Oregon native. He studied Mechanical Engineering at Oregon State University before entering graduate school at the University of Washington in 2012. Benjamin did his graduate work as a part of the Solheim Additive Manufacturing Lab, where he fixed printers, mentored undergraduates, wrote code, built circuits, did outreach to K-12 classrooms about 3D printing, and explored the possibilities of additive manufacturing.

The words of the wise are like goads, and like nails firmly fixed are the collected sayings; they are given by one Shepherd. My son, beware of anything beyond these. Of making many books there is no end, and much study is weariness of the flesh.
Ecclesiastes, 12:11-12, English Standard Version